

Washington University in St. Louis

Washington University Open Scholarship

All Theses and Dissertations (ETDs)

January 2010

Physics of ultrasonic wave propagation in bone and heart characterized using Bayesian parameter estimation

Christian Anderson

Washington University in St. Louis

Follow this and additional works at: <https://openscholarship.wustl.edu/etd>

Recommended Citation

Anderson, Christian, "Physics of ultrasonic wave propagation in bone and heart characterized using Bayesian parameter estimation" (2010). *All Theses and Dissertations (ETDs)*. 17.
<https://openscholarship.wustl.edu/etd/17>

This Dissertation is brought to you for free and open access by Washington University Open Scholarship. It has been accepted for inclusion in All Theses and Dissertations (ETDs) by an authorized administrator of Washington University Open Scholarship. For more information, please contact digital@wumail.wustl.edu.

WASHINGTON UNIVERSITY IN SAINT LOUIS

Department of Physics

Dissertation Examination Committee:

James G. Miller, Chair

Philip V. Bayly

G. Larry Bretthorst

Mark R. Conradi

Patrick C. Gibbons

Mark R. Holland

Martin H. Israel

PHYSICS OF ULTRASONIC WAVE PROPAGATION IN BONE AND
HEART CHARACTERIZED USING BAYESIAN PARAMETER
ESTIMATION

by

Christian Carl Anderson

A dissertation presented to the
Graduate School of Arts and Sciences
of Washington University in
partial fulfillment of the
requirements for the degree
of Doctor of Philosophy

August 2010

Saint Louis, Missouri

© copyright by

Christian Carl Anderson

2010

All rights reserved

Abstract

This Dissertation explores the physics underlying the propagation of ultrasonic waves in bone and in heart tissue through the use of Bayesian probability theory. Quantitative ultrasound is a noninvasive modality used for clinical detection, characterization, and evaluation of bone quality and cardiovascular disease. Approaches that extend the state of knowledge of the physics underpinning the interaction of ultrasound with inherently inhomogeneous and isotropic tissue have the potential to enhance its clinical utility.

Simulations of fast and slow compressional wave propagation in cancellous bone were carried out to demonstrate the plausibility of a proposed explanation for the widely reported anomalous negative dispersion in cancellous bone. The results showed that negative dispersion could arise from analysis that proceeded under the assumption that the data consist of only a single ultrasonic wave, when in fact two overlapping and interfering waves are present.

The confounding effect of overlapping fast and slow waves was addressed by applying Bayesian parameter estimation to simulated data, to experimental data acquired on bone-mimicking phantoms, and to data acquired *in vitro* on cancellous bone. The

Bayesian approach successfully estimated the properties of the individual fast and slow waves even when they strongly overlapped in the acquired data.

The Bayesian parameter estimation technique was further applied to an investigation of the anisotropy of ultrasonic properties in cancellous bone. The degree to which fast and slow waves overlap is partially determined by the angle of insonation of ultrasound relative to the predominant direction of trabecular orientation. In the past, studies of anisotropy have been limited by interference between fast and slow waves over a portion of the range of insonation angles. Bayesian analysis estimated attenuation, velocity, and amplitude parameters over the entire range of insonation angles, allowing a more complete characterization of anisotropy.

A novel piecewise linear model for the cyclic variation of ultrasonic backscatter from myocardium was proposed. Models of cyclic variation for 100 type 2 diabetes patients and 43 normal control subjects were constructed using Bayesian parameter estimation. Parameters determined from the model, specifically rise time and slew rate, were found to be more reliable in differentiating between subject groups than the previously employed magnitude parameter.

Acknowledgments

Most doctoral dissertations are the culmination of efforts by many more people than the author alone, and this one is no exception. During my graduate education, I was fortunate to meet many friends and colleagues who provided support and encouragement, only some of whom can possibly be named here. The research described in this Dissertation was performed primarily at the Laboratory for Ultrasonics in the Department of Physics at Washington University in St. Louis. My greatest debt of gratitude is to my advisor, James G. Miller, who along with Mark Holland oversaw my development not only as a scientist but as a writer, presenter, and communicator. I could not have asked for better mentorship.

I have tremendous appreciation for Larry Bretthorst, who provided expertise, advice, software, and computer time for me and others to learn and apply Bayesian probability theory. Karen Marutyan was also instrumental in this regard.

I am indebted to Keith Wear and his colleagues at the U.S. Food and Drug Administration, who offered considerable mentorship and support during my time spent there.

Several national and international collaborators contributed directly or indirectly

to this work, notably Keith Wear, Brent Hoffmeister, Pascal Laugier, Mami Matsukawa, and Michal Pakula. Within the Laboratory for Ultrasonics, I have enjoyed the companionship and advice of several current and former colleagues, including Kirk Wallace, Becky Trousil, Scott Handley, Steve Baldwin, Karen Marutyan, Min Yang, Adam Bauer, Allyson Gibson, Chris Lloyd, Joe Hoffman, Ben Johnson, and Amber Nelson.

I must express great thanks to my father, Michael Anderson, and to my late mother, Jan Anderson. It is difficult for me to imagine completing graduate studies without their example.

Finally, my most profound thanks to Allyson, my lab partner, fellow T.A., office-mate, accomplice, confidante, and lifelong companion. My wish is for the rest of our years together to be as happy as the ones we have experienced so far.

Contents

Abstract	iv
Acknowledgments	vi
List of Figures	xi
List of Tables	xvi
1 Introduction	1
1.1 Background and Motivation	1
1.2 Overview of the Dissertation	3
Bibliography	5
2 Clinical Applications of Ultrasonic Wave Propagation in Bone	7
2.1 Preface	7
2.2 Introduction	8
2.2.1 Bone anatomy and physiology	8
2.2.2 Osteoporosis	9
2.3 Quantitative ultrasound	12
2.4 Ultrasonic phase velocity in bone	17
2.4.1 Negative dispersion	18
2.4.2 Theoretical explanations for negative dispersion	20
2.4.3 Fast and slow compressional waves in bone	22
Bibliography	24
3 The Effect of Interfering Fast and Slow Waves on Dispersion in Cancellous Bone	30
3.1 Preface	30
3.2 Abstract	31
3.3 Introduction	32
3.4 Theory	36
3.4.1 Biot theory	38
3.4.2 Modified Biot-Attenborough model	41
3.4.3 Biot and Modified Biot-Attenborough model predictions	44
3.5 Simulated Wave Propagation in Bone	46

3.6	Results	50
3.7	Discussion	54
3.8	Conclusion	56
	Bibliography	58
4	Bayesian Probability Theory and Markov Chain Monte Carlo	61
4.1	Preface	61
4.2	Abstract	62
4.3	Bayesian probability theory	62
4.3.1	Historical perspective	62
4.3.2	Bayes' Theorem	64
4.4	Bayesian calculations	65
4.5	Markov chain Monte Carlo	69
4.5.1	Markov chains	70
4.5.2	The Metropolis-Hastings algorithm	71
4.5.3	Simulated annealing	74
4.5.4	Nested sampling	79
	Bibliography	84
5	Estimating Fast and Slow Wave Ultrasonic Properties in Bone Using Bayesian Probability Theory	86
5.1	Preface	86
5.2	Abstract	87
5.3	Introduction	87
5.4	Methods	90
5.4.1	Ultrasonic data acquisition	90
5.4.2	Model of ultrasonic wave propagation	93
5.4.3	Bayesian calculations	94
5.5	Results	97
5.5.1	Simulated data	97
5.5.2	Phantom data	101
5.5.3	Cancellous bone data	104
5.6	Discussion	107
5.7	Conclusion	112
	Bibliography	113
6	Anisotropy of Ultrasonic Properties in Cancellous Bone	118
6.1	Preface	118
6.2	Introduction	119
6.3	Methods	120
6.3.1	Data acquisition	120
6.3.2	Analysis	121
6.4	Results	121

6.5	Discussion	127
	Bibliography	131
7	Bayesian Analysis of Cyclic Variation of Myocardial Backscatter	132
7.1	Preface	132
7.2	Abstract	133
7.3	Introduction	134
7.4	Methods	135
	7.4.1 Subjects	135
	7.4.2 Laboratory tests	136
	7.4.3 Data acquisition	137
	7.4.4 Model of cyclic variation data	139
	7.4.5 Parameter estimation	140
	7.4.6 Data analysis	144
7.5	Results	146
7.6	Discussion	147
	Bibliography	152
8	Summary and Concluding Remarks	155

List of Figures

- 2.1 A sagittal cross section of an *ex vivo* human calcaneus (heel bone) specimen harvested from a cadaver donor. The bone marrow that normally fills the porous spaces within the cancellous bone has been removed. The complex trabecular structure of cancellous bone is surrounded by a thin layer of cortical bone and a residual amount of soft tissue. . . . 10
- 2.2 Diagnostic classification categories for bone quality based on bone mineral density (BMD) as defined by the World Health Organization. The normal distribution is an approximation of a histogram of bone mineral density for young white women; the abscissa indicates the number of standard deviations from the mean, or T-score. A BMD measurement between 1 and 2.5 standard deviations below the mean is defined as osteopenia (shaded gray region); a BMD lower than 2.5 standard deviations below the mean is defined as osteoporosis (shaded black region). 13
- 2.3 An image of the General Electric Achilles InsightTM device used for heel quantitative ultrasound. The subject's foot is placed in the device such that the heel is oriented between the two transducer housings, and ultrasonic signals are propagated through the calcaneus bone. Configuration settings and results of the test are displayed on the LCD screen. 16
- 2.4 Attenuation coefficient (Panel A) and phase velocity (Panel B) as for an excised human calcaneus specimen. Measurements were performed in the Laboratory for Ultrasonics. The attenuation coefficient is approximately linear with frequency. According to the Kramers-Kronig relations, the phase velocity should rise logarithmically with frequency (gray curve); however, the measured dispersion is negative (black circles). 21

- 3.1 Predictions of Biot theory (dashed lines) and Modified Biot-Attenborough model (solid lines) for fast and slow wave velocities at 500 kHz as functions of porosity. The top panel shows predictions at parallel insonification, and the bottom panel shows predictions at perpendicular insonification. The shaded regions indicate the approximate range of physiological porosities for bovine and human cancellous bone measured by other investigators. 45

-
- 3.2 The time-domain representation of the artificially generated reference pulse used as input to the simulations is displayed in the upper panel, and the power spectrum of the pulse is shown in the lower panel. . . . 47
- 3.3 Results of independent fast and slow wave propagation when the velocity of the fast wave is varied. The velocity of the fast wave increases from the left column to the right column. The top panels display the resultant mixed RF waveforms, and the center and bottom panels show the corresponding dispersion curves and attenuation coefficients obtained when the mixed waveform is analyzed as if it contained only one wave. When v_{fast} is only 50 m/s greater than v_{slow} (far left panels), the mixed waveform exhibits positive dispersion and a nearly linear attenuation coefficient. As v_{fast} becomes increasingly greater than v_{slow} (middle panels), the dispersion becomes negative. When v_{fast} is significantly larger than v_{slow} (far right panels), the dispersion curve and attenuation coefficient have complicated frequency-dependent behavior. 52
- 3.4 Results of independent fast and slow wave propagation when the relative contributions of the fast and slow wave are varied. The contribution of the fast wave increases from the left column to the right column. The top panels display the resultant mixed RF waveforms, and the center and bottom panels show the corresponding dispersion curves and attenuation coefficients obtained when the mixed waveform is analyzed as if it contained only one wave. The far left-hand panels display only slow wave propagation ($A_{fast} = 0, A_{slow} = 1$), resulting in a positive dispersion and a strictly linear attenuation coefficient. The far right-hand panels show only fast wave propagation ($A_{fast} = 1, A_{slow} = 0$), again corresponding to a positive dispersion and linear attenuation coefficient. The middle panels represent mixed waveforms (non-zero amplitudes for both fast and slow waves) that exhibit negative dispersions while maintaining an approximately linear attenuation coefficient. . . 53
- 4.1 Schematic of the beginning of a Markov chain trajectory in a hypothetical two-dimensional parameter space. The dashed lines represent probability contours, and the black dots are locations visited by the Markov chain. The neighborhood of the peak of the target probability density (center contours) will be more finely sampled than the outlying areas. 73
- 4.2 One-dimensional illustration of the effect of the annealing parameter β on a hypothetical target distribution of a parameter X . When $\beta = 0$, the target distribution is a smooth Gaussian prior. As β increases, the target distribution begins to resemble the multimodal posterior, and eventually becomes the posterior itself when $\beta = 1$. Allowing the Markov chains to converge to each intermediate distribution decreases the chance of one or more chains becoming stuck on a local maximum. 76

4.3	In this typical example from results of a simulation described in Chapter 5, 64 Markov chains each drew 64 samples from the joint posterior probability for a group of parameters Θ . The logarithm of the posterior probability for each of the 64 chains is plotted against the sample repeat number. The trajectories of the chains are well-mixed, suggesting an absence of evidence against convergence.	78
4.4	Schematic of nested sampling acting on a one-dimensional target distribution (black lines). The live samples are represented by gray circles. The likelihood constraint L^* defined by the lowest-probability sample (horizontal dashed line) moves upward at each iteration, compressing the subset of the parameter space where the samples are allowed to exist into the high-probability region.	82
5.1	Data acquisition arrangement for the Lexan phantom with a step discontinuity (top, Panel A) and the phantom made from bonded Lexan and Plexiglas (bottom, Panel B).	92
5.2	Input data to the Bayesian calculations (top panel, solid black circles) consisting of the sum of a simulated fast wave (middle panel, black squares) and slow wave (bottom panel, black circles). The output of the Bayesian calculations corresponding to each portion of the data is shown superimposed in a gray line. The signal-to-noise ratio in the input data is 50:1.	99
5.3	Marginal posterior probability density functions for the three sets of simulated data at varying signal-to-noise ratio (SNR) levels. All distributions integrate to 1. SNRs of 50:1, 100:1, and 250:1 are shown in circles, squares, and triangles, respectively. As the signal quality improves, the width of the distributions decreases, indicating increased confidence in the parameter value. However, the mean and peak parameter values do not change appreciably.	100
5.4	Data acquired at 5 MHz on a Lexan phantom with a step discontinuity (top panel, dark circles) with the model constructed from the parameters that maximized the joint posterior probability superimposed (top panel, gray line). The fast and slow waves that comprise the model are displayed in the bottom panel.	102
5.5	Conventional analysis of the data from a Lexan phantom with a step discontinuity yields significant artifacts in the attenuation coefficient and phase velocity near band center. In contrast, the curves for the fast and slow waves obtained using Bayesian probability theory are smoothly varying and consistent with a flat and parallel block of Lexan. 103	103

5.6	Data acquired at 500 kHz on a phantom constructed from bonded blocks of Lexan and Plexiglas (top panel, dark circles) with the model constructed from the parameters that maximized the joint posterior probability superimposed (top panel, gray line). The fast and slow waves that comprise the model are displayed in the bottom panel. . .	105
5.7	Data acquired at 500 kHz at one site on a human femur condyle specimen (top panel, dark circles) with the model constructed from the parameters that maximized the joint posterior probability superimposed (top panel, gray line). The fast and slow waves that comprise the model are displayed in the bottom panel.	108
5.8	The conventionally measured phase velocity for the data acquired on a human femur condyle (left panel, dark circles) exhibits an anomalous negative dispersion, in contrast with the dispersion predicted by the Kramers-Kronig relations (left panel, gray curve). The fast and slow wave dispersions obtained using Bayesian probability theory (right panel) do not exhibit anomalous behavior.	109
5.9	Values for nBUA and phase velocity at band center inferred by Bayesian probability theory for nine spatial locations within the same human femur condyle specimen. The phase velocities do not vary substantially over the nine sites, but there is considerable variation in nBUA. . . .	109
6.1	Acquired experimental data (black curves) and models constructed using Bayesian probability theory (gray curves) for a cancellous bone sample. The angles θ are insonation angles relative to the predominant trabecular alignment. As θ increases from parallel to perpendicular insonation, the fast and slow waves become more overlapped.	123
6.2	The most probable values for the parameters A_{fast} (top) and A_{slow} (bottom) as a function of insonation angle for a bovine cancellous bone specimen.	124
6.3	The most probable values for the parameters β_{fast} (top) and β_{slow} (bottom) as a function of insonation angle for a bovine cancellous bone specimen.	125
6.4	The signal loss at band center (1 MHz) as a function of insonation angle for a bovine cancellous bone specimen.	126
6.5	The most probable values for the parameters v_{fast} (top) and v_{slow} (bottom) at 1 MHz as a function of insonation angle for a bovine cancellous bone specimen.	128
6.6	The ratio of maximum fast wave amplitude to maximum slow wave amplitude as a function of insonation angle for a bovine cancellous bone specimen.	129

7.1	Regions of interest were placed within the posterior left ventricular wall on each image frame (shown in Panel A) and tracked throughout the heart cycle. The average level of backscatter was determined for each frame and averaged across five heart cycles to obtain an average cyclic variation waveform, such as the one depicted in Panel B.	138
7.2	Panel A (top): Schematic of a model cyclic variation waveform and the parameters used to characterize it. The high and low amplitude levels determine the magnitude, and the four transition time parameters (x_1, x_2, x_3, x_4) mark the locations where the line segments join. Given a set of values for these six parameters, the model waveform (shown in gray) can be constructed. Panel B (bottom): Illustration of the pulse parameters derived from a model cyclic variation waveform. The magnitude is the difference between the high and low levels, and the rise time is the time taken to go from 10% of the magnitude to 90% of the magnitude on the rising edge. The slew rate is the difference between the 90% level and the 10% level, divided by the rise time.	141
7.3	Representative results for models of acquired cyclic variation data. The data, consisting of backscatter averaged over five heart cycles, are shown in gray circles; the models are shown in solid black lines. The flexible nature of the model allows good representation of both narrow (Panel A) and wide (Panel B) waveform data.	148
7.4	Differences in the magnitude, rise time, and slew rate of the cyclic variation of backscatter from myocardium among the two subject groupings. Differences between normal control and type 2 diabetic subjects are shown in the left panels, and those between the highest and lowest quartiles of subjects grouped by glycated hemoglobin (HgA1c) are shown in the right panels. Data are presented as means \pm standard errors. Corresponding p -values determined by two-tailed t -tests are included in each panel.	149

List of Tables

3.1	Biot theory and modified Biot theory parameters used to compute the velocities used in the simulations of wave propagation. The calculated velocities are displayed as a function of porosity in Fig. 3.1.	37
5.1	Prior probabilities for each model parameter. The means and standard deviations define Gaussian probability density functions that are bounded by the low and high values.	96
5.2	The input values of the model parameters used to construct simulated data sets are compared to the output means and standard deviations of the Monte Carlo samples computed using Bayesian probability theory.	98
5.3	The expected values of the model parameters are taken from ultrasonic measurements performed on a flat and parallel block of Lexan. These expected values are compared to the means and standard deviations of the Monte Carlo samples computed using Bayesian probability theory for the data acquired on a block of Lexan with a step discontinuity. .	104
5.4	The expected values of the model velocity parameters are taken from separate ultrasonic measurements performed on flat and parallel blocks of Lexan and Plexiglas. These expected values are compared to the means and standard deviations of the Monte Carlo samples computed using Bayesian probability theory for the data acquired on a phantom constructed by bonding blocks of Lexan and Plexiglas.	106
5.5	Means and standard deviations of the Monte Carlo samples computed using Bayesian probability theory for the data acquired on a human cancellous bone specimen taken from a femur condyle.	107
7.1	Summary of prior probability density functions used for each parameter in the Bayesian calculations. The means and standard deviations define Gaussian probability densities bounded by the low and the high values.	143
7.2	Study group characteristics for the control and diabetic populations. .	145
7.3	Study group characteristics for the glycated hemoglobin (HbA1c) highest and lowest quartiles.	146

CHAPTER 1

INTRODUCTION

1.1 Background and Motivation

The broad theme of this Dissertation is the application of Bayesian probability theory to the physics underlying ultrasonic wave propagation in bone and heart tissue. Ultrasound is a modality that is well-suited for characterizing tissue because of its sensitivity to the mechanical properties of the medium in which it propagates. Consequently, analyses of ultrasonic data acquired on tissue may provide a non-invasive way to highlight subtle abnormalities before they are manifested symptomatically. An improved understanding of the physics underlying the propagation of ultrasonic waves in biological tissues can therefore lead to an improved ability detect, characterize, and diagnose pathologies. Specific pathologies pertinent to this Dissertation are osteoporosis and type 2 diabetes.

Osteoporosis is a disease characterized by a decrease in bone mass and an overall deterioration of bone structure, leading to increased fracture risk. Quantitative ultrasound is a tool for identifying the changes in bone quality that appear as the disease progresses (Njeh *et al.*, 1999; Hans *et al.*, 1999; Hans and Krieg, 2008; Bonnick, 2004). However, despite its potential advantages over X-ray based methods (described in Chapter 2), ultrasound has not proven to be superior to X-ray-based measurements of bone density. An incomplete understanding of the physics of ultrasonic wave propagation in bone may be a partial explanation for this failure of bone sonometry to live up to its clinical potential. In particular, an apparent conflict exists between measured phase velocities in cancellous bone and the dispersion predicted by the Kramers-Kronig relations (Waters and Hoffmeister, 2005; Wear, 2007). A portion of this Dissertation is dedicated to a proposed explanation for this phenomenon, and applying Bayesian methods to ultrasonic data acquired on bone to overcome the consequences of the apparent contradiction.

Type 2 diabetes is a risk factor for cardiovascular disease, including diabetic cardiomyopathy (Fang *et al.*, 2004; Hamby *et al.*, 1974; Kannel *et al.*, 1974; Rijzewijk *et al.*, 2008; Witteles and Fowler, 2008). Previous studies have indicated that parameters derived from analysis of the cyclic variation of backscatter from myocardium over the heart cycle could be early indicators of diabetic cardiomyopathy (Gibson *et al.*, 2009; Pérez *et al.*, 1992; Wagner *et al.*, 1995). A goal of this Dissertation is to extend such analyses by invoking a novel method for modeling cyclic variation of backscatter so that parameters potentially more sensitive to diastolic dysfunction can

be examined. Bayesian probability theory is used to estimate the model parameters.

1.2 Overview of the Dissertation

The first portion of this Dissertation is focussed on ultrasonic wave propagation in cancellous bone, especially the relationships between dispersion and the frequency dependence of the attenuation coefficient. Chapter 2 provides a more extensive background on osteoporosis and bone ultrasonography, as well as an overview of studies of negative dispersion and multiple-mode wave propagation in cancellous bone.

The discussion of dispersion in bone is continued in Chapter 3, where simulated wave propagation is used to show that the negative dispersion observed in bone by many investigators can arise when data composed of multiple interfering compressional wave modes is analyzed as if only one wave is present.

Chapter 4 is a summary of Bayesian probability theory and the Markov chain Monte Carlo methods used in later chapters. The calculations used for Bayesian parameter estimation are presented, along with explanations of simulated annealing and nested sampling algorithms.

In Chapter 5, Bayesian probability theory is applied to simulated data, to data acquired on bone-mimicking phantoms, and to data acquired on excised cancellous bone specimens. Parameters that characterize frequency-independent signal loss, attenuation coefficient, and speed of sound for interfering fast and slow waves present in the data are estimated. Results suggest that data analyzed in this manner might

aid in eliminating artifacts in conventionally obtained phase velocity measurements.

A further application and extension of the methods used in Chapter 5 is presented in Chapter 6. The anisotropic structure of cancellous bone results in ultrasonic properties that also exhibit anisotropy. However, measurements exhibiting this anisotropy often cannot be carried out because of significant overlap between fast and slow waves. Bayesian analysis is applied to such data in an effort to fully characterize the anisotropy of several ultrasonic parameters in bovine femur.

Chapter 7 presents an application of Bayesian parameter estimation to a novel model of cyclic variation of myocardial backscatter in type 2 diabetes patients. Parameters derived from the model appear to provide improved approaches for identifying hearts at potentially greater risk.

Chapter 8 contains a summary and concluding remarks.

Bibliography

- Bonnick, S. L. (2004). *Bone Densitometry in Clinical Practice* (Humana Press).
- Fang, Z. Y., Prins, J. B., and Marwick, T. H. (2004). “Diabetic cardiomyopathy: evidence, mechanisms, and therapeutic implications”, *Endocr Rev* **25**, 543–67.
- Gibson, A. A., Schaffer, J. E., Peterson, L. R., Bilhorn, K. R., Robert, K. M., Haider, T. A., Farmer, M. S., Holland, M. R., and Miller, J. G. (2009). “Quantitative analysis of the magnitude and time delay of cyclic variation of myocardial backscatter from asymptomatic type 2 diabetes mellitus subjects”, *Ultrasound Med Biol* **35**, 1458–1467.
- Hamby, R. I., Zoneraich, S., and Sherman, L. (1974). “Diabetic cardiomyopathy”, *JAMA* **229**, 1749–54.
- Hans, D. and Krieg, M. (2008). “The clinical use of quantitative ultrasound (QUS) in the detection and management of osteoporosis”, *IEEE Trans Ultrason Ferroelectr Freq Control* **55**, 1529 – 1538.
- Hans, D., Wu, C., Njeh, C. F., Zhao, S., Augat, P., Newitt, D., Link, T., Lu, Y., Majumdar, S., and Genant, H. K. (1999). “Ultrasound velocity of trabecular cubes reflects mainly bone density and elasticity”, *Calcif Tissue Int* **64**, 18–23.
- Kannel, W. B., Hjortland, M., and Castelli, W. P. (1974). “Role of diabetes in congestive heart failure: the framingham study”, *Am J Cardiol* **34**, 29–34.
- Njeh, C. F., Hans, D., Fuerst, T., Glüer, C.-C., and Genant, H. K. (1999). *Quantitative Ultrasound: Assessment of Osteoporosis and Bone Status* (Martin Dunitz Ltd).
- Pérez, J. E., McGill, J. B., Santiago, J. V., Schechtman, K. B., Waggoner, A. D., Miller, J. G., and Sobel, B. E. (1992). “Abnormal myocardial acoustic properties in diabetic patients and their correlation with the severity of disease”, *J Am Coll Cardiol* **19**, 1154–62.
- Rijzewijk, L. J., van der Meer, R. W., Smit, J. W., Diamant, M., Bax, J. J., Hammer, S., Romijn, J. A., de Roos, A., and Lamb, H. J. (2008). “Myocardial steatosis is an independent predictor of diastolic dysfunction in type 2 diabetes mellitus”, *J Am Coll Cardiol* **52**, 1793–9.
- Wagner, R. F., Wear, K. A., Perez, J. E., McGill, J. B., Schechtman, K. B., and Miller, J. G. (1995). “Quantitative assessment of myocardial ultrasound tissue characterization through receiver operating characteristic analysis of Bayesian classifiers”, *J Am Coll Cardiol* **25**, 1706–11.

- Waters, K. R. and Hoffmeister, B. K. (2005). “Kramers-Kronig analysis of attenuation and dispersion in trabecular bone”, *J Acoust Soc Am* **118**, 3912–20.
- Wear, K. A. (2007). “Group velocity, phase velocity, and dispersion in human calcaneus in vivo”, *J Acoust Soc Am* **121**, 2431–7.
- Witteles, R. M. and Fowler, M. B. (2008). “Insulin-resistant cardiomyopathy clinical evidence, mechanisms, and treatment options”, *J Am Coll Cardiol* **51**, 93–102.

CHAPTER 2

CLINICAL APPLICATIONS OF ULTRASONIC WAVE PROPAGATION IN BONE

2.1 Preface

This Chapter contains an overview of bone anatomy and bone physiology, and osteoporosis. The relevance of quantitative ultrasound to the diagnosis and monitoring of osteoporosis, as well as improvements that may be achieved through a greater understanding of ultrasonic wave propagation in bone, are also discussed.

2.2 Introduction

2.2.1 Bone anatomy and physiology

Bone is living tissue that provides bodily structure and support. There are two bone tissue types that are primarily important to clinical ultrasound applications. The first is cortical bone, also known as compact bone, a relatively solid material that comprises the exterior shell of bones. The second is cancellous or trabecular bone, a highly porous material found primarily in bone interiors, especially in the spine, hip, heel, wrist, and at the the ends of long bones. These two tissue types have remarkably different architectures and mechanical properties. Cortical bone has an intricate microstructure of tiny canals and tunnels through which the circulatory and lymphatic system distribute nutrients, but the porosity is generally low enough, about 4-10 percent (Laval-Jeantet *et al.*, 1983), that cortical bone can be assumed to be a homogeneous and isotropic solid for typical clinical ultrasound frequencies (~ 200 - 1000 kHz). In contrast, cancellous bone is a complex lattice-like structure composed of hard rod-shaped and plate-shaped elements (trabeculae) interspersed with soft bone marrow. The porosity of human cancellous bone ranges from 60 percent to above 95 percent (Hodgkinson *et al.*, 1996; Wear, 2005; Lee *et al.*, 2003; Hosokawa and Otani, 1998). Typical trabeculae can range from approximately 50-170 μm in thickness and are spaced 700-2000 μm apart (Thomsen *et al.*, 2002; Ulrich *et al.*, 1999). An example of cancellous bone is shown in the sagittal cross section of an excised human calcaneus (heel bone) specimen displayed in Fig. 2.1. The bone

marrow has been removed, exposing the trabecular network (cancellous bone) that dominates the interior. A thin outer boundary of cortical bone and overlying soft tissue are also visible.

Bone structure is continuously influenced by remodeling, a process in which old cancellous bone is discarded and replaced (Njeh *et al.*, 1999; Manolagas and Jilka, 1995; Parfitt, 1994). Remodeling is a complex process regulated by several hormones and growth factors (Manolagas and Jilka, 1995; Canalis *et al.*, 1988). Briefly, the remodeling process occurs as specialized cells known as osteoclasts resorb the bone matrix at discrete micro-damaged sites. The cavity left by resorption is then filled with replacement osteoid (collagen and other proteins) by other cells called osteoblasts, eventually leading to full remineralization. In healthy bone, a dynamic balance is maintained between osteoclast and osteoblast activity such that the volume fraction of bone is approximately constant on a global scale. Although the remodeling process is fundamentally the same in both cancellous and cortical bone, cancellous bone has a higher rate of turnover; approximately 25 percent of cancellous bone is resorbed and replaced annually in healthy adults, compared to approximately 3 percent of cortical bone (Manolagas and Jilka, 1995).

2.2.2 Osteoporosis

A negative imbalance in remodeling (more resorption than formation) results in a net bone loss. The bone loss results in thinner trabeculae and fewer trabecular connections in cancellous bone, and thinner and more porous cortical bone. Over

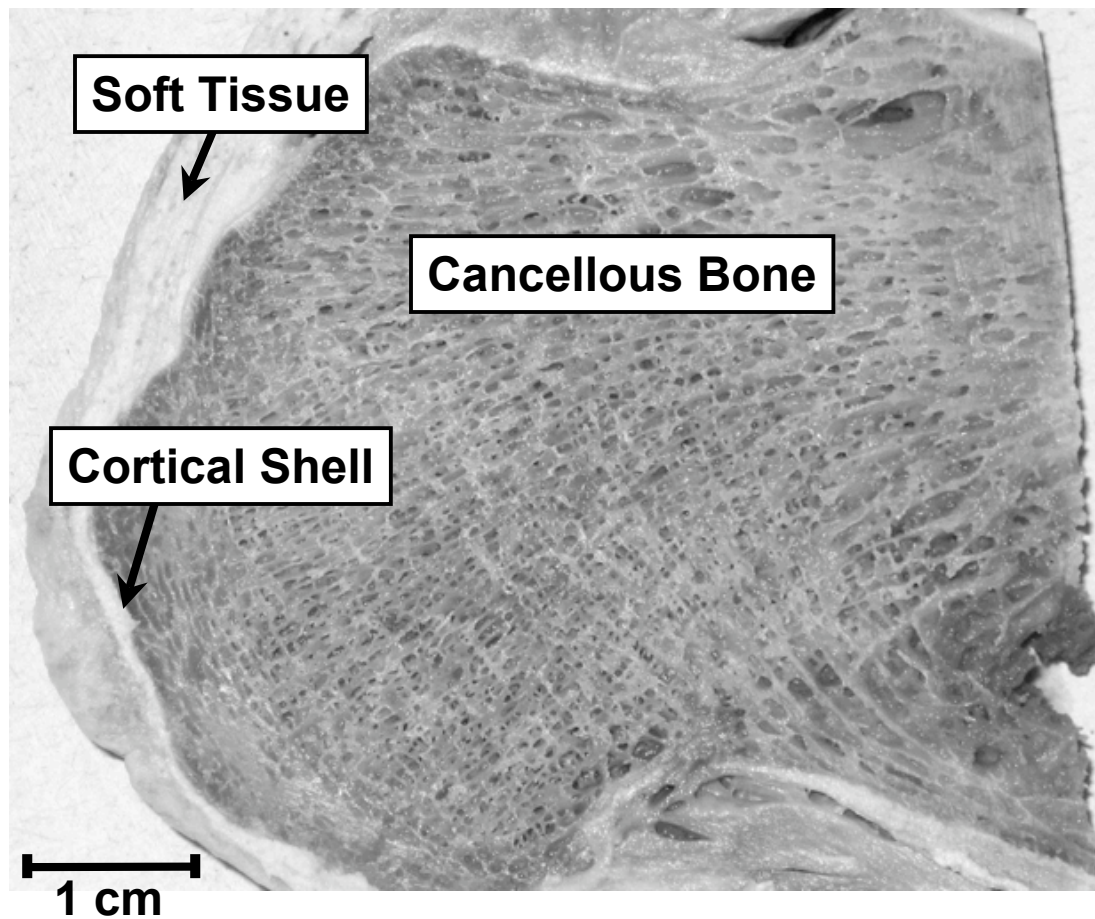


FIGURE 2.1: A sagittal cross section of an *ex vivo* human calcaneus (heel bone) specimen harvested from a cadaver donor. The bone marrow that normally fills the porous spaces within the cancellous bone has been removed. The complex trabecular structure of cancellous bone is surrounded by a thin layer of cortical bone and a residual amount of soft tissue. (Photo by Christian C. Anderson)

time, the degradation of bone quality leads to compromised skeletal strength and an increased risk of fragility-related fracture, especially at sites dominated by cancellous bone, such as the spine, hip, and wrist. This condition is a disease known as osteoporosis (WHO, 2004; NIH, 2001). Osteoporosis is a serious condition that currently affects over 10 million Americans, and the number of people at risk continues to rise as the population ages. Osteoporotic fractures are associated with high degrees of morbidity and mortality. Approximately one-fourth of subjects that suffer a hip fracture die within a year of the event due to resulting complications, and about one-half of those that remain are unable to live independently (Hans and Krieg, 2008; Langton and Njeh, 2008).

There are no current accurate explicit measures of *in vivo* bone strength. The current clinical gold standard for assessment of bone quality is bone mineral density (BMD), an X-ray based metric that provides a measure of the amount of bone present within a projected area, and hence acts as a proxy measure of bone strength (Cummings and Black, 1995; Johnell *et al.*, 2005; Kanis, 2002; Kanis *et al.*, 2007). BMD is measured by Dual Energy X-ray Absorptiometry (DEXA), a technique in which X-rays with two distinct energy peaks are used to distinguish calcified bone tissue from soft tissue in an areal projection (Bonnick, 2004). DEXA measurements are typically made at the hip and spine using large devices. These machine generally consist of a table for the subject to lie on combined with a scanning arm and some apparatus for X-ray generation, detection, and analysis.

The World Health Organization (WHO) has defined categories for bone quality

based on BMD relative to a reference population of young, healthy, white women (WHO, 1994; Kanis, 1994, 2002). The WHO committee responsible for these classifications did not have enough data to designate appropriate definitions for men and other ethnic groups. Osteopenia is defined as a BMD one standard deviation below the mean of the reference population, and osteoporosis is defined as a BMD more than 2.5 standard deviations below the mean. Severe or established osteoporosis is defined as osteoporosis in conjunction with a fragility fracture. Thus, by definition, approximately 15% of young white women have osteopenia, and approximately 0.6% have osteoporosis. Conventionally, the number of standard deviations below the mean of the reference population is reported as a T-score; thus, a T-score between -1 and -2.5 is classified as osteopenic, and a T-score less than or equal to -2.5 is osteoporotic (NIH, 2001; Kanis, 2002). An approximate histogram of bone mineral density for young white women (i.e., the reference population) is shown in Fig. 2.2. The osteopenic range of BMD is shaded gray, and the osteoporotic range is shaded black.

2.3 Quantitative ultrasound

An alternative modality for evaluating bone quality is quantitative ultrasound, often abbreviated QUS (Njeh *et al.*, 1999; Hans and Krieg, 2008; Hans *et al.*, 1996; Bonnicks, 2004; Garnero *et al.*, 1998). This method typically involves the transmission of ultrasonic waves along a surface of cortical bone, or through cancellous bone

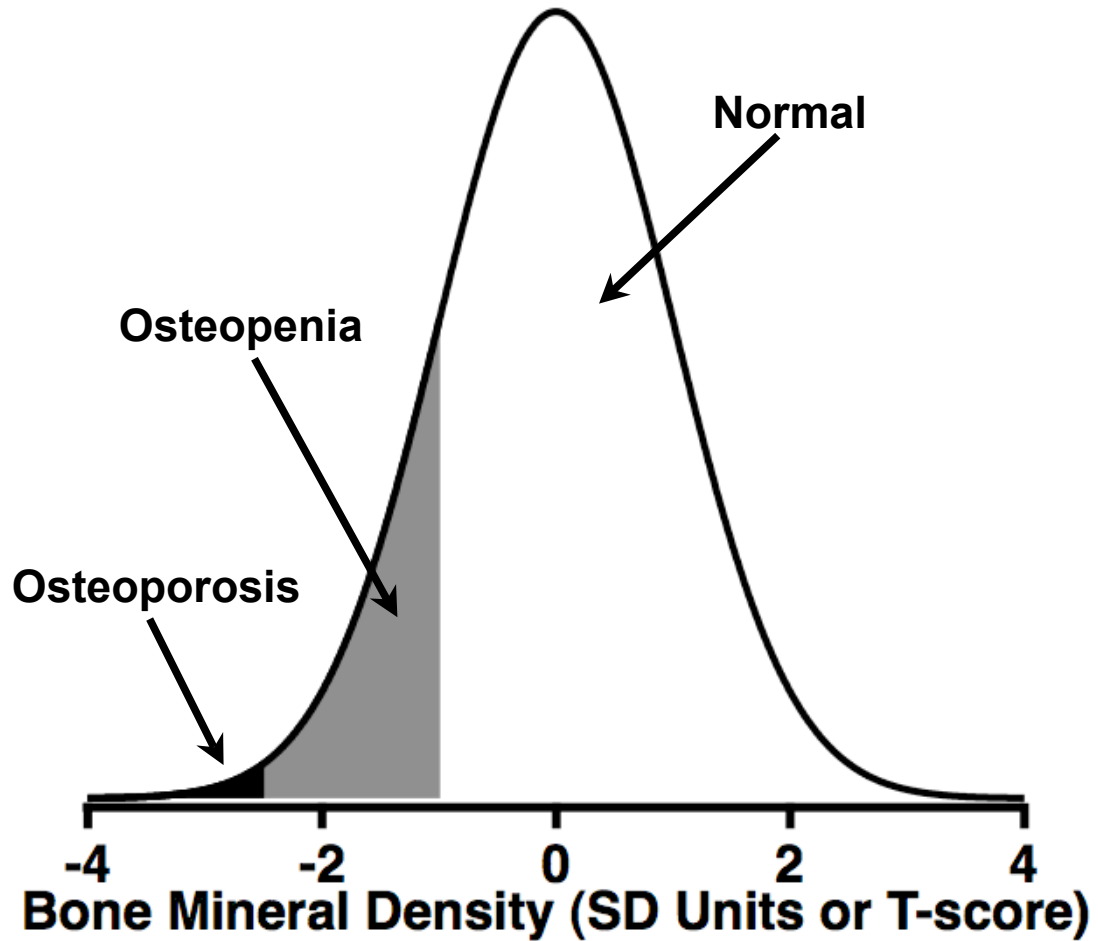


FIGURE 2.2: Diagnostic classification categories for bone quality based on bone mineral density (BMD) as defined by the World Health Organization. The normal distribution is an approximation of a histogram of bone mineral density for young white women; the abscissa indicates the number of standard deviations from the mean, or T-score. A BMD measurement between 1 and 2.5 standard deviations below the mean is defined as osteopenia (shaded gray region); a BMD lower than 2.5 standard deviations below the mean is defined as osteoporosis (shaded black region).

located at a peripheral skeletal site, such as the calcaneus (heel) bone. The primary wave phenomena of interest are signal velocity and attenuation. Ultrasound velocity is usually calculated using time-of-flight measurements through a sample of known or assumed thickness, and is reported in the research literature and by clinical devices as speed of sound (SOS) (Barkmann *et al.*, 2008; Goossens *et al.*, 2008; *et al.*, 2005; Strelitzki *et al.*, 1997; Wear, 2007a). Attenuation is usually expressed as the slope of a linear fit to the frequency-dependent signal loss, a parameter known as “Broadband Ultrasound Attenuation” (BUA) (Langton *et al.*, 1984; Langton and Njeh, 2008; Langton and Hodgskinson, 1997; Petley *et al.*, 1995; Strelitzki *et al.*, 1999; Wear, 2008). Occasionally, BUA is normalized by the bone thickness, in which case the parameter reported is “normalized Broadband Ultrasonic Attenuation” (nBUA). Clinical bone sonometry devices often combine velocity and BUA measurements into a single index of bone quality, but these indices vary across manufacturers (Bonnick, 2004). Bone sonometers enjoy some advantages over DEXA devices due to their high portability, relatively low cost, and zero risk of exposure to ionizing radiation. However, quantitative ultrasound suffers from an inability to directly measure sites of particular importance to osteoporotic fracture risk, the spine and hip. The locations of these bones make non-invasive transmission measurements difficult due to the large amounts of nearby overlying soft tissue, and their irregular surfaces generate complications involving scattering and refraction. Transmission bone sonometry therefore is typically performed at peripheral sites, especially the heel bone, under the assumption that osteoporosis is a systemic disease and should present at peripheral sites as well as

at the hip and spine. Devices designed for heel ultrasonography consist of a housing for the subject's foot and heel to rest, with a transmitting transducer and a receiving transducer on either side of the heel. A typical image of such a device, the General Electric (GE) Achilles InsightTM (General Electric Medical Systems, Waukesha, WI, USA) is shown in Fig. 2.3. In the Achilles InsightTM, the receiver is a two-dimensional array of transducer elements. A broadband signal is propagated through the heel, and velocity and BUA measurements are made by comparing the acquired signal to a stored reference waveform via time-of-flight measurement and a log spectral subtraction algorithm, respectively. The velocity and BUA results are combined into a proprietary index of bone quality and displayed to the user. Overall, the body of evidence from studies indicates that heel quantitative ultrasound is approximately as reliable as DEXA for predicting hip and spine fracture (Hans and Krieg, 2008).

Ultrasound modalities should, in theory, provide more information about bone quality than DEXA due to its greater sensitivity to physical properties. DEXA measures areal bone content, but does not provide direct measurements of resistance to fracture (e.g., elasticity). In contrast, the velocity of an acoustic wave has a physical relationship to both density and elasticity of the medium in which it propagates, namely

$$v = \sqrt{\frac{E}{\rho}}, \quad (2.1)$$

where v is velocity, E is elastic modulus, and ρ is mass density. Despite this theoretical advantage, quantitative ultrasound has not yet reached its full clinical potential. The ability of ultrasound to predict fractures approaches or equals the that of DEXA

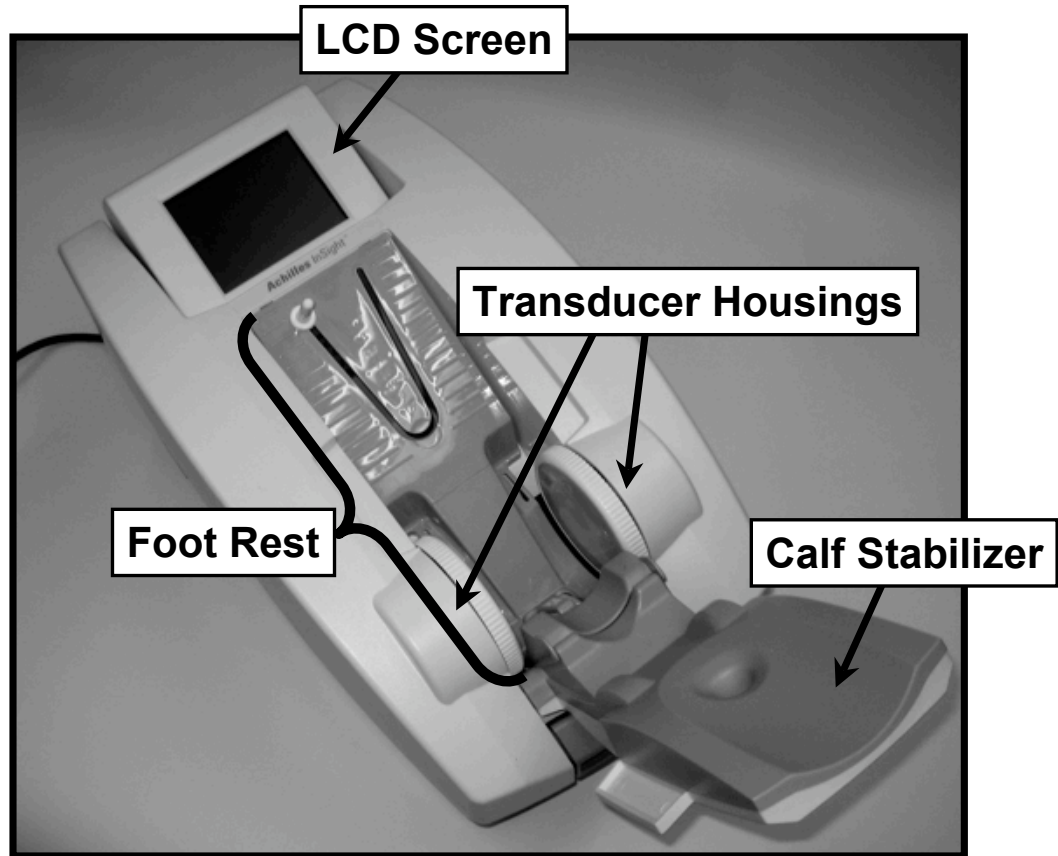


FIGURE 2.3: An image of the General Electric Achilles Insight™ device used for heel quantitative ultrasound. The subject's foot is placed in the device such that the heel is oriented between the two transducer housings, and ultrasonic signals are propagated through the calcaneus bone. Configuration settings and results of the test are displayed on the LCD screen. (Photo by Christian C. Anderson)

instead of surpassing it, and DEXA remains the clinical gold standard. Moreover, although studies of ultrasonic wave propagation in bone date to at least the 1970s, the phenomenon remains incompletely understood, and an improved understanding of the physics involved may lead to better clinical diagnostic performance. For this reason, ultrasonic wave propagation in bone is an active research area.

2.4 Ultrasonic phase velocity in bone

In the context of ultrasonic wave propagation in bone, phase velocity and dispersion are particular areas of interest. Along with other frequency-dependent effects, such as attenuation and phase cancellation at the face of a phase sensitive piezoelectric receiver, dispersion is known to influence measurements of group velocity such as those made by clinical ultrasound devices (Wear, 2009b, 2007a; Haiat *et al.*, 2006). Such effects cause the received signal to be markedly different from the transmitted signal, complicating time-of-flight measurements used in group velocity calculation. In addition, reporting only the group velocity excludes any information about bone quality that might be inferred from the dispersion itself. Thus, a better understanding of phase velocity might aid in addressing frequency-dependent sources of error in group velocity measurements, as well as provide additional diagnostic criteria.

Dispersion is not believed to be incorporated into any clinical device technology; the current literature consists almost exclusively of *in vitro* studies, although at least one *in vivo* study exists (Wear, 2007b). Phase velocity is typically calculated by

comparing the unwrapped phase of a signal transmitted through bone to that of a signal that has propagated through a non-dispersive reference medium, such as water.

Using this phase spectroscopy approach, the phase velocity is given by

$$v_p(f) = v_h \left[1 - \frac{v_h \Delta\phi(f)}{d} \frac{1}{2\pi f} \right]^{-1}, \quad (2.2)$$

where $v_p(f)$ is the phase velocity at frequency f , v_h is the velocity in the host medium, d is the sample thickness, and $\Delta\phi(f)$ is the difference in phase between the two signal spectra.

Despite the straightforward nature of computing phase velocity, its use in practice is complicated by a poor understanding of the physics that give rise to the dispersion observed in cancellous bone. One notable example is the conflict between experimentally observed dispersions and dispersions predicted by the Kramers-Kronig relations.

2.4.1 Negative dispersion

The Kramers-Kronig (KK) relations mathematically connect the real and imaginary parts of causal and square-integrable transfer functions, and can be applied to the complex wave number in ultrasonic wave propagation. The result is that phase velocity $c(f)$ can be derived from knowledge of the attenuation coefficient $\alpha(f)$ and vice versa. The so-called nearly-local approximation to the integral acoustic Kramers-Kronig relations is given by (O'Donnell *et al.*, 1981; Waters *et al.*, 2003, 2005; Mobley *et al.*, 2005)

$$\alpha(f) - \alpha(f_0) \approx -\frac{\pi}{2} (2\pi f)^2 \frac{d}{df} \left(\frac{1}{c(f)} \right). \quad (2.3)$$

This approximation has been shown to be valid for media with an attenuation coefficient that increases linearly with frequency; that is,

$$\alpha(f) = \beta f, \quad (2.4)$$

where β is the slope of the attenuation coefficient. The parameter β is analogous to normalized Broadband Ultrasound Attenuation in the bone sonometry community.

In cases of small dispersion, Eq. (2.3) can be further simplified to

$$c(f) \approx c(f_0) + \frac{1}{\pi^2} c(f_0)^2 \beta \ln \left(\frac{f}{f_0} \right), \quad (2.5)$$

where f_0 is a chosen reference frequency. Thus, for media that exhibit a linear relationship between attenuation and phase velocity, the dispersion is predicted to increase logarithmically; that is, the dispersion is expected to be positive. The attenuation coefficient of cancellous bone is well established to have a linear dependence on frequency; the reliance on BUA as a clinically relevant parameter testifies to this fact. Nevertheless, many studies of cancellous bone have found that phase velocity decreases with increasing frequency, a phenomenon first described by our Laboratory as anomalous negative dispersion (Droin *et al.*, 1998; Wear, 2005, 2007b, 2009a; Haiat *et al.*, 2006; Marutyan *et al.*, 2006; Pakula *et al.*, 2009). An illustration of the inconsistency between the Kramers-Kronig predictions and experimental measurements is depicted in Fig. 2.4, where attenuation coefficient and phase velocity measurements for a human calcaneus specimen prepared in our Laboratory are displayed. The attenuation coefficient (Panel A) rises linearly with frequency over the experimental bandwidth. The dispersion predicted by the Kramers-Kronig relations using the

attenuation coefficient (Panel B, gray line) has a markedly different frequency dependence from the measured dispersion (Panel B, black circles). It is on this basis of results such as these that negative dispersion in bone is referred to as “anomalous”.

2.4.2 Theoretical explanations for negative dispersion

The apparent contradiction between the Kramers-Kronig relations and experimental measurements has led to several proposals to resolve the conflict. As yet, there is no consensus on which, if any, of the proposed solutions contribute significantly to the observed effect. One approach is to modify or extend the way that the Kramers-Kronig relations apply to data acquired on cancellous bone. Waters and Hoffmeister (2005) suggested an extension of the Kramers-Kronig relations using the method of subtractions. The twice-subtracted Kramers-Kronig relations can predict negative dispersion, but this technique requires the introduction of additional adjustable parameters into the formalism. The physical role of the additional parameters is unclear.

Other approaches involve more sophisticated physical theories of ultrasonic wave propagation in porous media to predict negative dispersion. Haïat *et al.* showed that multiple scattering from trabeculae coupled with absorption mechanisms could result in negative dispersion (Haïat *et al.*, 2008a), and Chakraborty suggested a non-local modification to the widely-used Biot theory for wave propagation in poroelastic media that also predicts a decrease in phase velocity with frequency (Chakraborty, 2008).

Still another explanation, described in detail in this Dissertation, is that negative dispersion can result from analyzing data acquired on cancellous bone as if only one

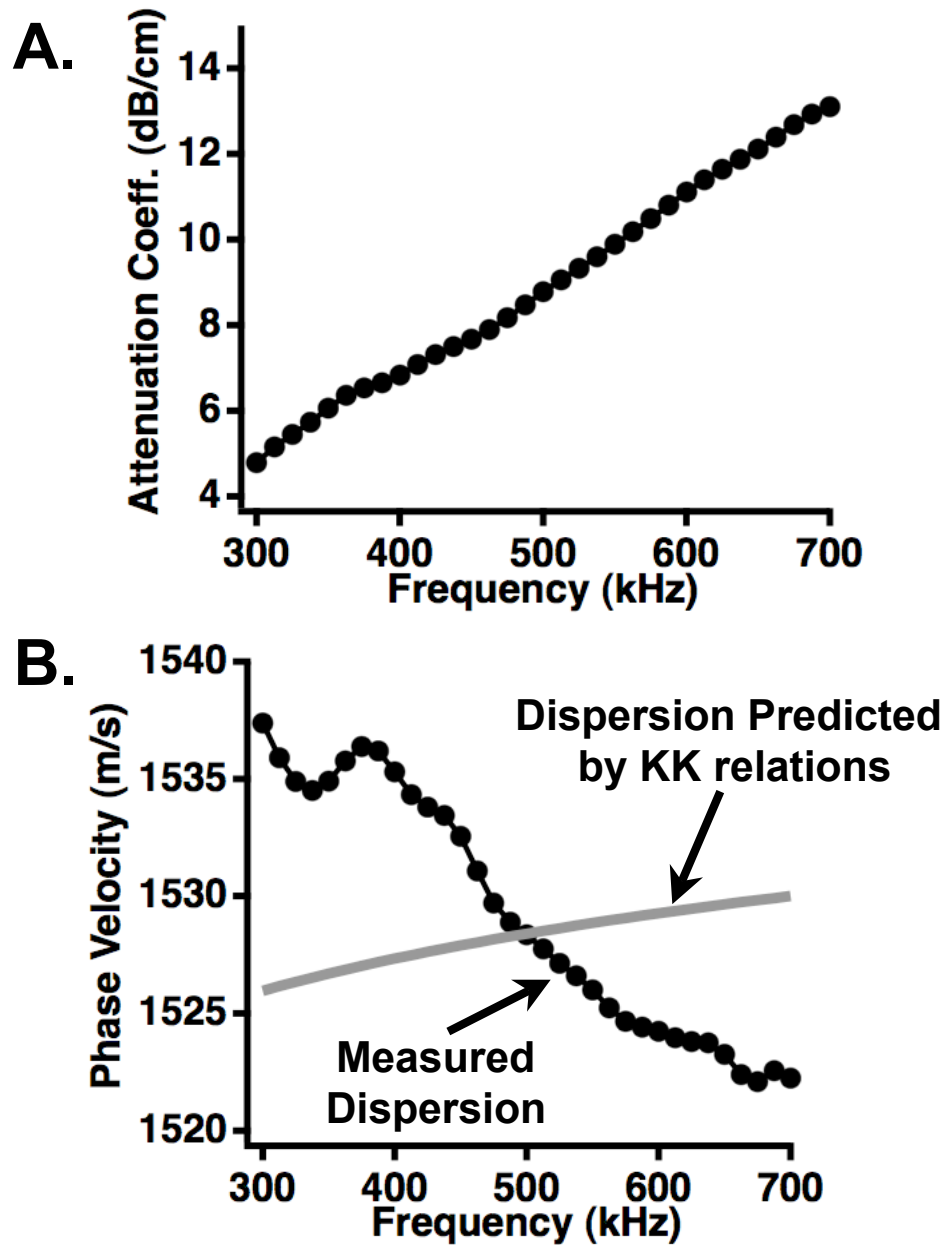


FIGURE 2.4: Attenuation coefficient (Panel A) and phase velocity (Panel B) as for an excised human calcaneus specimen. Measurements were performed in the Laboratory for Ultrasonics. The attenuation coefficient is approximately linear with frequency. According to the Kramers-Kronig relations, the phase velocity should rise logarithmically with frequency (gray curve); however, the measured dispersion is negative (black circles).

compressional wave is present, when in fact multiple overlapping waves comprise the acquired signal (Marutyan *et al.*, 2006; Anderson *et al.*, 2008). More information on this proposal is given in the following section and in Chapter 3.

2.4.3 Fast and slow compressional waves in bone

Multiple compressional acoustic wave modes have been known to propagate in porous media for several decades. The theory of Biot was formulated in the early 1950s in a geophysical context to describe acoustic wave propagation in fluid-saturated porous rock (Biot, 1956a,b). The theory predicts the existence of two compressional waves, which Biot referred to as a “wave of the first kind” and a “wave of the second kind” but have in recent times often been referred to as “fast” and “slow”. Biot theory was first applied to cancellous bone by McKelvie and Palmer (McKelvie and Palmer, 1991), and has since been used extensively to model bone (Pakula *et al.*, 2008; Sebaa *et al.*, 2008; Fellah *et al.*, 2008; Wear *et al.*, 2005; Haire and Langton, 1999; Hosokawa and Otani, 1998; Williams, 1992). A modified Biot-Attenborough (MBA) model has also been developed for a medium with cylindrical pores and applied to bone (Lee *et al.*, 2003, 2007). Mathematical details of Biot theory and the MBA model are presented in Chapter 3.

Schoenberg introduced an alternative theory applicable to a periodic layered fluid-solid structure (Schoenberg, 1984; Plona *et al.*, 1987). This theory also predicts the existence of two compressional waves, and has also been shown to predict negative dispersion (Wear, 2001). Schoenberg theory has been successfully applied to cancel-

lous bone independently and in conjunction with Biot theory (Hughes *et al.*, 1999; Wear, 2001; Hughes *et al.*, 2007; Lee *et al.*, 2007), but the ability to accurately model the complex architecture of cancellous bone as a rigorous periodic layered structure is somewhat limited for most experimental circumstances.

Fast and slow waves were first observed in cortical bone by Lakes *et al.* (1983). Subsequently, fast and slow waves were reported in transmission studies of cancellous bone by Hosokawa and Otani (1997) and later by other investigators (Mizuno *et al.*, 2009; Haiat *et al.*, 2008b; Padilla and Laugier, 2000; Lee *et al.*, 2007). In some experiments, the fast and slow waves are separated in time and are individually discernible in the acquired signal. In other cases, the two waves overlap in the time-domain data. The consequences of overlapping fast and slow waves to calculations of phase velocity are discussed in the following Chapter.

Bibliography

- Anderson, C. C., Marutyan, K. R., Holland, M. R., Wear, K. A., and Miller, J. G. (2008). “Interference between wave modes may contribute to the apparent negative dispersion observed in cancellous bone”, *J Acoust Soc Am* **124**, 1781–9.
- at, G. H., Padilla, F., Barkmann, R., Kolta, S., Latremouille, C., Gluer, C., and Laugier, P. (2005). “In vitro speed of sound measurement at intact human femur specimens”, *Ultrasound Med Biol* **31**, 987–996.
- Barkmann, R., Laugier, P., Moser, U., Dencks, S., Klausner, M., Padilla, F., Haiat, G., Heller, M., and Glüer, C.-C. (2008). “In vivo measurements of ultrasound transmission through the human proximal femur”, *Ultrasound Med Biol* **34**, 1186–90.
- Biot, M. (1956a). “Theory of propagation of elastic waves in a fluidsaturated porous solid. I. lowfrequency range”, *J Acoust Soc Am* **28**, 168–178.
- Biot, M. (1956b). “Theory of propagation of elastic waves in a fluidsaturated porous solid. II. higher frequency range”, *J Acoust Soc Am* **28**, 179–191.
- Bonnick, S. L. (2004). *Bone Densitometry in Clinical Practice* (Humana Press).
- Canalis, E., McCarthy, T., and Centrella, M. (1988). “Growth factors and the regulation of bone remodeling”, *J Clin Invest* **81**, 277–81.
- Chakraborty, A. (2008). “Prediction of negative dispersion by a nonlocal poroelastic theory”, *J Acoust Soc Am* **123**, 56–67.
- Cummings, S. R. and Black, D. (1995). “Bone mass measurements and risk of fracture in caucasian women: a review of findings from prospective studies”, *Am J Med* **98**, 24S–28S.
- Droin, P., Berger, G., and Laugier, P. (1998). “Velocity dispersion of acoustic waves in cancellous bone”, *IEEE Trans Ultrason Ferroelectr Freq Control* **45**, 581–92.
- Fellah, Z., Sebaa, N., Fellah, M., Mitri, F., Ogam, E., Lauriks, W., and Depollier, C. (2008). “Application of the biot model to ultrasound in bone: direct problem”, *IEEE Trans Ultrason Ferroelectr Freq Control* **55**, 1508 – 1515.
- Garnero, P., Dargent-Molina, P., Hans, D., Schott, A. M., Bréart, G., Meunier, P. J., and Delmas, P. D. (1998). “Do markers of bone resorption add to bone mineral density and ultrasonographic heel measurement for the prediction of hip fracture in elderly women? the epidios prospective study”, *Osteoporos Int* **8**, 563–9.

- Goossens, L., Vanderoost, J., Jaecques, S., Boonen, S., D’hooge, J., Lauriks, W., and der Perre, G. V. (2008). “The correlation between the sos in trabecular bone and stiffness and density studied by finite-element analysis”, *IEEE Trans Ultrason Ferroelectr Freq Control* **55**, 1234 – 1242.
- Haïat, G., Lhémery, A., Renaud, F., Padilla, F., Laugier, P., and Naili, S. (2008a). “Velocity dispersion in trabecular bone: influence of multiple scattering and of absorption”, *J Acoust Soc Am* **124**, 4047–58.
- Haïat, G., Padilla, F., Cleveland, R. O., and Laugier, P. (2006). “Effects of frequency-dependent attenuation and velocity dispersion on in vitro ultrasound velocity measurements in intact human femur specimens”, *IEEE Trans Ultrason Ferroelectr Freq Control* **53**, 39–51.
- Haïat, G., Padilla, F., Peyrin, F., and Laugier, P. (2008b). “Fast wave ultrasonic propagation in trabecular bone: numerical study of the influence of porosity and structural anisotropy”, *J Acoust Soc Am* **123**, 1694–705.
- Haire, T. J. and Langton, C. M. (1999). “Biot theory: a review of its application to ultrasound propagation through cancellous bone”, *Bone* **24**, 291–5.
- Hans, D., Dargent-Molina, P., Schott, A. M., Sebert, J. L., Cormier, C., Kotzki, P. O., Delmas, P. D., Pouilles, J. M., Breart, G., and Meunier, P. J. (1996). “Ultrasonographic heel measurements to predict hip fracture in elderly women: the epidios prospective study”, *Lancet* **348**, 511–4.
- Hans, D. and Krieg, M. (2008). “The clinical use of quantitative ultrasound (QUS) in the detection and management of osteoporosis”, *IEEE Trans Ultrason Ferroelectr Freq Control* **55**, 1529 – 1538.
- Hodgskinson, R., Njeh, C. F., Whitehead, M. A., and Langton, C. M. (1996). “The non-linear relationship between bua and porosity in cancellous bone”, *Phys Med Biol* **41**, 2411–20.
- Hosokawa, A. and Otani, T. (1997). “Ultrasonic wave propagation in bovine cancellous bone”, *J Acoust Soc Am* **101**, 558–62.
- Hosokawa, A. and Otani, T. (1998). “Acoustic anisotropy in bovine cancellous bone”, *J Acoust Soc Am* **103**, 2718–22.
- Hughes, E. R., Leighton, T. G., Petley, G. W., and White, P. R. (1999). “Ultrasonic propagation in cancellous bone: a new stratified model”, *Ultrasound Med Biol* **25**, 811–21.
- Hughes, E. R., Leighton, T. G., White, P. R., and Petley, G. W. (2007). “Investigation of an anisotropic tortuosity in a biot model of ultrasonic propagation in cancellous bone.”, *J Acoust Soc Am* **121**, 568–574.

- Johnell, O., Kanis, J. A., Oden, A., Johansson, H., Laet, C. D., Delmas, P., Eisman, J. A., Fujiwara, S., Kroger, H., Mellstrom, D., Meunier, P. J., Melton, L. J., O'Neill, T., Pols, H., Reeve, J., Silman, A., and Tenenhouse, A. (2005). "Predictive value of BMD for hip and other fractures", *J Bone Miner Res* **20**, 1185–94.
- Kanis, J. A. (1994). "Assessment of fracture risk and its application to screening for postmenopausal osteoporosis: synopsis of a who report", *Osteoporos Int* **4**, 368–81.
- Kanis, J. A. (2002). "Diagnosis of osteoporosis and assessment of fracture risk", *Lancet* **359**, 1929–36.
- Kanis, J. A., Oden, A., Johnell, O., Johansson, H., Laet, C. D., Brown, J., Burckhardt, P., Cooper, C., Christiansen, C., Cummings, S., Eisman, J. A., Fujiwara, S., Glüer, C., Goltzman, D., Hans, D., Krieg, M.-A., Croix, A. L., McCloskey, E., Mellstrom, D., Melton, L. J., Pols, H., Reeve, J., Sanders, K., Schott, A.-M., Silman, A., Torgerson, D., van Staa, T., Watts, N. B., and Yoshimura, N. (2007). "The use of clinical risk factors enhances the performance of BMD in the prediction of hip and osteoporotic fractures in men and women", *Osteoporos Int* **18**, 1033–46.
- Lakes, R., Yoon, H. S., and Katz, J. L. (1983). "Slow compressional wave propagation in wet human and bovine cortical bone", *Science* **220**, 513–515.
- Langton, C. and Njeh, C. (2008). "The measurement of broadband ultrasonic attenuation in cancellous bone—a review of the science and technology", *IEEE Trans Ultrason Ferroelectr Freq Control* **55**, 1546 – 1554.
- Langton, C. M. and Hodgkinson, R. (1997). "The in vitro measurement of ultrasound in cancellous bone", *Stud Health Technol Inform* **40**, 175–199.
- Langton, C. M., Palmer, S. B., and Porter, R. W. (1984). "The measurement of broadband ultrasonic attenuation in cancellous bone", *Eng Med* **13**, 89–91.
- Laval-Jeantet, A. M., Bergot, C., Carroll, R., and Garcia-Schaefer, F. (1983). "Cortical bone senescence and mineral bone density of the humerus", *Calcif Tissue Int* **35**, 268–72.
- Lee, K. I., Hughes, E. R., Humphrey, V. F., Leighton, T. G., and Choi, M. J. (2007). "Empirical angle-dependent biot and mba models for acoustic anisotropy in cancellous bone.", *Phys Med Biol* **52**, 59–73.
- Lee, K. I., Roh, H.-S., and Yoon, S. W. (2003). "Acoustic wave propagation in bovine cancellous bone: application of the modified biot-attenborough model", *J Acoust Soc Am* **114**, 2284–93.
- Manolagas, S. C. and Jilka, R. L. (1995). "Bone marrow, cytokines, and bone remodeling: emergin insights into the pathophysiology of osteoporosis", *N Engl J Med* **332**, 305–11.

- Marutyan, K. R., Holland, M. R., and Miller, J. G. (2006). “Anomalous negative dispersion in bone can result from the interference of fast and slow waves”, *J Acoust Soc Am* **120**, EL55–61.
- McKelvie, M. L. and Palmer, S. B. (1991). “The interaction of ultrasound with cancellous bone”, *Phys Med Biol* **36**, 1331–40.
- Mizuno, K., Matsukawa, M., Otani, T., Laugier, P., and Padilla, F. (2009). “Propagation of two longitudinal waves in human cancellous bone: an in vitro study”, *J Acoust Soc Am* **125**, 3460–6.
- Mobley, J., Waters, K. R., and Miller, J. G. (2005). “Causal determination of acoustic group velocity and frequency derivative of attenuation with finite-bandwidth Kramers-Kronig relations”, *Phys Rev E* **72**, 016604.
- NIH (2001). “Osteoporosis prevention, diagnosis, and therapy”, *JAMA* **285**, 785–95.
- Njeh, C. F., Hans, D., Fuerst, T., Glüer, C.-C., and Genant, H. K. (1999). *Quantitative Ultrasound: Assessment of Osteoporosis and Bone Status* (Martin Dunitz Ltd).
- O’Donnell, M., Jaynes, E. T., and Miller, J. G. (1981). “Kramers-Kronig relationship between ultrasonic attenuation and phase velocity”, *J Acoust Soc Am* **69**, 696–701.
- Padilla, F. and Laugier, P. (2000). “Phase and group velocities of fast and slow compressional waves in trabecular bone”, *J Acoust Soc Am* **108**, 1949–52.
- Pakula, M., Padilla, F., and Laugier, P. (2009). “Influence of the filling fluid on frequency-dependent velocity and attenuation in cancellous bones between 0.35 and 2.5 mhz”, *J Acoust Soc Am* **126**, 3301–3310.
- Pakula, M., Padilla, F., Laugier, P., and Kaczmarek, M. (2008). “Application of biot’s theory to ultrasonic characterization of human cancellous bones: determination of structural, material, and mechanical properties”, *J Acoust Soc Am* **123**, 2415–23.
- Parfitt, A. M. (1994). “Osteonal and hemi-osteonal remodeling: the spatial and temporal framework for signal traffic in adult human bone”, *J Cell Biochem* **55**, 273–86.
- Petley, G. W., Robins, P. A., and Aindow, J. D. (1995). “Broadband ultrasonic attenuation: are current measurement techniques inherently inaccurate?”, *Br J Radiol* **68**, 1212–4.
- Plona, T., Winkler, K., and Schoenberg, M. (1987). “Acoustic waves in alternating fluid/solid layers”, *J Acoust Soc Am* **81**, 1227–1234.

- Schoenberg, M. (1984). “Wave propagation in alternating solid and fluid layers”, *Wave Motion* **6**, 303–320.
- Sebaa, N., Fellah, Z., Fellah, M., Ogam, E., Mitri, F., Depollier, C., and Lauriks, W. (2008). “Application of the biot model to ultrasound in bone: inverse problem”, *IEEE Trans Ultrason Ferroelectr Freq Control* **55**, 1516 – 1523.
- Strelitzki, R., Metcalfe, S. C., Nicholson, P. H., Evans, J. A., and Paech, V. (1999). “On the ultrasonic attenuation and its frequency dependence in the os calcis assessed with a multielement receiver”, *Ultrasound Med Biol* **25**, 133–41.
- Strelitzki, R., Nicholson, P. H., and Evans, J. A. (1997). “Low-frequency ultrasonic velocity measurements in human calcaneal trabecular bone”, *Physiol Meas* **18**, 119–27.
- Thomsen, J. S., Ebbesen, E. N., and Mosekilde, L. I. (2002). “Age-related differences between thinning of horizontal and vertical trabeculae in human lumbar bone as assessed by a new computerized method”, *Bone* **31**, 136–42.
- Ulrich, D., van Rietbergen, B., Laib, A., and R uegsegger, P. (1999). “The ability of three-dimensional structural indices to reflect mechanical aspects of trabecular bone”, *Bone* **25**, 55–60.
- Waters, K., Hughes, M., Mobley, J., and Miller, J. (2003). “Differential forms of the Kramers-Kronig dispersion relations”, *IEEE Trans Ultrason Ferroelectr Freq Control* **50**, 68 – 76.
- Waters, K., Mobley, J., and Miller, J. (2005). “Causality-imposed (Kramers-Kronig) relationships between attenuation and dispersion”, *IEEE Trans Ultrason Ferroelectr Freq Control* **52**, 822 – 823.
- Waters, K. R. and Hoffmeister, B. K. (2005). “Kramers-Kronig analysis of attenuation and dispersion in trabecular bone”, *J Acoust Soc Am* **118**, 3912–20.
- Wear, K. (2001). “A stratified model to predict dispersion in trabecular bone”, *IEEE Trans Ultrason Ferroelectr Freq Control* **48**, 1079 – 1083.
- Wear, K. A. (2005). “The dependencies of phase velocity and dispersion on trabecular thickness and spacing in trabecular bone-mimicking phantoms”, *J Acoust Soc Am* **118**, 1186–92.
- Wear, K. A. (2007a). “The dependence of time-domain speed-of-sound measurements on center frequency, bandwidth, and transit-time marker in human calcaneus in vitro”, *J Acoust Soc Am* **122**, 636–44.
- Wear, K. A. (2007b). “Group velocity, phase velocity, and dispersion in human calcaneus in vivo”, *J Acoust Soc Am* **121**, 2431–7.

- Wear, K. A. (2008). “Mechanisms for attenuation in cancellous-bone-mimicking phantoms”, *IEEE Trans Ultrason Ferroelectr Freq Control* **55**, 2418–25.
- Wear, K. A. (2009a). “The dependencies of phase velocity and dispersion on volume fraction in cancellous-bone-mimicking phantoms”, *J Acoust Soc Am* **125**, 1197–201.
- Wear, K. A. (2009b). “Frequency dependence of average phase shift from human calcaneus in vitro”, *J Acoust Soc Am* **126**, 3291–3300.
- Wear, K. A., Laib, A., Stuber, A. P., and Reynolds, J. C. (2005). “Comparison of measurements of phase velocity in human calcaneus to biot theory”, *J Acoust Soc Am* **117**, 3319–24.
- WHO (1994). “Assessment of fracture risk and its application to screening for postmenopausal osteoporosis”, *World Health Organ Tech Rep Ser* **843**, 1–129.
- WHO (2004). “Prevention and management of osteoporosis”, *World Health Organ Tech Rep Ser* **921**, 206.
- Williams, J. L. (1992). “Ultrasonic wave propagation in cancellous and cortical bone: prediction of some experimental results by Biot’s theory”, *J Acoust Soc Am* **91**, 1106–12.

CHAPTER 3

THE EFFECT OF INTERFERING FAST AND SLOW WAVES ON DISPERSION IN CANCELLOUS BONE

3.1 Preface

This Chapter is based on the peer-reviewed journal article “Interference between wave modes may contribute to the apparent negative dispersion observed in cancellous bone” written by Christian C. Anderson, Karen R. Marutyan, Mark R. Holland, Keith A. Wear, and James G. Miller and published in *The Journal of the Acoustical Society of America*, Vol. 124, No. 3, pp. 1781-89.

3.2 Abstract

Previous work has shown that ultrasonic waves propagating through cancellous bone often exhibit a linear-with-frequency attenuation coefficient, but a decrease in phase velocity with frequency (negative dispersion) that is inconsistent with the causality-imposed Kramers-Kronig relations. In the current study, interfering wave modes similar to those observed in bone are shown to potentially contribute to the observed negative dispersion. Biot theory, the Modified Biot-Attenborough model, and experimental results are used to aid in simulating multiple-mode wave propagation through cancellous bone. Simulations entail constructing individual wave modes exhibiting a positive dispersion using plausible velocities and amplitudes, and then summing the individual modes to create mixed-mode output waveforms. Results of the simulations indicate that mixed-mode waveforms can exhibit negative dispersion when analyzed conventionally under the assumption that only one wave is present, even when the individual interfering waves exhibit positive dispersions in accordance with the Kramers-Kronig relations. Furthermore, negative dispersion is observed when little or no visual evidence of interference exists in the time-domain data. Understanding the mechanisms responsible for the observed negative dispersion could aid in determining the true material properties of cancellous bone, as opposed to the apparent properties measured using conventional data analysis techniques.

3.3 Introduction

There is considerable interest in the use of ultrasound to evaluate bone quality, with investigations of cancellous (trabecular) bone playing a prominent role. Cancellous bone consists of a network of (hard) calcified strands (trabeculae) through which courses (soft) bone marrow. Methods for characterizing bone tissue using ultrasound often consist of measurements of the velocity and attenuation properties of ultrasonic waves transmitted through the trabecular network (Droin *et al.*, 1998; Wear, 2000; Hoffmeister *et al.*, 2000; Wear, 2007; Apostolopoulos and Deligianni, 2008).

The intricate structure of cancellous bone tissue can complicate measurements. The material architecture is anisotropic, with the trabeculae predominantly oriented along the direction of stresses experienced by the bone. Consequently, acquired ultrasonic data depend on the angle of insonification relative to the predominant trabecular orientation (Hosokawa and Otani, 1998; Lee *et al.*, 2007a; Hughes *et al.*, 2007). A large number of ultrasonic investigations of cancellous bone reported in the literature are performed on bovine leg bones or on human calcanei. In bovine leg bones, insonification is approximately perpendicular to the trabeculae in the medial-lateral (ML) and anterior-posterior (AP) directions, and approximately parallel in the superior-inferior (SI) direction. Human calcanei are typically insonified in the ML direction, corresponding to the perpendicular orientation.

The porous structure of cancellous bone supports the propagation of two compressional ultrasonic waves, often denoted as a fast wave and a slow wave (Hosokawa

and Otani, 1998; Padilla and Laugier, 2000; Lee *et al.*, 2003). Depending on experimental circumstances, such as the porosity and thickness of the bone sample and the insonification angle relative to the predominant trabecular orientation, the two waves are sometimes separate and visibly distinct in the time-domain radiofrequency (RF) data; in other instances, only one wave is observed. One possible contributing factor for the observation of a single wave in certain cases is that the difference in the arrival times of the fast and slow waves is small compared to the temporal extent of the ultrasonic pulse, resulting in an RF trace that appears to be that of a single wave but is in fact the sum of interfering fast and slow waves. In their investigations of anisotropy in bovine cancellous bone, Hosokawa and Otani noted that the propagation speeds of the fast and slow waves converge as the incident ultrasonic field becomes aligned perpendicular to the predominant trabecular orientation, resulting in overlap of the fast and slow waves in the received RF trace (Hosokawa and Otani, 1998). Padilla and Laugier identified the overlap of fast and slow waves as a complicating factor in their study of a stratified model for bone (Padilla and Laugier, 2000). Lee *et al.* reported that in the medial-lateral (ML) direction, fast and slow waves in bovine tibia overlap and "are observed as if one longitudinal wave propagates" (Lee *et al.*, 2003). Haiat *et al.* also noted the difficulties associated with multiple-mode propagation (Haiat *et al.*, 2008).

In general, investigators have found that the attenuation coefficient of bone varies linearly or quasi-linearly with frequency, and typically report attenuation measurements as the rate of change in attenuation coefficient with frequency (Droin *et al.*,

1998; Waters and Hoffmeister, 2005). This parameter is known as *Broadband Ultrasound Attenuation* (BUA) or, if normalized by sample thickness, as *normalized Broadband Ultrasound Attenuation* (nBUA), also known as *slope of attenuation*. However, despite the consensus on the frequency dependence of attenuation coefficient, there is considerable variation in measurements of the frequency dependence of phase velocity. Many laboratories report that on average, the phase velocity of ultrasonic waves propagating through cancellous bone decreases with increasing frequency, a phenomenon known as negative dispersion (Droin *et al.*, 1998; Wear, 2000, 2007; Nicholson *et al.*, 1996). However, an increase in phase velocity with frequency (positive dispersion) is observed in 10 to 20 percent of investigated sites (Wear, 2000; Droin *et al.*, 1998).

The observed negative dispersion in the majority of bone samples analyzed is further confounded when one considers the apparent inconsistencies with the causality-imposed Kramers-Kronig (KK) relations that relate attenuation to dispersion (O'Donnell *et al.*, 1981; Waters *et al.*, 2000, 2005; Waters and Hoffmeister, 2005; Mobley *et al.*, 2005). According to the nearly-local approximation to the KK relations with one subtraction, an *increase* in phase velocity with frequency is expected for samples exhibiting an approximately linear-with-frequency attenuation coefficient. If the attenuation coefficient varied strictly linearly with frequency, the dispersion curve would be positive and logarithmic (Waters and Hoffmeister, 2005; Waters *et al.*, 2000, 2005). The inconsistencies with the KK relations are especially troubling in light of evidence that they are valid even under conditions in which the attenuation coefficient and phase velocity exhibit complicated behavior (Bauer *et al.*, 2007).

Currently, dispersion is not a widely used metric for clinical bone quality analysis. However, the negative dispersion measured in cancellous bone suggests that evaluating the material properties of bone using current data analysis techniques may be compromised because they result in the measurement of "apparent" material properties instead of the underlying "true" material properties. Consequently, a better understanding of the dispersion characteristics of cancellous bone, including the mechanisms responsible for the observed negative dispersion, could aid in determining the true material properties of cancellous bone, as opposed to the apparent properties measured using conventional data analysis techniques.

In a previous Letter, our laboratory proposed that negative dispersion in cancellous bone can arise when radiofrequency (RF) signals consisting of overlapped fast and slow waves are analyzed as if they are a single longitudinal wave (Marutyan *et al.*, 2006). In the current investigation, this proposed mechanism is extended and enhanced by using theoretical and experimental results of ultrasonic wave propagation in bone obtained by previous investigators as a basis to generate simulated fast and slow waves that are consistent with the nearly-local approximation to the KK relations. The simulated fast and slow waves are then used to create a "mixed" waveform consisting of overlapping fast and slow waves, and it is then demonstrated that analyzing the mixed waveforms may contribute to the observed negative dispersion in cancellous bone.

3.4 Theory

Theories of wave propagation in bone were considered to aid in determining appropriate input values for the parameters used in the simulations. Ultrasonic wave velocity in bone has been extensively modeled using Biot theory (Biot, 1956a,b; Haire and Langton, 1999; Fella *et al.*, 2004; Sebaa *et al.*, 2006; Hughes *et al.*, 2007; Wear *et al.*, 2005; Williams, 1992; Hosokawa and Otani, 1997; Lee *et al.*, 2007a; Chakraborty, 2008), Modified Biot-Attenborough theory (Roh and Yoon, 2004; Lee *et al.*, 2003, 2007a,b), and stratified media theory (Hughes *et al.*, 1999; Wear, 2001; Lin *et al.*, 2001; Padilla and Laugier, 2000; Plona *et al.*, 1987; Lee *et al.*, 2007a). Each of these models predicts the existence of fast and slow waves; however, the stratified model predicts that only the fast wave propagates at perpendicular insonification. Because the simulations involve two propagating compressional waves, the stratified model was not explored in this study. It should be noted, however, that actual bone structures are unlikely to be rigorously perpendicular to ultrasound wave propagation at any orientation, resulting in the presence of multiple modes even for nominally perpendicular orientations.

The Biot and Modified Biot-Attenborough models are typically used to predict the phase velocities of fast and slow waves as functions of porosity, defined as (1 - volume fraction of bone). Each model has been empirically extended to include angle-dependent parameters to account for the anisotropy of cancellous bone (Lee *et al.*, 2007a). Because the existing literature includes slightly different implementations of

TABLE 3.1: Biot theory and modified Biot theory parameters used to compute the velocities used in the simulations of wave propagation. The calculated velocities are displayed as a function of porosity in Fig. 3.1.

Parameter	Biot	Modified Biot
Solid density (ρ_s)	1960 kg/m ³	1960 kg/m ³
Fluid density (ρ_f)	1000 kg/m ³	1000 kg/m ³
Young's modulus of solid (E_s)	20 GPa	
Bulk modulus of fluid (K_f)	2.28 GPa	
Poisson's ratio for solid (ν_s)	0.32	
Poisson's ratio for skeletal frame (ν_b)	0.32	
Tortuosity (α_{tort})	Equation 3.7	1
Fluid viscosity (η)	10 ⁻³ Pa s	
Viscous characteristic length (Λ)	5 μ m	
Exponent (n)	1.23 (parallel) 2.35 (perpendicular)	
Fluid compressional speed (c_f)		1500 m/s
Solid compressional speed (c_s)		3800 m/s
Kinematic viscosity of fluid (ν)		1 \times 10 ⁻⁶ m ² /s
Specific heat ratio of fluid (γ)		1.004
Prandtl number of fluid (N_{Pr})		7
Pore radius (a)		0.5 mm
Boundary condition parameter (s_1)		1.5
Phase velocity parameter (s_2)		0.5 (parallel) 1.7 (perpendicular)

each theory, details of the theoretical formalisms used to calculate phase velocities are included below.

3.4.1 Biot theory

Biot theory considers the motions of the fluid and solid components of a porous material. Input parameters consist of physical and mechanical properties of the fluid and solid components of the propagation medium. The input parameters are used to predict fast and slow compressional waves corresponding to in-phase and out-of-phase motion between the fluid and solid. Energy losses are due to viscous interactions at interfaces.

Biot theory gives rise to three elastic parameters P , Q , and R given by

$$P = \frac{\beta_{por} \left(\frac{K_s}{K_f} - 1 \right) K_b + \beta_{por}^2 K_s + (1 - 2\beta_{por}) (K_s - K_b)}{D} + \frac{4\mu_b}{3} \quad (3.1a)$$

$$Q = \frac{(1 - \beta_{por} - \frac{K_b}{K_s})\beta_{por} K_s}{D} \quad (3.1b)$$

$$R = \frac{K_s \beta_{por}^2}{D} \quad (3.1c)$$

where $D = 1 - \beta_{por} - \frac{K_b}{K_s} + \beta_{por} \frac{K_s}{K_f}$ and K_s is the bulk modulus of the solid material, K_f is the bulk modulus of the fluid, K_b is the bulk modulus of the elastic frame, μ_b is the shear modulus of the elastic frame, and β_{por} is porosity (volume fraction of fluid).

If the solid material is assumed to be isotropic, the bulk modulus K_s can be related to the intrinsic elastic parameters of the solid by

$$K_s = \frac{E_s}{3(1 - 2\nu_s)} \quad (3.2)$$

where E_s and ν_s are the Young's modulus and Poisson's ratio for the solid. The Young's modulus of the elastic frame of the porous structure E_b is determined from the porosity and E_s through the power law relationship

$$E_b = E_s(1 - \beta_{por})^n. \quad (3.3)$$

If the frame is assumed to be isotropic, its bulk and shear moduli K_b and μ_b can be written as

$$K_b = \frac{E_b}{3(1 - 2\nu_b)} \quad (3.4)$$

$$\mu_b = \frac{E_b}{2(1 + \nu_b)} \quad (3.5)$$

where ν_b is Poisson's ratio for the frame.

Although Biot theory assumes an isotropic medium, it has been empirically extended to apply to anisotropic porous materials through exploitation of the power law relationship between E_b and E_s . The exponent n in Eq. (3.3) depends on the angle of insonification relative to trabecular alignment. Hosokawa and Otani found $n = 1.46$ in the parallel orientation, and $n = 2.14$ in the perpendicular direction (Hosokawa and Otani, 1998). Williams found that n has a value of 1.23 when cancellous bone is insonified parallel to the trabeculae, and a value of 2.35 when insonification is perpendicular to the trabeculae (Williams, 1992). Those values for n were adopted by Lee *et al.* to construct an angle-dependent Biot model (Lee *et al.*, 2007a). In the current study, the values established by Williams and later employed by Lee *et al.* were used in the Biot theory calculations.

Biot theory also includes mass coefficients to allow for viscous and inertial drag

effects. These coefficients are given by

$$\rho_{11} + \rho_{12} = (1 - \beta_{por})\rho_s \quad (3.6a)$$

$$\rho_{22} + \rho_{12} = \beta_{por}\rho_f \quad (3.6b)$$

$$\rho_{12} = -(\alpha_{tort}(\omega) - 1)\beta_{por}\rho_f \quad (3.6c)$$

where ρ_f and ρ_s are the densities of the fluid and solid components, and $\alpha_{tort}(\omega)$ is a structural factor known as the dynamic tortuosity. The subscript *tort* is used to distinguish the tortuosity ($\alpha_{tort}(\omega)$) from the attenuation coefficient ($\alpha(\omega)$). The dynamic tortuosity was introduced by Johnson, Koplik, and Dashen as

$$\alpha_{tort}(\omega) = \alpha_\infty \left[1 + \frac{2}{\Lambda} \left(\frac{i\eta}{\omega\rho_f} \right)^{1/2} \right] \quad (3.7)$$

in which Λ is the viscous characteristic length and η is the fluid viscosity (Johnson *et al.*, 1987). The tortuosity parameter α_∞ is given by

$$\alpha_\infty = 1 - s(1 - 1/\beta_{por}) \quad (3.8)$$

where s is a parameter derived from a microscopic model of a frame moving in a fluid. Other investigators have consistently let $s = 0.25$ (Williams, 1992; Hosokawa and Otani, 1998; Wear *et al.*, 2005; Lee *et al.*, 2007a).

The elastic parameters and mass coefficients are used to construct a characteristic equation given by

$$\begin{vmatrix} \omega^2\rho_{11} - k^2P & \omega^2\rho_{12} - k^2Q \\ \omega^2\rho_{12} - k^2Q & \omega^2\rho_{22} - k^2R \end{vmatrix} = 0 \quad (3.9)$$

whose roots are the wavenumbers of the fast and slow waves. The solutions are

$$k^2 = \omega^2 \left(\frac{B \pm \sqrt{B^2 - 4AC}}{2A} \right) \quad (3.10)$$

where

$$A = PR - Q^2 \quad (3.11a)$$

$$B = R\rho_{11} + P\rho_{22} - 2Q\rho_{12} \quad (3.11b)$$

$$C = \rho_{11}\rho_{22} - \rho_{12}^2. \quad (3.11c)$$

The phase velocities for the fast and slow waves are then calculated by $v_{phase} = \text{Re}(\omega/k)$, resulting in

$$v_{fast} = \text{Re} \left[\left(\frac{2A}{B - \sqrt{B^2 - 4AC}} \right)^{1/2} \right] \quad (3.12a)$$

$$v_{slow} = \text{Re} \left[\left(\frac{2A}{B + \sqrt{B^2 - 4AC}} \right)^{1/2} \right] \quad (3.12b)$$

where $\text{Re}()$ returns the real component of a complex number.

3.4.2 Modified Biot-Attenborough model

The Modified Biot-Attenborough model, proposed by Roh and Yoon, is a phenomenological approach for modeling wave propagation through a medium with cylindrical pores (Roh and Yoon, 2004; Lee *et al.*, 2003, 2007a,b). It allows for both viscous and thermal energy dissipation, but requires empirically-determined input parameters. Following the formulation given by Lee *et al.* (Lee *et al.*, 2007a), the equation of continuity for one-dimensional wave propagation through a circular cylindrical pore

is

$$-\rho_f \frac{\partial \langle v \rangle}{\partial x} = \frac{\partial \rho}{\partial t} \quad (3.13)$$

where ρ_f is the fluid density and $\langle v \rangle$ is the average particle velocity over the cross section of the pore. The equation of motion is given by

$$\frac{\partial p}{\partial x} = \rho_c(\omega) \frac{\partial \langle v \rangle}{\partial t} \quad (3.14)$$

where p is the acoustic pressure and $\rho_c(\omega)$ is the complex density given by

$$\rho_c(\omega) = \rho_f [1 - 2(\lambda e^{i\pi/2})^{-1} T'(\lambda e^{i\pi/2})]^{-1} \quad (3.15)$$

where

$$T'(\lambda e^{i\pi/2}) = \frac{J_1(\lambda e^{i\pi/2})}{J_0(\lambda e^{i\pi/2})} \quad (3.16)$$

in which J_0 and J_1 are the zero-order and first-order cylindrical Bessel functions. The dimensionless parameter λ is related to the size of the viscous boundary layer at the pore wall and may be written

$$\lambda(\omega) = a s_1 (\omega/\nu)^{1/2} \quad (3.17)$$

where a is the pore radius, ν is the kinematic viscosity of the fluid, and s_1 is a boundary condition parameter representing the pore frame rigidity.

When thermal effects are considered, the complex compressibility of the fluid $C_c(\omega)$ is given by

$$C_c(\omega) = (\gamma \rho_f c_f^2)^{-1} [1 + 2(\gamma - 1)(N_{Pr}^{1/2} \lambda e^{i\pi/2})^{-1} T'(N_{Pr}^{1/2} \lambda e^{i\pi/2})] \quad (3.18)$$

where c_f , γ , and N_{Pr} are the compressional speed, specific heat ratio, and Prandtl number of the fluid, respectively. When the model is extended to a material consisting of an ensemble of cylindrical pores, the wavenumber for the fast wave is given by

$$k_{fast} = \alpha_{tort} \left[\frac{k_c^2 k_s^2}{(1 - \beta_{por})^{s_2} k_c^2 + \beta_{por}^{s_2} k_s^2} \right]^{1/2} \quad (3.19)$$

where α_{tort} is tortuosity, β_{por} is porosity, $k_s = \omega/c_s$ is the wavenumber of the pore frame, s_2 is a phase velocity parameter, and k_c is the complex frequency-dependent wavenumber of the pore fluid given by

$$k_c(\omega) = \omega [C_c(\omega) \rho_c(\omega)]^{1/2} \quad (3.20)$$

The wavenumber for the slow wave is constructed in a similar fashion, under the assumption that the slow wave velocity tends to zero at low porosities. This wavenumber is given by

$$k_{slow} = \alpha_{tort} \left[\frac{k_c^2 k_g^2}{(1 - \beta_{por})^{s_2} k_c^2 + \beta_{por}^{s_2} k_g^2} \right]^{1/2} \quad (3.21)$$

where $k_g = \omega/c_g$ is the wavenumber of a hypothetical fluid with an extremely low (approaching zero) wave velocity. The phase velocities for the fast and slow waves are found using $v_{phase} = \text{Re}(\omega/k)$, resulting in

$$v_{fast} = \text{Re} \left(\frac{\omega}{\alpha_{tort}} \left[\frac{(1 - \beta_{por})^{s_2} k_c^2 + \beta_{por}^{s_2} k_s^2}{k_c^2 k_s^2} \right]^{1/2} \right) \quad (3.22a)$$

$$v_{slow} = \text{Re} \left(\frac{\omega}{\alpha_{tort}} \left[\frac{(1 - \beta_{por})^{s_2} k_c^2 + \beta_{por}^{s_2} k_g^2}{k_c^2 k_g^2} \right]^{1/2} \right) \quad (3.22b)$$

The phase velocity parameter s_2 in Eqs. (3.19) and (3.21) determines the functional form of the phase velocity as a function of porosity. Lee *et al.* introduced an empirical

anisotropy to this parameter and found that $s_2 = 0.5$ at parallel insonification and 1.7 at perpendicular insonification (Lee *et al.*, 2007a). These values for s_2 are used in the current study.

3.4.3 Biot and Modified Biot-Attenborough model predictions

The input parameter values for each model are listed in Table 3.1, and the resultant phase velocities at 500 kHz for the fast and slow waves as functions of porosity for both perpendicular and parallel insonification are shown in Fig. 3.1.

As indicated in Fig. 3.1, the angle-dependent Biot and Modified Biot models predict that when insonification is parallel to the trabecular orientation, corresponding to the superior-inferior (SI) direction in bovine leg bones, the velocities of the fast and slow waves remain distinct and moderately different over a wide range of porosities, including those within physiological ranges, and eventually converge toward the same value only at extremely high porosities. At a porosity of 0.85, Biot theory predicts that in the parallel orientation the difference in the velocities of the fast and slow waves is about 1180 m/s, whereas the Modified Biot model predicts a difference of approximately 1320 m/s. Experimentally, the velocities at parallel insonification were sufficiently different to permit Hosokawa and Otani to observe and measure the velocities of distinct fast and slow waves at porosities above 0.8 in samples approximately 9 mm thick (Hosokawa and Otani, 1998).

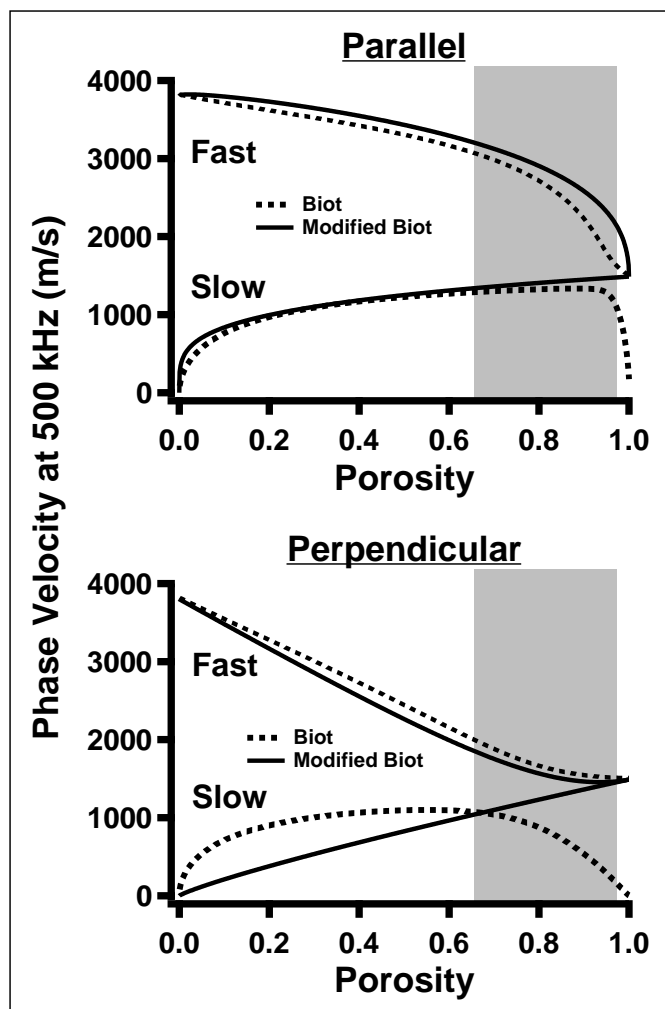


FIGURE 3.1: Predictions of Biot theory (dashed lines) and Modified Biot-Attenborough model (solid lines) for fast and slow wave velocities at 500 kHz as functions of porosity. The top panel shows predictions at parallel insonification, and the bottom panel shows predictions at perpendicular insonification. The shaded regions indicate the approximate range of physiological porosities for bovine and human cancellous bone measured by other investigators (Hosokawa and Otani, 1998; Lee *et al.*, 2003; Wear *et al.*, 2005).

The Biot and Modified Biot model predictions differ for the porosity-dependent behavior of the velocities when bone is insonified in the clinically relevant perpendicular direction. In that orientation, and at a porosity of 0.85, Biot theory predicts a velocity difference of 865 m/s, whereas the Modified Biot model predicts a difference of about 200 m/s. Experiments performed while insonifying in the perpendicular orientation have generally not resulted in the observation of distinct fast and slow waves. Investigations of the anisotropy of cancellous bone have demonstrated that the fast and slow waves become more and more overlapped as the angle of insonification proceeds from parallel to perpendicular (Hosokawa and Otani, 1998).

3.5 Simulated Wave Propagation in Bone

The propagation of ultrasound through bone was simulated by generating fast waves and slow waves independently using phase velocity and attenuation coefficient parameters, and then combined the two waves to form a simulated received signal. The input to the simulation consisted of a simulated broadband reference pulse with a center frequency of 550 kHz and a -6 dB bandwidth of approximately 250-850 kHz (see Fig. 3.2). An output waveform corresponding to ultrasonic wave propagation through bone was produced by applying linear transfer functions to the input

$$\text{Output}(\omega) = \text{Input}(\omega) [H_{fast}(\omega) + H_{slow}(\omega)] \quad (3.23)$$

where $\text{Output}(\omega)$ and $\text{Input}(\omega)$ are the complex frequency-domain representations of the input reference waveform and output mixed waveform. Wave propagation

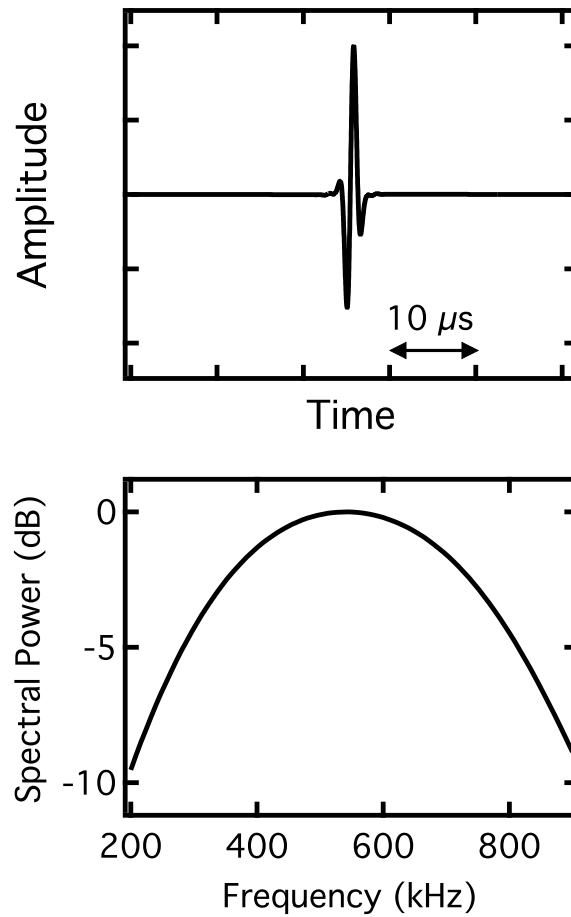


FIGURE 3.2: The time-domain representation of the artificially generated reference pulse used as input to the simulations is displayed in the upper panel, and the power spectrum of the pulse is shown in the lower panel.

through bone and bone-like materials is assumed to be linear, with speeds of sound and attenuation coefficients independent of amplitude. $H_{fast}(\omega)$ and $H_{slow}(\omega)$ are the transfer functions for the individual fast and slow waves given by

$$H_{fast}(\omega) = A_{fast} \exp[-\alpha_{fast}(\omega)l] \exp\left[i\omega \frac{l}{v_{fast}(\omega)}\right] \quad (3.24a)$$

$$H_{slow}(\omega) = A_{slow} \exp[-\alpha_{slow}(\omega)l] \exp\left[i\omega \frac{l}{v_{slow}(\omega)}\right] \quad (3.24b)$$

in which A_{fast} and A_{slow} are frequency-independent amplitude compensation factors that correspond to relative initial amplitudes of the fast and slow waves upon encountering the sample; l is the sample thickness; $\alpha_{fast}(\omega)$ and $\alpha_{slow}(\omega)$ are the attenuation coefficients given by

$$\alpha_{fast}(\omega) = \beta_{fast} \frac{\omega}{2\pi} \quad (3.25a)$$

$$\alpha_{slow}(\omega) = \beta_{slow} \frac{\omega}{2\pi} \quad (3.25b)$$

where β_{fast} and β_{slow} are the values for nBUA. The phase velocities $v_{fast}(\omega)$ and $v_{slow}(\omega)$ are given by

$$v_{fast}(\omega) = v_{fast}(\omega_0) + v_{fast}(\omega_0)^2 \frac{\beta_{fast}}{\pi^2} \ln\left(\frac{\omega}{\omega_0}\right) \quad (3.26a)$$

$$v_{slow}(\omega) = v_{slow}(\omega_0) + v_{slow}(\omega_0)^2 \frac{\beta_{slow}}{\pi^2} \ln\left(\frac{\omega}{\omega_0}\right) \quad (3.26b)$$

where ω_0 is a chosen reference frequency of interest. The linear-with-frequency functional form of the attenuation coefficients (Eq. (3.25)) is taken from the consensus of the published literature. The phase velocities (Eq. (3.26)) are obtained by applying the nearly-local form of the KK relations to the linear-with-frequency attenuation coefficients (Eq. (3.25)), under the assumption that this form of the KK relations is

valid for the fast and slow waves. These expressions for the phase velocities are valid for small dispersions.

In all simulations, the parameter l was set at 1 cm, a typical thickness of bone samples investigated *in vitro*. The value for the reference frequency $\frac{\omega_0}{2\pi}$ was set to 300 kHz, and $v_{slow}(\omega_0)$ was held constant at 1500 m/s, a velocity near that of sound in water. Based on measurements by Waters and Hoffmeister, the input values for β_{fast} and β_{slow} were set to 20 dB/cm/MHz and 6.9 dB/cm/MHz, respectively (Waters and Hoffmeister, 2005). Input values for $v_{fast}(\omega_0)$, A_{fast} , and A_{slow} were systematically varied. Based on the theoretical predictions displayed in Fig. 3.1, and the experimental observations of overlapping fast and slow wave modes, $v_{fast}(\omega_0)$ was varied between 1550 m/s and 2100 m/s, covering a wide range of velocities that result in the overlap of the fast and slow waves. When v_{fast} was varied, A_{fast} and A_{slow} were held constant at 0.3 and 0.7, respectively, so that the relative amplitudes of the fast and slow waves were comparable to those observed by other investigators (Hosokawa and Otani, 1998; Waters and Hoffmeister, 2005). Determining appropriate values for A_{fast} and A_{slow} is challenging, given the complexity involved in calculating transmission coefficients specific to individual fast and slow waves. Therefore, a second set of simulations was created in which $v_{fast}(\omega_0)$ was held constant at 1600 m/s and A_{fast} and A_{slow} were varied between 0 and 1 to determine the effects of those parameters on the resultant mixed waveform.

Phase velocities were calculated using a phase unwrapping algorithm previously shown to be valid for experimental data (Trousil *et al.*, 2001).

3.6 Results

The resulting attenuation coefficients and phase velocities when $v_{fast}(\omega_0)$ was varied between 1550 m/s and 2100 m/s are shown in Fig. 3.3. The relative contributions of the fast and slow waves, A_{fast} and A_{slow} , were held constant at 0.3 and 0.7, respectively. The left column of Fig. 3.3 was created with $v_{fast}(\omega_0)$ set at 1550 m/s, a velocity only 50 m/s faster than that of the slow wave. Under such conditions, a visual inspection of the RF signal reveals no explicit evidence of the presence of a second wave; furthermore, the attenuation coefficient and phase velocities do not exhibit suspicious behavior, despite interference taking place in the simulated ultrasonic field. However, as the difference in v_{fast} and v_{slow} becomes more pronounced, as in the remaining columns of Fig. 3.3, a negative dispersion becomes apparent, in spite of the fact that the frequency-dependent behavior of the attenuation coefficient could be approximated by a linear-with-frequency fit. When $v_{fast}(\omega_0) = 1600$ m/s, the magnitude of dispersion (difference in phase velocity) for a two-fold increase in frequency is approximately -4 m/s, based on a linear least squares fit over the bandwidth from 400-800 kHz. , as in the second column of Fig. 3.3. When $v_{fast}(\omega_0) = 1700$ m/s, the dispersion magnitude is approximately -15 m/s over the same bandwidth, with a local minimum in phase velocity appearing around 650 kHz. Additionally, the mixed waveform begins to show some evidence of interference under visual inspection. By the time the fast wave velocity reaches 2100 m/s (right panel), the fast and slow waves are sufficiently separated in time that the dispersion curve obtained by analyz-

ing the mixed waveform using a conventional phase spectroscopy algorithm has large fluctuations, with analogous behavior appearing in the attenuation coefficient.

Results for varying A_{fast} and A_{slow} are shown in Fig. 3.4. In the leftmost panel, the only contribution to the mixed waveform is the slow wave, and the resulting attenuation coefficient and phase velocity corresponding to this waveform are representative of the slow wave input parameters with positive dispersion. As the contribution of the fast wave increases (that is, A_{fast} becomes proportionally more important compared to A_{slow}), the behavior of the phase velocity changes, and begins to decrease with frequency (demonstrates a negative dispersion) over portions of the bandwidth. When $(A_{fast}, A_{slow}) = (0.3, 0.7)$, the magnitude of dispersion is -4 m/s over the 400-800 kHz bandwidth, but the attenuation coefficient can still be described as reasonably linear. The dispersion becomes approximately -11 m/s over the same bandwidth when $(A_{fast}, A_{slow}) = (0.4, 0.6)$, with the attenuation coefficient beginning to exhibit a modest degree of not-linear-with-frequency behavior. In each case, the individual fast and slow waves each exhibit a logarithmically-increasing (positive) dispersion and a linear-with-frequency attenuation coefficient. Furthermore, the time-domain RF data (top panels) do not show explicit evidence of two-wave interference upon visual inspection. The far right column of Fig. 3.4 shows the resultant mixed wave and its properties when $(A_{fast}, A_{slow}) = (1, 0)$, corresponding to only fast wave propagation. As expected, the phase velocity and attenuation coefficient of the mixed waveform return to mimicking those of the fast wave with positive dispersion.

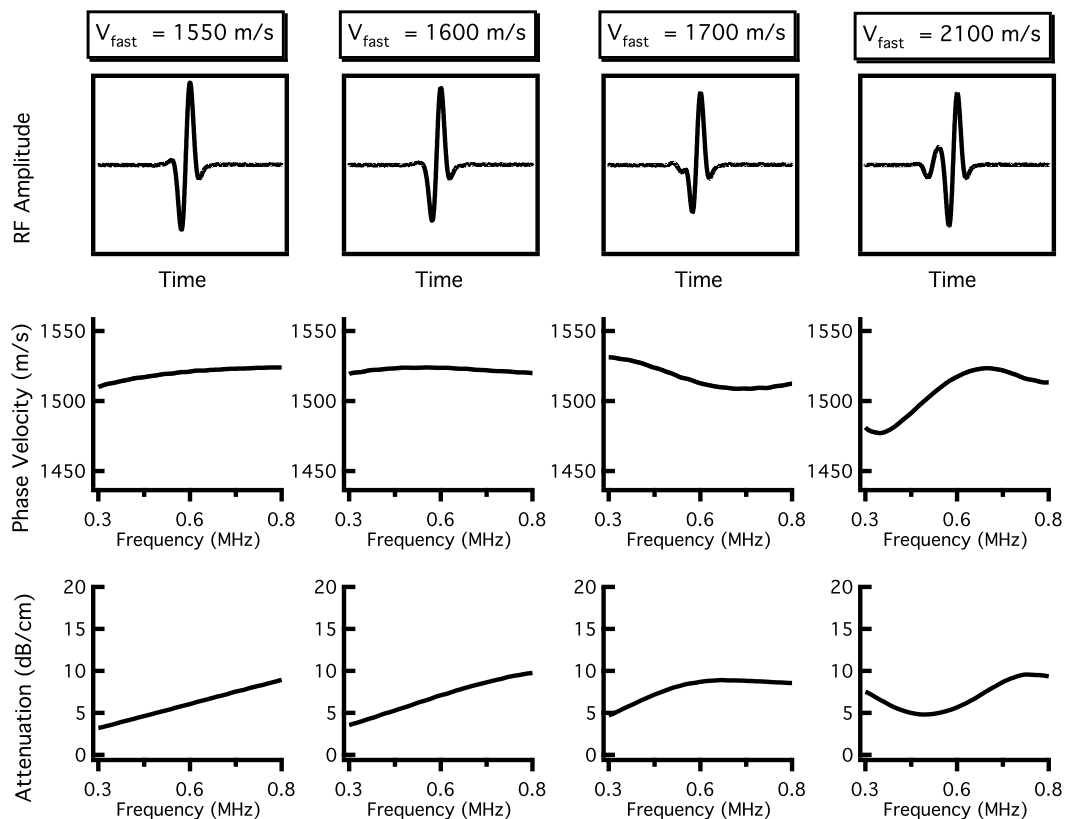


FIGURE 3.3: Results of independent fast and slow wave propagation when the velocity of the fast wave is varied. The velocity of the fast wave increases from the left column to the right column. The top panels display the resultant mixed RF waveforms, and the center and bottom panels show the corresponding dispersion curves and attenuation coefficients obtained when the mixed waveform is analyzed as if it contained only one wave. When v_{fast} is only 50 m/s greater than v_{slow} (far left panels), the mixed waveform exhibits positive dispersion and a nearly linear attenuation coefficient. As v_{fast} becomes increasingly greater than v_{slow} (middle panels), the dispersion becomes negative. When v_{fast} is significantly larger than v_{slow} (far right panels), the dispersion curve and attenuation coefficient have complicated frequency-dependent behavior.

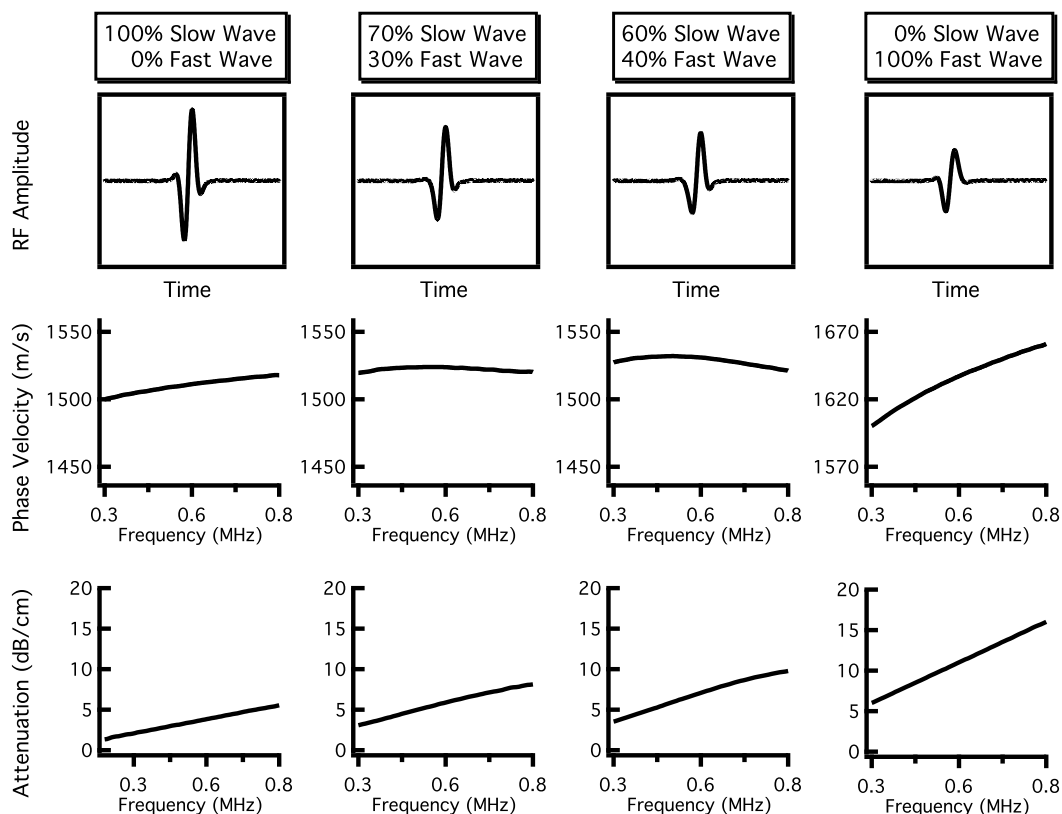


FIGURE 3.4: Results of independent fast and slow wave propagation when the relative contributions of the fast and slow wave are varied. The contribution of the fast wave increases from the left column to the right column. The top panels display the resultant mixed RF waveforms, and the center and bottom panels show the corresponding dispersion curves and attenuation coefficients obtained when the mixed waveform is analyzed as if it contained only one wave. The far left-hand panels display only slow wave propagation ($A_{fast} = 0, A_{slow} = 1$), resulting in a positive dispersion and a strictly linear attenuation coefficient. The far right-hand panels show only fast wave propagation ($A_{fast} = 1, A_{slow} = 0$), again corresponding to a positive dispersion and linear attenuation coefficient. The middle panels represent mixed waveforms (non-zero amplitudes for both fast and slow waves) that exhibit negative dispersions while maintaining an approximately linear attenuation coefficient.

3.7 Discussion

This study uses a linear systems approach, in conjunction with established experimental and theoretical evidence for multiple-wave propagation in cancellous bone, to generate a phenomenological model capable of producing simulated signals that exhibit negative dispersions similar to those observed in cancellous bone. The frequency-domain linear systems model has the advantage of simplicity and ease of computation, but this heuristic approach may not adequately account for all features of ultrasonic propagation through cancellous bone. Alternative approaches, including those that take advantage of finite difference time-domain techniques, may prove better for relating the fast and slow waves to the material properties of bone.

The parameter space for this model has been examined, specifically the relative amplitudes and velocities of the fast and slow waves, in the limited manner outlined in Figs. 3.3 and 3.4. The dispersions become more extreme, and more negative, as the fast and slow waves become closer in magnitude and more disparate in velocity. The detailed nature of the dispersion, however, depends on complicated interdependencies among all the parameters in the model, and a rigorous determination of what regions of the parameter space generate negative dispersion is beyond the scope of this preliminary study.

It has been assumed that the attenuation coefficients of cancellous bone rise linearly with frequency. This approximation appears to be adequate for frequencies in the hundreds of kilohertz range currently employed in many clinical devices, and is

consistent with the general consensus in the published literature. However, this model may not be rigorously valid for bandwidths extending far into the megahertz range, especially if longitudinal-to-longitudinal scattering becomes a significant contributor to the attenuation coefficient at higher frequencies.

The primary focus of this study is simulated propagation of multiple longitudinal waves through cancellous bone. Experimental confirmation of the results presented here would presumably involve analyzing data from bone samples that exhibit a negative dispersion when analyzed under the assumption that one wave was present, and recovering two waves when the data is analyzed in a way that permits distinguishing between fast and slow waves. However, differentiating the fast and slow waves can be difficult when they are strongly overlapped temporally. Our Laboratory has proposed a Bayesian approach for recovering the properties of each wave and has experimentally confirmed that negative dispersion can arise from two-mode propagation in a simple phantom (Marutyan *et al.*, 2007; Bauer *et al.*, 2008). A better understanding of the physical properties of cancellous bone that contribute to the attenuation and velocity properties of the fast and slow waves may also prove advantageous in predicting the degree of overlap of the two signals, which in turn could provide insight about the dispersion properties of a signal analyzed as if only one wave were present. To that end, Haiat *et al.* have investigated the effects of anisotropy and bone volume fraction on the degree of separation between the fast and slow waves (Haiat *et al.*, 2008).

3.8 Conclusion

Simulated ultrasonic wave propagation of fast and slow waves with phase velocities and attenuation coefficients, similar to those predicted and observed in bone, yielded resultant waveforms consisting of interfering waves that exhibited a decrease in phase velocity with frequency when analyzed conventionally under the assumption that only one wave was present. The underlying "true" ultrasonic characteristics of the fast and slow waves were obscured when analyzed in such a manner. Although the individual wave modes exhibited strictly linear-with-frequency attenuation coefficients and positive logarithmic-with-frequency phase velocities, conventional analysis of the mixed waveforms frequently resulted in complex frequency-dependencies of attenuation coefficient and dispersion. In fact, the two-independent mode model used in these simulations produced resultant mixed waveforms characterized by negative dispersion despite the fact that the individual fast and slow waves exhibit positive dispersions in accordance with the Kramers-Kronig relations for attenuation and dispersion. In some simulations, negative dispersion was produced without substantially changing the coarse visual characteristics of either the time-domain signal or the linear-with-frequency behavior of the attenuation coefficient. Although further study is required to determine the validity and role of independent mode simulations for characterizing bone, the interference of multiple waves appears to be a possible source for an apparent negative dispersion of the kind observed in cancellous bone. If the material and structural properties of cancellous bone give rise to multiple in-

terfering wave modes, recovering the ultrasonic characteristics of the individual wave modes, instead of those of the mixed waveform, could provide more robust ultrasonic determinations of bone quality.

Acknowledgments

This work was supported in part by NSF Grant No. CBET-0717830 Scholar in Residence at the FDA and by NIH Grant No. R37 HL40302.

Bibliography

- Apostolopoulos, K. N. and Deligianni, D. D. (2008). “Influence of microarchitecture alterations on ultrasonic backscattering in an experimental simulation of bovine cancellous bone aging.”, *J Acoust Soc Am* **123**, 1179–1187.
- Bauer, A. Q., Marutyan, K. R., Holland, M. R., and Miller, J. G. (2007). “Is the kramers-kronig relationship between ultrasonic attenuation and dispersion maintained in the presence of apparent losses due to phase cancellation?”, *J Acoust Soc Am* **122**, 222–228.
- Bauer, A. Q., Marutyan, K. R., Holland, M. R., and Miller, J. G. (2008). “Negative dispersion in bone: the role of interference in measurements of the apparent phase velocity of two temporally overlapping signals.”, *J Acoust Soc Am* **123**, 2407–2414.
- Biot, M. A. (1956a). “Theory of propagation of elastic waves in a fluid-saturated porous solid. I. Low-frequency range”, *J Acoust Soc Am* **28**, 168–178.
- Biot, M. A. (1956b). “Theory of propagation of elastic waves in a fluid-saturated porous solid. II. Higher frequency range”, *J Acoust Soc Am* **28**, 179–191.
- Chakraborty, A. (2008). “Prediction of negative dispersion by a nonlocal poroelastic theory.”, *J Acoust Soc Am* **123**, 56–67.
- Droin, P., Berger, G., and Laugier, P. (1998). “Velocity dispersion of acoustic waves in cancellous bone”, *IEEE Trans Ultrason Ferroelectr Freq Control* **45**, 581–592.
- Fellah, Z. E. A., Chapelon, J. Y., Berger, S., Lauriks, W., and Depollier, C. (2004). “Ultrasonic wave propagation in human cancellous bone: application of biot theory.”, *J Acoust Soc Am* **116**, 61–73.
- Haiat, G., Padilla, F., Peyrin, F., and Laugier, P. (2008). “Fast wave ultrasonic propagation in trabecular bone: numerical study of the influence of porosity and structural anisotropy.”, *J Acoust Soc Am* **123**, 1694–1705.
- Haire, T. and Langton, C. (1999). “Biot theory: A review of its application to ultrasound propagation through cancellous bone”, *Bone* **24**, 291–295.
- Hoffmeister, B. K., Whitten, S. A., and Rho, J. Y. (2000). “Low-megahertz ultrasonic properties of bovine cancellous bone.”, *Bone* **26**, 635–642.
- Hosokawa, A. and Otani, T. (1997). “Ultrasonic wave propagation in bovine cancellous bone.”, *J Acoust Soc Am* **101**, 558–562.
- Hosokawa, A. and Otani, T. (1998). “Acoustic anisotropy in bovine cancellous bone.”, *J Acoust Soc Am* **103**, 2718–2722.

- Hughes, E. R., Leighton, T. G., Petley, G. W., and White, P. R. (1999). “Ultrasonic propagation in cancellous bone: a new stratified model.”, *Ultrasound Med Biol* **25**, 811–821.
- Hughes, E. R., Leighton, T. G., White, P. R., and Petley, G. W. (2007). “Investigation of an anisotropic tortuosity in a biot model of ultrasonic propagation in cancellous bone.”, *J Acoust Soc Am* **121**, 568–574.
- Johnson, D. L., Koplik, J., and Dashen, R. (1987). “Theory of dynamic permeability and tortuosity in fluid-saturated porous media”, *J Fluid Mech* **176**, 379–402.
- Lee, K. I., Hughes, E. R., Humphrey, V. F., Leighton, T. G., and Choi, M. J. (2007a). “Empirical angle-dependent biot and mba models for acoustic anisotropy in cancellous bone.”, *Phys Med Biol* **52**, 59–73.
- Lee, K. I., Humphrey, V. F., Leighton, T. G., and Yoon, S. W. (2007b). “Predictions of the modified biot-attenborough model for the dependence of phase velocity on porosity in cancellous bone.”, *Ultrasonics* **46**, 323–330.
- Lee, K. I., Roh, H.-S., and Yoon, S. W. (2003). “Acoustic wave propagation in bovine cancellous bone: application of the modified biot-attenborough model.”, *J Acoust Soc Am* **114**, 2284–2293.
- Lin, W., Qin, Y. X., and Rubin, C. (2001). “Ultrasonic wave propagation in trabecular bone predicted by the stratified model.”, *Ann Biomed Eng* **29**, 781–790.
- Marutyan, K. R., Bretthorst, G. L., and Miller, J. G. (2007). “Bayesian estimation of the underlying bone properties from mixed fast and slow mode ultrasonic signals.”, *J Acoust Soc Am* **121**, EL8–15.
- Marutyan, K. R., Holland, M. R., and Miller, J. G. (2006). “Anomalous negative dispersion in bone can result from the interference of fast and slow waves.”, *J Acoust Soc Am* **120**, EL55–61.
- Mobley, J., Waters, K. R., and Miller, J. G. (2005). “Causal determination of acoustic group velocity and frequency derivative of attenuation with finite-bandwidth kramers-kronig relations.”, *Phys Rev E Stat Nonlin Soft Matter Phys* **72**, 016604.
- Nicholson, P. H., Lowet, G., Langton, C. M., Dequeker, J., and Van der Perre, G. (1996). “A comparison of time-domain and frequency-domain approaches to ultrasonic velocity measurement in trabecular bone.”, *Phys Med Biol* **41**, 2421–2435.
- O’Donnell, M., Jaynes, E. T., and Miller, J. G. (1981). “Kramers-kronig relationship between ultrasonic attenuation and phase velocity”, *J Acoust Soc Am* **69**, 696–701.
- Padilla, F. and Laugier, P. (2000). “Phase and group velocities of fast and slow compressional waves in trabecular bone.”, *J Acoust Soc Am* **108**, 1949–1952.

- Plona, T. J., Winkler, K. W., and Schoenberg, M. (1987). “Acoustic waves in alternating fluid/solid layers”, *J Acoust Soc Am* **81**, 1227–1234.
- Roh, H.-S. and Yoon, S. W. (2004). “Acoustic diagnosis for porous medium with circular cylindrical pores.”, *J Acoust Soc Am* **115**, 1114–1124.
- Sebaa, N., Fella, Z. E. A., Fella, M., Ogam, E., Wirgin, A., Mitri, F. G., Depollier, C., and Lauriks, W. (2006). “Ultrasonic characterization of human cancellous bone using the biot theory: inverse problem.”, *J Acoust Soc Am* **120**, 1816–1824.
- Trousil, R. L., Waters, K. R., and Miller, J. G. (2001). “Experimental validation of the use of kramers-kronig relations to eliminate the phase sheet ambiguity in broadband phase spectroscopy.”, *J Acoust Soc Am* **109**, 2236–2244.
- Waters, K., Hughes, M., Mobley, J., Brandenburger, G., and Miller, J. (2000). “On the applicability of kramers-kronig relations for ultrasonic attenuation obeying a frequency power law”, *J Acoust Soc Am* **108**, 556–563.
- Waters, K. R. and Hoffmeister, B. K. (2005). “Kramers-Kronig analysis of attenuation and dispersion in trabecular bone.”, *J Acoust Soc Am* **118**, 3912–3920.
- Waters, K. R., Mobley, J., and Miller, J. G. (2005). “Causality-imposed (kramers-kronig) relationships between attenuation and dispersion.”, *IEEE Trans Ultrason Ferroelectr Freq Control* **52**, 822–833.
- Wear, K. A. (2000). “Measurements of phase velocity and group velocity in human calcaneus”, *Ultrasound Med Biol* **26**, 641–646.
- Wear, K. A. (2001). “A stratified model to predict dispersion in trabecular bone.”, *IEEE Trans Ultrason Ferroelectr Freq Control* **48**, 1079–1083.
- Wear, K. A. (2007). “Group velocity, phase velocity, and dispersion in human calcaneus in vivo.”, *J Acoust Soc Am* **121**, 2431–2437.
- Wear, K. A., Laib, A., Stuber, A. P., and Reynolds, J. C. (2005). “Comparison of measurements of phase velocity in human calcaneus to Biot theory.”, *J Acoust Soc Am* **117**, 3319–3324.
- Williams, J. L. (1992). “Ultrasonic wave propagation in cancellous and cortical bone: prediction of some experimental results by Biot’s theory.”, *J Acoust Soc Am* **91**, 1106–1112.

CHAPTER 4

BAYESIAN PROBABILITY THEORY AND MARKOV CHAIN MONTE CARLO

4.1 Preface

This Chapter provides background information on Bayesian probability theory and the use of Markov chain Monte Carlo (MCMC) in Bayesian applications. The particular algorithms discussed are simulated annealing and nested sampling.

4.2 Abstract

Bayesian probability theory is a powerful inference tool with extensive applications in the natural sciences. Many applications of Bayesian probability, including the parameter estimation problems addressed in later Chapters of this Dissertation, require advanced computational algorithms to approximate the Bayesian posterior probabilities. In this Chapter, a brief historical context for Bayesian probability theory is provided, followed by a summary of Bayesian calculations used in later Chapters. The Markov chain Monte Carlo methods, used to carry out these calculations, simulated annealing and nested sampling, are then discussed.

4.3 Bayesian probability theory

4.3.1 Historical perspective

Bayesian probability theory is an extension of logic that permits reasoning when the available information is not sufficient to determine facts with certainty. Its validity as an inductive inference tool makes it ideal for use in the natural sciences, where knowledge is always incomplete. The word “Bayesian” is derived from the name of Rev. Thomas Bayes, whose ideas on probability were published posthumously in 1763 (Bayes, 1763). Laplace independently rediscovered and formalized the approach, applying it to problems in celestial mechanics (Laplace, 1812, 1814). However, the formalism fell out of favor as the frequentist interpretation of probability dominated

statistical inference. Bayesian ideas remained popular among a minority of investigators in the twentieth century, notably Jeffreys (1939), Cox (1946), and Jaynes (1986, 2003).

In the Bayesian interpretation, probabilities represent states of knowledge; they are “degrees of belief” conditional on the information at hand (Jaynes, 2003; Sivia, 2006; Gregory, 2005; Stauffer, 2008). Notationally, probabilities are written in the form $P(X|I)$, which should be understood to mean “the probability for a proposition X given I ”, where I is available background information. To emphasize that all probabilities in the Bayesian approach are conditional, the probabilities are always dependent on I .

The Bayesian interpretation of probability has historically been a minority position within the probability and statistics community. A common perception was that the definition of probability as a degree of belief was too subjective; furthermore, Bayesian analysis was difficult from a practical perspective because of the intense computational power required to solve complex problems. However, in recent years, advantages of Bayesian probability theory over alternative interpretations of probability have been highlighted (Jaynes, 2003; Stauffer, 2008). In addition, the development of fast computing technologies and advanced computational algorithms, especially Markov chain Monte Carlo (MCMC), has made Bayesian analysis much more efficient and convenient, leading to increased interest in Bayesian probability (Stauffer, 2008).

4.3.2 Bayes' Theorem

Cox found that a logical and consistent system of reasoning must obey two rules (Cox, 1946). The first is the *sum rule*,

$$P(X|I) + P(\bar{X}|I) = 1, \quad (4.1)$$

where \bar{X} is the probability that X is not true. The second is the *product rule*,

$$P(XY|I) = P(X|YI)P(Y|I) \quad (4.2)$$

where X and Y are separate propositions. The product rule can be used to derive *Bayes' Theorem* (Bayes, 1763; Jaynes, 2003),

$$P(X|YI) = \frac{P(Y|XI)P(X|I)}{P(Y|I)}. \quad (4.3)$$

The term $P(X|YI)$ is known as the *posterior probability* for X given Y and I , and $P(Y|XI)$ called the *likelihood*. $P(X|I)$ is the *prior probability* for X , which is conditional only on the background information (i.e., what is known about X prior to obtaining information about Y). The term in the denominator of Eq. (4.3) has been referred to by several different names. Some examples are *marginal likelihood*, *prior predictive*, and *evidence*.

The sum rule and product rules can be used to derive a more generalized expression of Eq. (4.1),

$$P(X|I) = P(XY|I) + P(X\bar{Y}|I), \quad (4.4)$$

where an expression for $P(X|I)$ has been obtained by *marginalizing* over possible values for Y . If there exists a set of N propositions $\{Y_1, Y_2, \dots, Y_N\}$, Eq. (4.4) can be

recast as

$$P(X|I) = \sum_{k=1}^N P(XY_k|I) \quad (4.5)$$

provided that the set of Y_k form a mutually exclusive and exhaustive set of possibilities.

It is useful to consider further generalization to the continuum limit ($N \rightarrow \infty$), as when (for example) the Y_k constitute values of some continuous parameter. Eq. (4.5) becomes

$$P(X|I) = \int_{-\infty}^{\infty} P(XY|I)dY. \quad (4.6)$$

It must be noted that in Eq.(4.6), the integrand $P(XY|I)$ is a probability *density* rather than a probability. Eq. (4.6) is especially useful for eliminating nuisance parameters in many calculations.

4.4 Bayesian calculations

Common tasks in probability theory are estimation of the values of unknown parameters (parameter estimation) and determining the best model for a data set from a number of candidate models (model selection). Bayesian applications addressed in this Dissertation pertain to parameter estimation in ultrasonic measurements on cancellous bone and heart tissue, and this section describes how these parameters are estimated. The calculations parallel those reported by Bretthorst *et al.* (2005b,a).

In parameter estimation problems, the model and its corresponding parameters are known. Suppose that a generic model for an acquired data set of N data points

is given by

$$D_j = M_j(\Theta) + n_j, \quad (4.7)$$

where D_j is the j th point in the data vector D , $M_j(\Theta)$ is the corresponding point in the vector M that models the data, Θ is the parameter vector to be estimated, and n_j is the j th point in the residual vector n (the difference between the data and the model), often referred to as noise. The dimensionality of the parameter vector Θ can be arbitrarily large. For the purpose of illustration, suppose there are three parameters in M , such that Θ is three-dimensional; that is, $\Theta \equiv \{\theta_1, \theta_2, \theta_3\}$. The goal is to estimate the values of $\{\theta_1, \theta_2, \theta_3\}$ given the data. Symbolically, then, the task is to determine the *marginal* posterior probabilities $P(\theta_1|DI)$, $P(\theta_2|DI)$, and $P(\theta_3|DI)$.

The calculation begins by considering the *joint* posterior probability for all the parameters together, $P(\Theta|DI) \equiv P(\theta_1\theta_2\theta_3|DI)$, and applying Bayes' Theorem,

$$P(\Theta|DI) = \frac{P(D|\Theta)P(\Theta|I)}{P(D|I)}. \quad (4.8)$$

In parameter estimation problems, the term $P(D|I)$ can be considered a normalization constant and can be ignored provided we normalize these probabilities at the end of the calculations. Thus, Eq. (4.8) becomes

$$P(\Theta|DI) \propto P(D|\Theta)P(\Theta|I). \quad (4.9)$$

The joint prior, $P(\Theta|I)$, can be written as the product of priors for the individual parameters,

$$P(\Theta|I) = P(\theta_1|I)P(\theta_2|I)P(\theta_3|I), \quad (4.10)$$

under the assumption that the parameters are logically independent. Logical independence means that knowledge about the value of θ_1 has no influence on knowledge about the value of θ_2 or θ_3 , etc. The factors on the right-hand side of Eq. (4.10) can be assigned based on prior information about the individual parameters. If the prior information is vague, common choices for these priors are flat (uniform) functions or broad Gaussian functions.

The remaining term in Eq. (4.9) is the likelihood, or the direct probability for the data given the parameters, $P(D|\Theta I)$. Assignment of this probability requires reintroducing the characteristics of the residuals, the n_j in Eq. (4.7). The symbol n does not appear in $P(D|\Theta I)$ because this term is a marginal probability; information about the residuals has been removed by marginalization. The quantities of interest are the set of noise parameters n and the standard deviation of the prior probability for n , denoted by σ . We can reintroduce these quantities by writing

$$P(D|\Theta I) = \iint d\sigma dn P(Dn\sigma|\Theta I). \quad (4.11)$$

Factoring the integrand of Eq. (4.11) using the sum and product rules of probability theory (Eqs. (4.1) and (4.2)) gives

$$P(D|\Theta I) = \iint d\sigma dn P(\sigma|I)P(n|\sigma)P(D|\sigma n\Theta I). \quad (4.12)$$

The terms $P(\sigma|I)$ and $P(n|\sigma)$ are the prior probability for the standard deviation of the noise and the probability for the noise values given the standard deviation, respectively. The remaining term, $P(D|\sigma n\Theta I)$, is the direct probability for the data given the parameters, standard deviation, and n . This direct probability must be a

delta function, because the sum of n and the model at any given data point either equals the data (probability = 1) or does not (probability = 0). This situation is expressed by

$$P(D|\sigma n \Theta I) = \prod_j \delta [(D_j - M_j(\Theta)) - n_j]. \quad (4.13)$$

The prior probability $P(n|\sigma)$ can now be assigned. The principle of maximum entropy can be used to assign this prior probability as a zero-mean Gaussian function of standard deviation σ ,

$$P(n|\sigma) = (2\pi\sigma^2)^{-\frac{N}{2}} \exp \left[-\sum_j \frac{n_j^2}{2\sigma^2} \right]. \quad (4.14)$$

The prior probability for σ is assigned as a Jeffreys prior (Jeffreys, 1939),

$$P(\sigma|I) \propto \frac{1}{\sigma} \quad (4.15)$$

In general, care must be taken when using a Jeffreys prior because it is not normalizable and hence not a proper probability distribution. Its use in the problems described in this Dissertation is justified because the bounded prior probabilities used for the parameters Θ , as well as the digital limit of the computing platform, provide effective bounds that prevent the calculation from approaching an infinity provided that there is noise in the data, a realistic expectation in any experimental setting.

Substituting Eqs. (4.13-4.15) into Eq. (4.12),

$$P(D|\Theta I) \propto \iint d\sigma dn \left(\frac{1}{\sigma} \right) (2\pi\sigma^2)^{-\frac{N}{2}} \exp \left[-\sum_j \frac{n_j^2}{2\sigma^2} \right] \times \prod_j \delta [(D_j - M_j(\Theta)) - n_j]. \quad (4.16)$$

After simplification and evaluation of the integral over n ,

$$P(D|\Theta I) \propto \int d\sigma \sigma^{-N-1} \exp \left[-\frac{\sum_j (D_j - M_j(\Theta))^2}{2\sigma^2} \right]. \quad (4.17)$$

The integral over σ in Eq. (4.17) can be transformed into a Gamma function integral and evaluated, yielding

$$P(D|\Theta I) \propto \left(\frac{\sum_j (D - M(\Theta))^2}{2} \right)^{-\frac{N}{2}}, \quad (4.18)$$

an expression in the form of Student's t -distribution.

Substitution of Eqs. (4.10) and (4.18) into Eq. (4.9) yields

$$P(\Theta|DI) \propto \left(\frac{\sum_j (D - M(\Theta))^2}{2} \right)^{-\frac{N}{2}} P(\theta_1|I)P(\theta_2|I)P(\theta_3|I), \quad (4.19)$$

the final expression for the joint posterior probability for the parameters.

The marginal posterior probability densities for each parameter can be obtained from the joint posterior probability by using the marginalization equation to remove the parameters except the one of interest. For example, the marginal posterior probability for θ_1 is computed by integrating Eq. (4.19) over θ_2 and θ_3 ,

$$P(\theta_1|DI) = \iint d\theta_2 d\theta_3 P(\Theta|DI). \quad (4.20)$$

Note that for a model with m parameters, an $(m - 1)$ -dimensional integral must be performed m times to obtain marginal posterior probabilities for all parameters.

4.5 Markov chain Monte Carlo

If the model $M(\Theta)$ is complex or high-dimensional, an analytic solution to expressions like that of Eq. (4.20) may be difficult or impossible to achieve. Markov

chain Monte Carlo methods are a class of algorithms designed to sample from the posterior probabilities, thus eliminating the need to compute analytical solutions to the complex integrals by obtaining an approximate numerical solution (Gelfand and Smith, 1990; Tierney, 1994).

4.5.1 Markov chains

A *Markov chain* is a discrete stochastic process in which samples are drawn from a state space, and the i th state depends only on the $(i - 1)$ th state. In Bayesian applications, a Markov chain is initialized at some arbitrary location in the parameter space, usually by sampling from the prior probability density. By undergoing successive transitions within the parameter space, the chain eventually converges to the desired target posterior probability density. The samples generated by the locations visited by the chain can be analyzed and/or parameterized to form an empirical picture of the posterior probability (Bretthorst *et al.*, 2005b; Sivia, 2006).

To ensure proper convergence, the Markov chain must satisfy certain properties (Gilks *et al.*, 1996; Madras, 2002; Behrens, 2000; Stauffer, 2008). First, the chain must be *irreducible*, meaning that there must be a non-zero probability of reaching each point in the parameter space from any other location in the space. The second requirement is that the chain must be *aperiodic*. It must not oscillate between some set of states, or repeat some fixed sequence of states visited, even if that sequence includes every state in the space. The last required property is that the Markov chain must be *positive recurrent*, meaning that the expected time for the chain to return

to a visited state is finite. A Markov chain satisfying all three of these properties is said to be *ergodic* (Gregory, 2005; Stauffer, 2008).

4.5.2 The Metropolis-Hastings algorithm

The Monte Carlo method was envisioned by Stanislaw Ulam in 1946 while he was contemplating the chances of winning a game of Canfield solitaire (Eckhardt, 1987). The name “Monte Carlo” was suggested by Ulam’s colleague Nicholas Metropolis, who was inspired by an uncle of Ulam’s who had a habit of borrowing money because he “just had to go to Monte Carlo” (Metropolis, 1987). It was published by Metropolis and Ulam (1949) and shortly thereafter by Metropolis *et al.* (1953), who were interested in performing calculations related to neutron diffusion in fissionable material (Metropolis, 1987). Rather than calculate probabilities for all possible particle configurations, Metropolis *et al.* devised a method to simulate particle movement subject to a minimum energy criterion, allowing the system of particles to stochastically “walk” to highly probable states. Hastings (1970) subsequently generalized this approach, and it became known as the Metropolis-Hastings algorithm. The Metropolis-Hastings algorithm is now a widely-used technique for sampling from probability densities. Given a posterior density $P(x|DI)$ for a parameter x , the algorithm is as follows.

1. Initialize a starting point x_0 .
2. At the i th iteration, given x_{i-1} ,
 - (a) Determine a candidate new location x'_i from a proposal distribution $q(x'_i|x_{i-1})$. The support of $q(x'_i|x_{i-1})$ must include the support of $P(x|DI)$.

(b) Calculate the acceptance ratio

$$r = \frac{P(x'_i|DI)q(x'_i|x_{i-1})}{P(x_{i-1}|DI)q(x_{i-1}|x'_i)}. \quad (4.21)$$

(c) Sample a real number U in the interval $(0,1)$ from a uniform density.

(d) Set

$$x_i = \begin{cases} x'_i & \text{if } U \leq r \\ x_{i-1} & \text{otherwise} \end{cases}. \quad (4.22)$$

3. Increment i and move on to the next iteration beginning at step 2.

The proposal distribution $q(x'_i|x_{i-1})$ can have almost any form, but a popular choice is a multivariate Gaussian centered on x_{i-1} . The width of the Gaussian can be varied according to the proportion of accepted proposed moves. If too many proposals are accepted, the width of the proposal distribution is too small; if the opposite is true, the width is too large. For a parameter space of three or more dimensions, a theoretically optimal acceptance rate is 0.234 (Roberts *et al.*, 1997).

The Metropolis-Hastings algorithm works by proposing a move within some neighborhood of the current location ($x_{i-1} \rightarrow x'_i$). The move is always accepted ($x_i = x'_i$) if the probability at the new location is higher than the probability at the current one. However, even if the proposed location is “downhill” in probability from the current location, the move is still accepted with probability $\frac{\text{prob}(\text{new location})}{\text{prob}(\text{old location})}$. In this manner, some downhill moves are permitted, although “small” downhill moves are more favorable than “large” ones. The sequence of x_i in the Metropolis-Hastings algorithm forms a Markov chain. A schematic of an example Markov chain trajectory in a hypothetical two-dimensional parameter space is shown in Fig. 4.1.

4.5.3 Simulated annealing

One could, of course, initialize a single Markov chain and allow it to explore the parameter space using the Metropolis-Hastings method until it converges to the target distribution. However, this approach can be problematic if the posterior density is multimodal. In such cases, the chain can become stuck in a local maximum and fail to explore the other modes. Furthermore, it can be difficult to determine if and when the chain has converged to the posterior density.

One solution to these concerns is simulated annealing, introduced by Kirkpatrick *et al.* (1983). Annealing in metallurgy and materials science is a process in which a material is heated above its melting temperature and then slowly cooled, allowing the constituent atoms to arrive at a low-energy configuration as the material solidifies. If the material is cooled too quickly, the atoms become fixed in a high-energy state. Simulated annealing works analogously in a computational context. To help prevent the Markov chains from becoming stuck in a local maximum of the target distribution, the chains are allowed to explore a series of intermediate probability densities that smoothly transition from the joint prior to the target joint posterior probability. In parameter estimation problems, the task is accomplished by introducing an annealing parameter $\beta \in [0, 1]$ to Bayes' Theorem (Eq. (4.9)),

$$P(\Theta|DI) \propto [P(D|\Theta)]^\beta P(\Theta|I). \quad (4.23)$$

The annealing parameter acts as the inverse of temperature. At the start of the calculation, β is initialized at zero (high temperature) and increases to 1 (low temperature)

in a series of steps as the simulation progresses. The manner and rate at which β moves from 0 to 1 is known as the *annealing schedule*, which can be expressed as the series $\{\beta_0, \beta_1, \dots, \beta_j\}$ after j steps. The annealing schedule can be adjusted to fit the needs of the particular problem. A long schedule costs computation time, but a schedule that is too short increases the risk of the chain producing a local maximum. When simulated annealing is applied to problems described in this Dissertation, the annealing schedule is designed so that β increases linearly from 0 to 1 in 101 or 201 iterations.

After j iterations, the series of intermediate target distributions can be written $\{P_{\beta_0}, P_{\beta_1}, \dots, P_{\beta_j}\}$, where P_{β_j} is shorthand for $[P(D|\Theta I)]^\beta P(\Theta|I)$ at the j th iteration. Each time β is incremented, the Markov chain is allowed to sample from the intermediate distribution for a sufficient number of Metropolis-Hastings steps that the samples reflect P_{β_j} . Using this approach, the samples reflect the prior at the start of the calculation ($\beta = 0$) and transition smoothly to reflect the target posterior at the end of the calculation ($\beta = 1$). An illustration of how changing β affects the target distribution is shown in a one-dimensional example in Fig. 4.2.

An advantage of simulated annealing is that it can naturally be parallelized. Multiple independent Markov chains can be run simultaneously and in parallel using modern computing technology. The use of multiple chains permits more efficient exploration of the parameter space and ensures that the samples drawn from the collection of chains are more independent than those originating from a single chain. Furthermore, it provides another measure of protection against exploration of a local

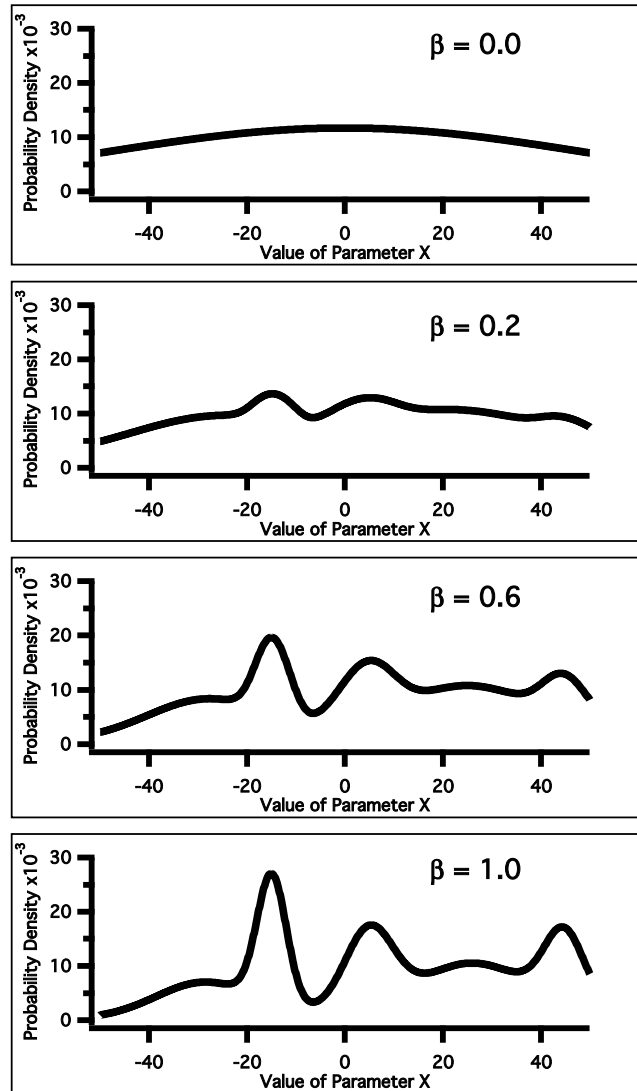


FIGURE 4.2: One-dimensional illustration of the effect of the annealing parameter β on a hypothetical target distribution of a parameter X . When $\beta = 0$, the target distribution is a smooth Gaussian prior. As β increases, the target distribution begins to resemble the multimodal posterior, and eventually becomes the posterior itself when $\beta = 1$. Allowing the Markov chains to converge to each intermediate distribution decreases the chance of one or more chains becoming stuck on a local maximum.

maximum because low-probability chains can be “killed” and replaced by higher-probability chains. When this method is employed, the chains are sorted by probability at each β step, and some number of the lowest probability chains are eliminated. A corresponding number of surviving chains are selected at random to be duplicated, thus replacing the killed chains with chains more likely to find the global maximum in probability. When the calculation resumes, the duplicated chains wander apart stochastically by the Metropolis-Hastings algorithm, and can eventually be considered independent.

Still another advantage of multiple chains is the enhanced ability to better evaluate convergence of the Markov chains. There is currently no known test that guarantees convergence. However, the trajectories of many Markov chains with the same target distribution can be used to gather evidence of whether they have collectively *not* converged. If all chains are found to be systematically sampling from approximately the same neighborhood in the parameter space at the end of the calculation, with normally distributed variations in the sampled probabilities, it may be inferred that each chain has converged to the target. If the trajectories of some chains differ substantially from the others, or there are systematic increases in the probabilities of the samples, then the chains have not yet converged. A plot of the trajectories of several Markov chains obtained in a calculation described in Chapter 5 is shown in Fig. 4.3. The samples obtained from the chains in Fig. 4.3 are well-mixed, indicating an absence of evidence against convergence (but not proof of convergence).

The simulated annealing algorithm can be summarized as follows.

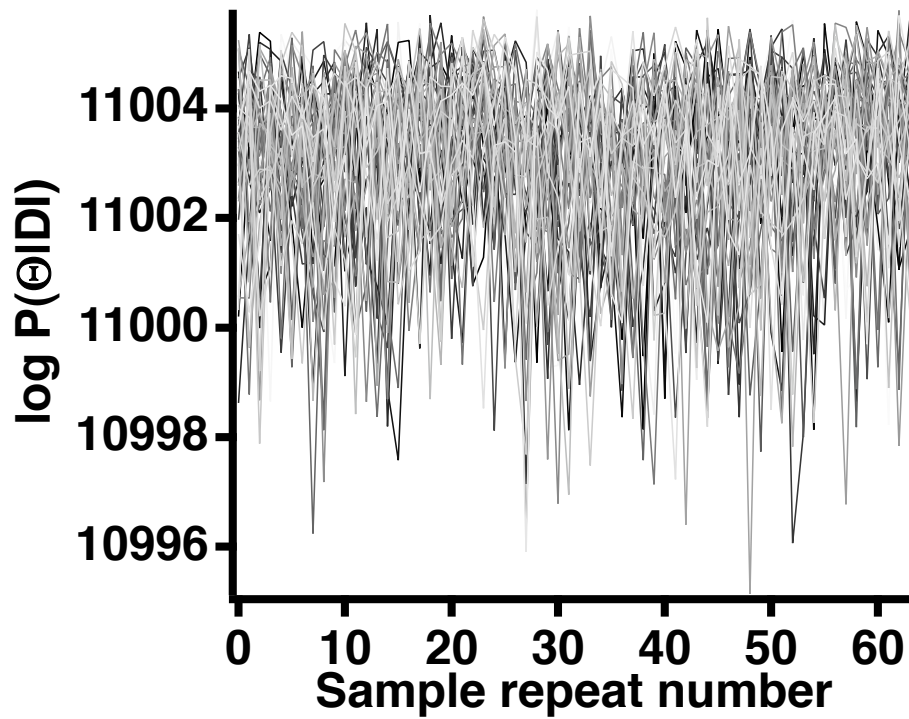


FIGURE 4.3: In this typical example from results of a simulation described in Chapter 5, 64 Markov chains each drew 64 samples from the joint posterior probability for a group of parameters Θ . The logarithm of the posterior probability for each of the 64 chains is plotted against the sample repeat number. The trajectories of the chains are well-mixed, suggesting an absence of evidence against convergence.

1. Initialize the Markov chains within the parameter space by sampling from the prior probability densities.
2. While the annealing parameter is less than 1,
 - (a) Increase the annealing parameter according to the schedule.
 - (b) Kill and replace low-probability Markov chains.
 - (c) Allow the Markov chains to explore the parameter space using the Metropolis-Hastings algorithm.
3. While there are fewer samples of the posterior than the desired number,
 - (a) Save the current samples stored in the active Markov chains
 - (b) Allow the Markov chains to explore the parameter space using the Metropolis-Hastings algorithm.

An application of simulated annealing to Bayesian parameter estimation in ultrasonic wave propagation in cancellous bone is described in Chapter 5

4.5.4 Nested sampling

Nested sampling, introduced by Skilling (2006), is an alternative technique for Bayesian computation. Skilling's motivation is to directly compute $P(D|I)$, the term in the denominator of Bayes' Theorem in Eq. 4.3. This term is known as the evidence, represented by Z . The evidence can be written

$$Z = \int P(D|\Theta I)P(\Theta|I)d\Theta, \quad (4.24)$$

where $P(D|\Theta I)$ is the likelihood and $P(\Theta|I)d\Theta$ is the prior mass element for data D and parameters Θ . Eq. (4.24) can be rewritten in the one-dimensional form

$$Z = \int L(X)dX, \quad (4.25)$$

where $L = P(D|\Theta I)$ and $dX = P(\Theta|I)d\Theta$. Nested sampling obtains an approximation to Eq. (4.25) by systematically tabulating the integrand, starting with the lowest contribution to Z and working upwards in likelihood. The process may be conceptualized by imagining a series of nested probability contours within a parameter space. The outermost contour is sampled first, and its contribution to the evidence is computed and added to the total. The next innermost contour then is sampled, then the next, and so on, working upwards in probability until the bulk of the joint posterior density has been found. Numerically, this iterative approach begins by initializing N samples from the prior. The sample with the lowest probability is identified, and its likelihood is temporarily stored as the *likelihood constraint* for that iteration, denoted L^* . The sample is then stored, and its contribution to the total evidence Z is calculated. The simplest way of computing this quantity at iteration k is

$$\Delta Z_k = L_k^*(X_{k-1} - X_k), \quad (4.26)$$

where ΔZ_k is the new component of Z and X_k is given by

$$X_k = \exp\left(-\frac{k}{N}\right). \quad (4.27)$$

Eq. (4.27) is obtained by calculating the expectation value for the amount of prior mass enclosed by probability contours defined by the lowest-probability samples in consecutive iterations. Eq. (4.26) shows that the integral of Eq. (4.25) is evaluated by adding a series of rectangles in the space defined by L and X .

After adding the new component of Z to the running total, the sample with likelihood L^* is eliminated, and one of the surviving $N - 1$ chains is duplicated to replace

it. The new, replacement sample is allowed to move within the parameter space via Markov chain Monte Carlo exploration for a number of steps sufficient to distance itself from its parent. However, this exploration is subject to the constraint that the chain's final location must have a probability greater than L^* ; in other words, the new sample must be drawn from the region of the parameter space inside the likelihood contour defined by the previous low-probability sample. Once a suitable new location has been selected, a new iteration begins. Due to the restriction on movement imposed by L^* updating at every step, the subset of the parameter space sampled by the N objects gradually shrinks. Eventually, the bulk of the posterior density is sufficiently sampled, so that new contributions to Z are miniscule. At this point, the iterations can be terminated, and parameter estimates are determined directly from the stored Monte Carlo samples. A schematic of a simple one-dimensional example of nested sampling is shown in Fig. 4.4. Note how the portion of the parameter space accessible to replacement samples decreases (subject to L^*) as the iteration number increases. In higher dimensions, the constraint imposed by L^* takes the form of a contour rather than a horizontal line.

In summary, the algorithm proceeds by

1. Sample N points from the prior probability. Initialize $Z = 0$ and $X_0 = 1$.
2. While the number of iterations is less than the desired stopping point,
 - (a) Find the sample with the lowest probability and store its likelihood as L^* .
 - (b) Set $X_k = \exp(-k/N)$.
 - (c) Increment Z by $L^*(X_{k-1} - X_k)$.
 - (d) Draw a new sample within the contour defined by L^* using MCMC.

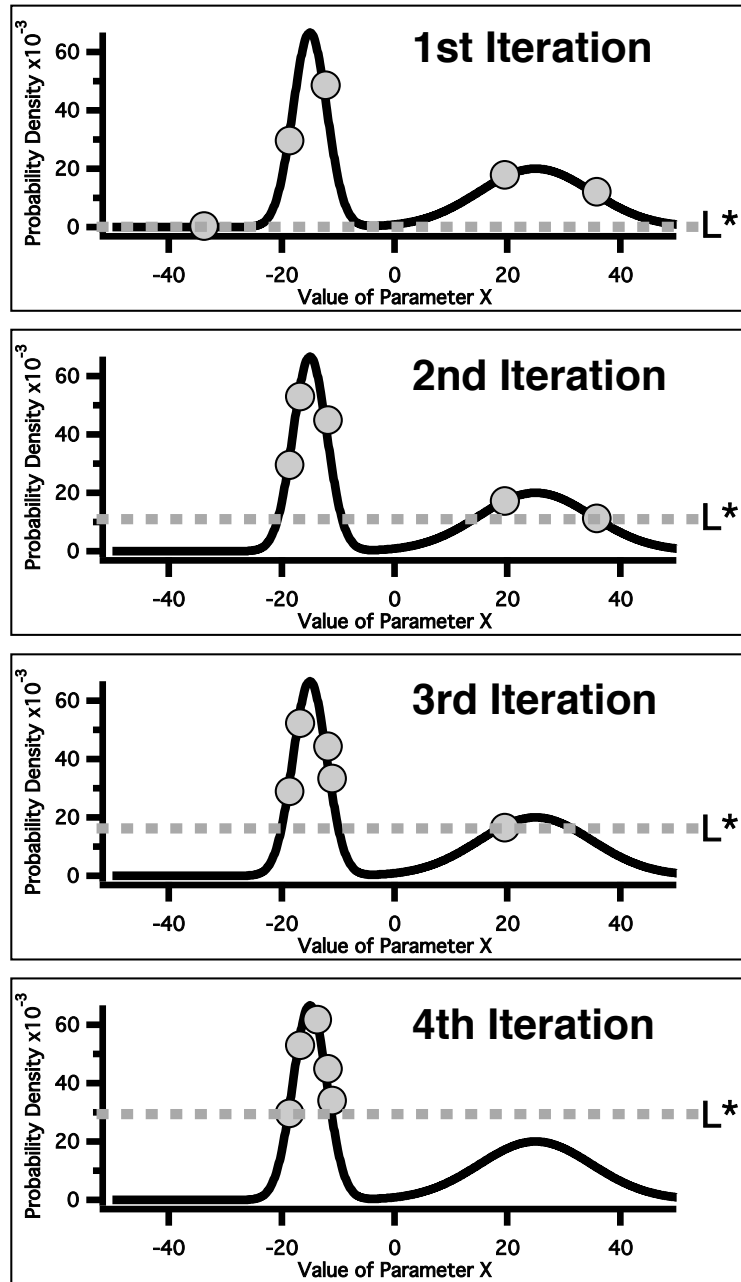


FIGURE 4.4: Schematic of nested sampling acting on a one-dimensional target distribution (black lines). The live samples are represented by gray circles. The likelihood constraint L^* defined by the lowest-probability sample (horizontal dashed line) moves upward at each iteration, compressing the subset of the parameter space where the samples are allowed to exist into the high-probability region.

Nested sampling has the advantage of direct computation of the evidence Z , if desired; this feature is particularly useful for model selection problems. However, a drawback is that parallelization, while possible, is less natural and therefore more difficult than other MCMC algorithms. Nested sampling is used in the calculations described in Chapter 7 of this Dissertation.

Bibliography

- Bayes, T. (**1763**). “An essay towards solving a problem in the doctrine of chances”, *Phil Trans R Soc* **53**.
- Behrends, E. (**2000**). *Introduction to Markov Chains* (Vieweg).
- Bretthorst, G. L., Hutton, W. C., Garbow, J. R., and Ackerman, J. J. (**2005a**). “Exponential model selection (in NMR) using Bayesian probability theory”, *Concepts Magn Reson* **27A**, 64–72.
- Bretthorst, G. L., Hutton, W. C., Garbow, J. R., and Ackerman, J. J. (**2005b**). “Exponential parameter estimation (in NMR) using Bayesian probability theory”, *Concepts Magn Reson* **27A**, 55–63.
- Cox, R. T. (**1946**). “Probability, frequency and reasonable expectation”, *Am J Phys* **14**, 1–13.
- Eckhardt, R. (**1987**). “Stan Ulam, John von Neumann, and the Monte Carlo method”, *Los Alamos Science* 131–141.
- Gelfand, A. and Smith, A. (**1990**). “Sampling-based approaches to calculating marginal densities”, *J Am Stat Assoc* **85**, 398–409.
- Gilks, W. R., Richardson, S., and Spiegelhalter, D. J. (**1996**). *Markov Chain Monte Carlo in Practice* (Chapman & Hall).
- Gregory, P. (**2005**). *Bayesian Logical Data Analysis for the Physical Sciences* (Cambridge Univ Press).
- Hastings, W. (**1970**). “Monte Carlo sampling methods using Markov chains and their applications”, *Biometrika* **57**, 97–109.
- Jaynes, E. T. (**1986**). “Bayesian methods: an introductory tutorial”, in *Maximum entropy and Bayesian methods in applied statistics*, edited by J. H. Justice (Cambridge Univ Press).
- Jaynes, E. T. (**2003**). *Probability theory: the logic of science* (Cambridge Univ Press).
- Jeffreys, H. (**1939**). *Theory of probability* (Oxford Univ Press).
- Kirkpatrick, S., Gelatt, C., and Vecchi, M. (**1983**). “Optimization by simulated annealing”, *Science* **220**, 671–680.
- Laplace, P. S. (**1812**). *Theorie Analytique des Probabilites* (Courcier).
- Laplace, P. S. (**1814**). *Essai Philosophique sur les Probabilites* (Courcier).

- Madras, N. (2002). *Lectures on Monte Carlo Methods* (American Mathematical Society).
- Metropolis, N. (1987). “The beginning of the Monte Carlo method”, *Los Alamos Science* 125–130.
- Metropolis, N., Rosenbluth, A., Rosenbluth, M., Teller, A., and Teller, E. (1953). “Equation of state calculations by fast computing machines”, *J Chem Phys* **21**, 1087–1092.
- Metropolis, N. and Ulam, S. (1949). “The Monte Carlo method”, *J Am Stat Assoc* **44**, 335–341.
- Roberts, G., Gelman, A., and Gilks, W. (1997). “Weak convergence and optimal scaling of random walk Metropolis algorithms”, *Ann Appl Probab* **7**, 110–120.
- Sivia, D. S. (2006). *Data analysis: a Bayesian tutorial* (Oxford Univ Press).
- Skilling, J. (2006). “Nested sampling for general Bayesian computation”, *Bayesian Analysis* **1**, 833–860.
- Stauffer, H. B. (2008). *Contemporary Bayesian and Frequentist Statistical Research Methods for Natural Resource Scientists* (Wiley).
- Tierney, L. (1994). “Markov chains for exploring posterior distributions”, *Ann Stat* 1701–1728.

CHAPTER 5

ESTIMATING FAST AND SLOW WAVE ULTRASONIC PROPERTIES IN BONE USING BAYESIAN PROBABILITY THEORY

5.1 Preface

This Chapter is based on the manuscript “Inverse problems in cancellous bone: estimation of the ultrasonic properties of fast and slow waves using Bayesian probability theory” written by Christian C. Anderson, Adam Q. Bauer, Mark R. Holland, Michal Pakula, Pascal Laugier, G. Larry Bretthorst, and James G. Miller. It is currently under review for publication in a peer-reviewed journal.

5.2 Abstract

Quantitative ultrasonic characterization of cancellous bone can be complicated by artifacts introduced by analyzing acquired data consisting of two propagating waves (a fast wave and a slow wave) as if only one wave were present. Recovering the ultrasonic properties of overlapping fast and slow waves could therefore lead to enhancement of bone quality assessment. The current study uses Bayesian probability theory to estimate phase velocity and normalized broadband ultrasonic attenuation (nBUA) parameters in a model of fast and slow wave propagation. Calculations are carried out using Markov chain Monte Carlo with simulated annealing to approximate the marginal posterior probability densities for parameters in the model. The technique is applied to simulated data, to data acquired on two phantoms capable of generating two waves in acquired signals, and to data acquired on a human femur condyle specimen. The models are in good agreement with both the simulated and experimental data, and the values of the estimated ultrasonic parameters fall within expected ranges.

5.3 Introduction

Quantitative ultrasound is a modality for evaluating changes in bone quality associated with osteoporosis (Barkmann *et al.*, 2008; Droin *et al.*, 1998; Haiat *et al.*, 2006; NIH, 2001; Padilla and Laugier, 2000; Pakula *et al.*, 2009; Petley *et al.*, 1995; Strelitzki and Evans, 1996; Wear *et al.*, 2000; Williams, 1992). Quantitative ultrasound

parameters, such as speed of sound and broadband ultrasonic attenuation (BUA), have been shown to correlate with bone mineral density (BMD) (Haïat *et al.*, 2006; Langton and Langton, 2000; Njeh *et al.*, 1997). The frequency dependence of phase velocity (i.e., dispersion) may also contain relevant clinical information, but it has not yet been demonstrated as a reliable indicator of bone quality.

Cancellous (trabecular) bone is a porous material found within the cavities of long bones and vertebrae. It consists of a complex matrix of hard spicules (trabeculae) interspersed with soft bone marrow. The complicated microstructure is known to support the propagation of multiple compressional ultrasonic wave modes, often referred to as fast waves and slow waves (Hosokawa, 2010; Fella *et al.*, 2008; Haïat *et al.*, 2008; Hosokawa and Otani, 1997, 1998; Lee *et al.*, 2007; Mizuno *et al.*, 2009). When cancellous bone samples are insonified in through-transmission studies, the two waves occasionally are separated and clearly distinct in the radiofrequency (rf) data. However, in some circumstances, the two waves can strongly overlap during the time period over which the rf data are acquired, resulting in interference and difficulties in distinguishing between the two waves (Padilla and Laugier, 2000; Haïat *et al.*, 2008; Hosokawa and Otani, 1998; Lee *et al.*, 2007; Anderson *et al.*, 2008; Marutyan *et al.*, 2006).

Ultrasonic measurements from many laboratories have revealed that cancellous bone exhibits a linear or nearly-linear increase in attenuation coefficient with frequency (Barkmann *et al.*, 2008; Droin *et al.*, 1998; Waters and Hoffmeister, 2005; Wear, 2007a, 2008). According to some forms of the causality-imposed Kramers-

Kronig (KK) relations that relate the frequency dependence of the phase velocity to the attenuation coefficient, materials that exhibit a linear-with-frequency increase in attenuation coefficient are expected to exhibit a logarithmic-with-frequency increase in phase velocity (Waters and Hoffmeister, 2005; Bauer *et al.*, 2007; O'Donnell *et al.*, 1978, 1981; Toll, 1956; Waters *et al.*, 2000b, 2003, 2005, 2000a). However, many laboratories report phase velocity measurements that decrease with frequency, a phenomenon known as anomalous negative dispersion (Droin *et al.*, 1998; Pakula *et al.*, 2009; Strelitzki and Evans, 1996; Anderson *et al.*, 2008; Marutyan *et al.*, 2006; Waters and Hoffmeister, 2005; Bauer *et al.*, 2008b; Nicholson *et al.*, 1996; Wear, 2000, 2007b, 2009). In an effort to explain the observed phase velocity dispersion, our Laboratory proposed that conventional phase spectroscopy analysis of acquired radiofrequency data might be influenced by the presence of multiple interfering compressional wave modes. In instances where fast and slow waves are overlapped, anomalous dispersion measurements could result from analyzing the interfering waves as if only one wave were present (Anderson *et al.*, 2008; Marutyan *et al.*, 2006). Numerical simulations demonstrated that when interference between a fast wave and a slow wave occurs, the acquired waveform exhibits apparent ultrasonic properties that differ from the true properties of the individual fast and slow waves (Anderson *et al.*, 2008; Marutyan *et al.*, 2006). Solving the inverse problem—that is, reconstructing the ultrasonic properties of the interfering fast and slow waves—could provide more reliable information about the medium under study. Studies undertaken by Sebaa *et al.* (2008), our Laboratory (Anderson *et al.*, 2007, 2009; Marutyan *et al.*, 2007b,a), and Wear

(2010) have addressed various ways of addressing inverse problems in the ultrasonic investigation of cancellous bone to accomplish these goals. The objective of the current study is to extend and enhance our Laboratory's proposed technique of using Bayesian probability theory to recover the properties of individual interfering waves in data acquired on bone and bone-mimicking phantoms.

5.4 Methods

5.4.1 Ultrasonic data acquisition

Two phantoms capable of producing two overlapping waves in acquired ultrasonic data were constructed from plastics. One phantom was constructed by machining a step discontinuity into a previously flat and parallel block of Lexan (polycarbonate thermoplastic resin). The thick portion of the block was 8.5 mm, and the thin portion of the block was 8.1 mm thick. Upon insonation, approximately half the ultrasonic beam propagates through the thick portion of the block, and half propagates through the thin side of the block. The difference in sample lengths for the two portions of the beam leads to two apparently independent waves in the acquired data. The size of the step discontinuity was chosen so that the fast and slow wave components would be approximately 180 degrees out of phase. Data were acquired on this phantom in a water tank using matched broadband 5 MHz center-frequency transducers in a through-transmission arrangement. The transducers were planar and had a diameter of 1.3 cm.

A second phantom was constructed from rectangular blocks of Plexiglas (poly-methyl methacrylate) and Lexan (polycarbonate thermoplastic resin). These blocks were bonded with Acrylic cement (IPS Corporation, Gardena, CA, USA) and machined so that the bonded material was flat and parallel, with a thickness of 1.1 cm. When this phantom is insonified near the boundary between the plastics, half of the ultrasonic beam travels through Lexan, and the other half travels through Plexiglas. Two waves arise in the acquired data because the speed of sound in Plexiglas is faster than the speed of sound in Lexan. To better approximate the conditions used in data acquisition on cancellous bone, especially the high kilohertz frequency range, data were acquired on this phantom using matched broadband 500 kHz center-frequency transducers in a through-transmission arrangement. These transducers were also planar and had a diameter of 2.9 cm. Schematics of the acquisition arrangement are shown in Fig. 5.1. Additionally, a human femur condyle specimen was prepared by machining the anterior and posterior sides of the condyle so that they were flat and parallel, with the trabecular structure exposed. The marrow was removed, and the sample was saturated with water. Data were acquired in a water tank at several spatial sites on the sample using a matched pair of 1 cm diameter, planar, 500 kHz center-frequency broadband transducers in a through transmission arrangement similar to the one used for data acquisition on the plastic bone-mimicking phantoms. The data acquired on the plastic phantoms and on the human bone sample served as input to a Bayesian program that estimated the ultrasonic parameters of a fast wave and a slow wave.

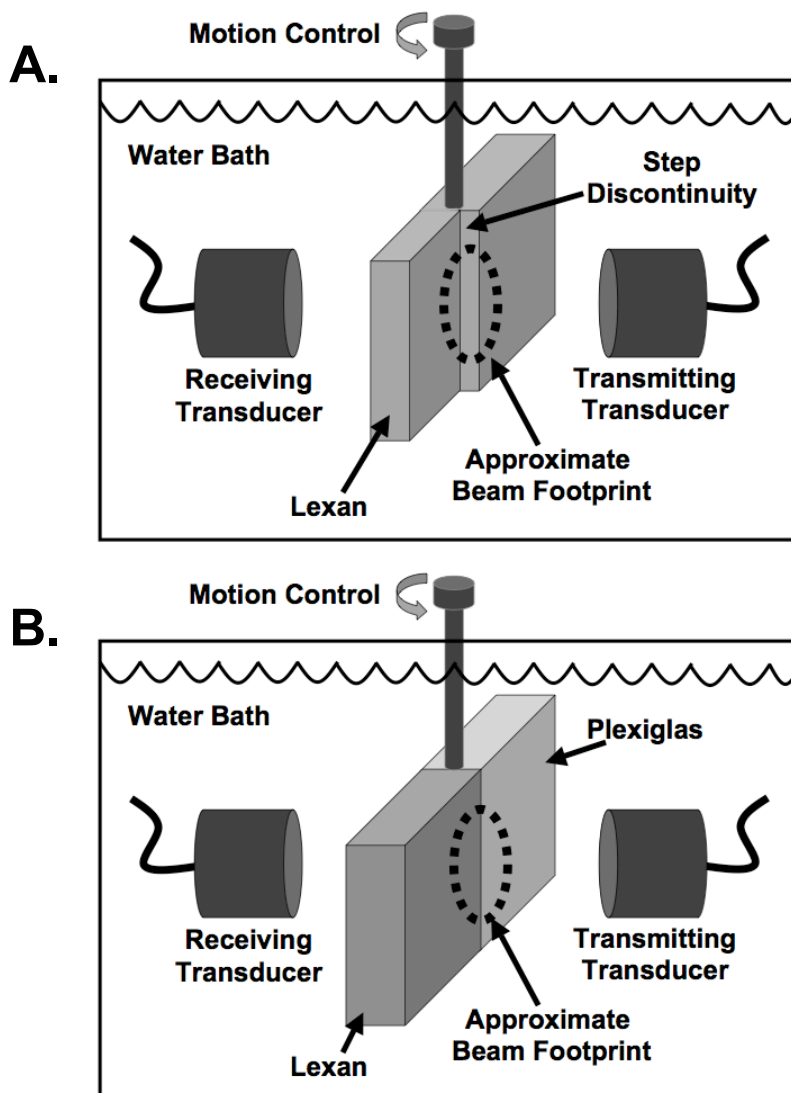


FIGURE 5.1: Data acquisition arrangement for the Lexan phantom with a step discontinuity (top, Panel A) and the phantom made from bonded Lexan and Plexiglas (bottom, Panel B).

5.4.2 Model of ultrasonic wave propagation

Time-domain ultrasonic data can be modeled as

$$\text{output}(f) = \text{input}(f) [H_{fast} + H_{slow}] + n \quad (5.1)$$

where $\text{output}(f)$ and $\text{input}(f)$ are the complex Fourier spectra of the model waveform and incident ultrasonic pulse, respectively, $H_{fast}(f)$ and $H_{slow}(f)$ are the transfer functions for the fast and slow waves, and n is an additive noise vector. When calculations were performed on the simulated input data, a simulated incident pulse was used to generate $\text{input}(f)$. When experimentally acquired data were used as input the calculations, a reference water-path signal was used as the source for $\text{input}(f)$.

The transfer functions are given by

$$H_{fast}(f) = A_{fast} \exp(-\beta_{fast}fd) \exp\left(\frac{i2\pi fd}{c_{fast}(f)}\right) \quad (5.2)$$

$$H_{slow}(f) = A_{slow} \exp(-\beta_{slow}fd) \exp\left(\frac{i2\pi fd}{c_{slow}(f)}\right) \quad (5.3)$$

where A_{fast} and A_{slow} are parameters that account for frequency-independent signal loss, such as transmission losses that might occur at interfaces between different media. The parameters β_{fast} and β_{slow} are the slopes of attenuation (nBUA) for the fast and slow waves, d is the thickness of the bone sample, and c_{fast} and c_{slow} are the phase velocities for the fast and slow waves. To ensure agreement with the Kramers-Kronig relations, the phase velocities are related to the attenuation coefficients by

$$c_{fast} = c_{fast}(f_0) + [c_{fast}(f_0)]^2 \frac{\beta_{fast}}{\pi^2} \log_e \left(\frac{f}{f_0} \right) \quad (5.4)$$

$$c_{slow} = c_{slow}(f_0) + [c_{slow}(f_0)]^2 \frac{\beta_{fast}}{\pi^2} \log_e \left(\frac{f}{f_0} \right) \quad (5.5)$$

where f_0 is a reference frequency chosen from within the experimental bandwidth and \log_e denotes the natural logarithm. In all calculations, f_0 was set at or near the middle of the experimental bandwidth, typically corresponding to a frequency near the center frequency of the transducer (either 500 kHz or 5 MHz for the experimentally acquired data).

In Eqs. (5.2-5.5), the nBUAs, β_{fast} and β_{slow} , are expressed in natural (i.e., base e) units (e.g. $\text{cm}^{-1}\text{MHz}^{-1}$). However, a common convention is to report nBUA in units of dB/cm/MHz. To avoid confusion, the notation β_{fast}^{dB} and β_{slow}^{dB} is used when referring to logarithmic values of nBUA, and β_{fast} and β_{slow} (without the superscript) is used when referring to natural units, with the understanding that

$$\beta_{fast}^{dB} = \frac{20}{\log_e(10)} \beta_{fast} \approx 8.69 \times \beta_{fast} \quad (5.6)$$

and that a similar relationship exists between β_{slow} and β_{slow}^{dB} .

5.4.3 Bayesian calculations

Bayesian probability theory (Sivia and Skilling, 2006) is used to estimate all of the parameters appearing in Eqs. (5.1-5.5). Bretthorst *et al.* (2005b) gives a detailed example of a calculation similar to the one carried out here. In Bayesian probability theory, everything known about a parameter is summarized by a probability density function. For example, the probability for $c_{slow}(f_0)$ is represented symbolically as $P(c_{slow}(f_0)|DI)$, where this notation should be understood as the posterior probabil-

ity for the parameter $c_{slow}(f_0)$ given the data D and the prior information I . The posterior probabilities for each individual parameter can all be computed from the joint posterior probability for all of the parameters by a process called marginalization, in which an integral over the joint posterior probability is performed over the uninteresting parameters. For example, if all of the parameters are represented as $\Theta = \{A_{fast}, \beta_{fast}, c_{fast}(f_0), A_{slow}, \beta_{slow}, c_{slow}(f_0)\}$, then the posterior probability for $c_{slow}(f_0)$ is computed as:

$$P(c_{slow}(f_0)) = \iiint\iiint P(\Theta|DI) dA_{fast}d\beta_{fast}dc_{fast}(f_0)dA_{slow}d\beta_{slow}, \quad (5.7)$$

where $P(\Theta|DI)$ is the joint posterior probability for all of the parameters. In a similar fashion, the posterior probabilities for the other parameters can be obtained by marginalizing over all of the parameters except the parameter of interest.

The joint posterior probability for all of the parameters is obtained by applying Bayes theorem,

$$P(\Theta|DI) = \frac{P(\Theta|I)P(D|\Theta I)}{P(D|I)}, \quad (5.8)$$

where $P(\Theta|I)$ is the prior probability for Θ given only I , $P(D|\Theta I)$ is the likelihood or the direct probability for the data given the parameters and the prior information, and $P(D|I)$ is a normalization constant.

Using the product rule of probability theory, the prior probability for the parameters can be factored,

$$P(\Theta|I) = P(A_{fast}|I)P(\beta_{fast}|I)P(c_{fast}(f_0)|I) \times \\ P(A_{slow}|I)P(\beta_{slow}|I)P(c_{slow}(f_0)|I). \quad (5.9)$$

TABLE 5.1: Prior probabilities for each model parameter. The means and standard deviations define Gaussian probability density functions that are bounded by the low and high values.

	Parameter					
	A_{fast}	A_{slow}	β_{fast}^{dB} (dB/cm/MHz)	β_{slow}^{dB} (dB/cm/MHz)	$c_{fast}(f_0)$ (m/s)	$c_{slow}(f_0)$ (m/s)
Low	0	0	0	0	1000	1000
Mean	0.5	0.5	43.4	43.4	2000	2000
High	1	1	86.8	86.8	3000	3000
Standard Deviation	0.5	0.5	43.4	43.4	1000	1000

To make this factorization, it has been assumed that each parameter is logically independent; i.e., each prior probability depends only on the parameter in question. For example, it has been assumed that what is known about A_{fast} does not depend on $c_{slow}(f_0)$, etc. In the calculation reported in this paper, it has been assumed that only vague prior information is available about each parameter. Because the prior information is vague, the functional form used to represent each prior probability is found to make very little difference in the resulting posterior probabilities. Consequently, these prior probabilities were assigned using bounded Gaussian distributions that provide order-of-magnitude estimates of each parameter. A summary of these order of magnitude estimates is given in Table 5.1.

Finally, the likelihood, $P(D|\Theta I)$ was assigned using a Gaussian prior probability to represent what was known about the noise. The standard deviation of this Gaussian was removed using marginalization with a Jeffreys prior (Jeffreys, 1961).

The calculation represented symbolically by Eq. (5.7) is a complicated five dimen-

sional integral that must be repeated six times, once for each parameter appearing in the model. Such multi-dimensional integrals are difficult or impossible to solve analytically. Consequently, a Markov chain Monte Carlo simulation with simulated annealing was used to approximate these integrals. More details on Bayesian probability theory are given by Sivia and Skilling (2006) and Bretthorst *et al.* (2005b), and further information on how Markov chain Monte Carlo is used in Bayesian probability theory is available in the literature (Bretthorst *et al.*, 2005a; Hastings, 1970; Metropolis *et al.*, 1953; Neal, 1993).

5.5 Results

5.5.1 Simulated data

As a preliminary investigation, simulated ultrasonic data were prepared using the model described in Eqs. (5.1-5.5), with varying levels of Gaussian noise added to the simulated signal to create three different simulated data sets with peak signal-to-noise ratios of 50:1, 100:1, and 250:1. In each case, the parameters used to create the simulated data were $\{A_{fast}, \beta_{fast}^{dB}, c_{fast}(f_0), A_{slow}, \beta_{slow}^{dB}, c_{slow}(f_0)\} = \{0.4, 20 \text{ dB/cm/MHz}, 1600 \text{ m/s}, 0.6, 6.9 \text{ dB/cm/MHz}, 1500 \text{ m/s}\}$, values previously shown to generate a negative dispersion using this model for acoustic wave propagation in bone (Anderson *et al.*, 2008). The value of f_0 was set at 300 kHz, and the propagation distance was set at 1 cm.

A comparison of the input fast and slow waves to the estimated fast and slow

TABLE 5.2: The input values of the model parameters used to construct simulated data sets are compared to the output means and standard deviations of the Monte Carlo samples computed using Bayesian probability theory.

	Parameter					
	A_{fast}	A_{slow}	β_{fast}^{dB} (dB/cm/MHz)	β_{slow}^{dB}	$c_{fast}(f_0)$	$c_{slow}(f_0)$ (m/s)
Input Value	0.40	0.60	20	6.9	1600	1500
SNR 50:1	0.38 ± 0.03	0.62 ± 0.02	19.2 ± 1.3	7.2 ± 0.3	1605 ± 7	1500 ± 0.4
SNR 100:1	0.38 ± 0.02	0.61 ± 0.01	19.0 ± 0.7	7.1 ± 0.2	1605 ± 3	1500 ± 0.2
SNR 250:1	0.38 ± 0.01	0.61 ± 0.005	19.4 ± 0.3	7.1 ± 0.1	1603 ± 2	1500 ± 0.1

waves is shown in Fig. 5.2. The simulated data used in this example had a signal-to-noise ratio of 50:1, and the estimated fast and slow waves were generated from the parameters that had maximum posterior probability. The agreement between the simulated input and model output waves is excellent. In addition, the estimated parameters are in good agreement with the input values. The marginal distributions for each parameter in the model are shown in Fig. 5.3. Even when the signal-to-noise ratio is relatively poor, Bayesian probability theory successfully estimates the true input parameter values; the peak values of the marginal distributions do not change appreciably as signal quality changes. However, the benefit of high quality data is evident in that the widths of the marginal posterior probability density functions are reduced as the signal-to-noise ratio improves. A numerical summary of these results is presented in Table 5.2.

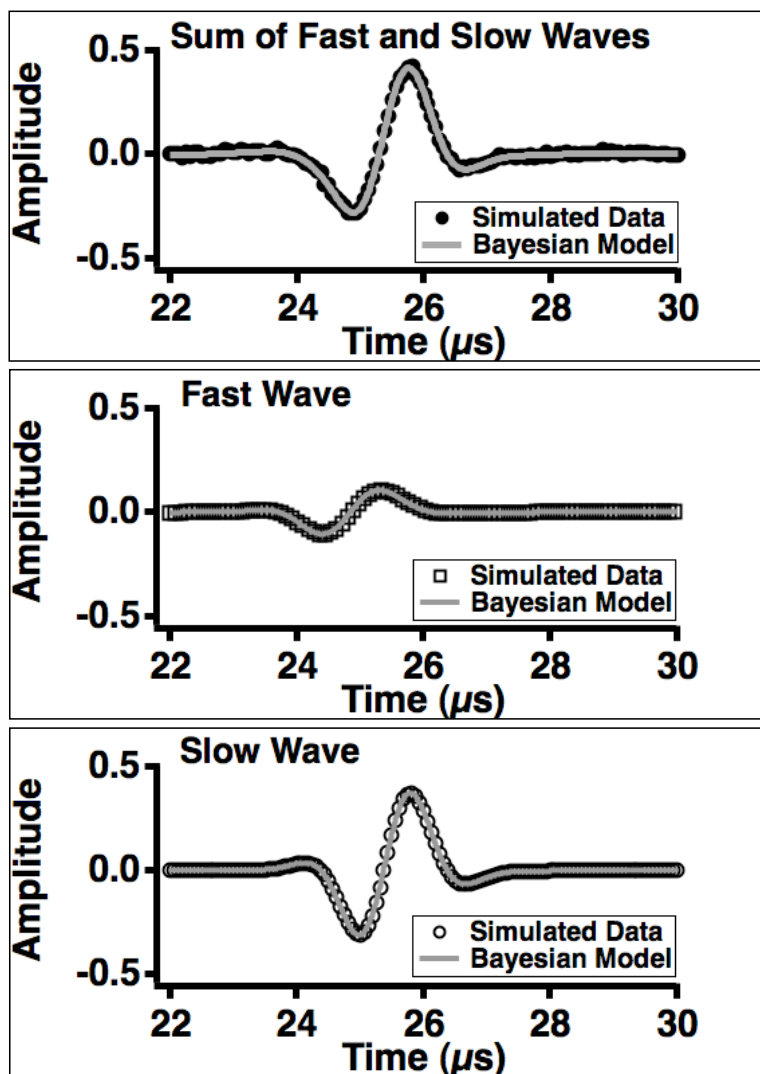


FIGURE 5.2: Input data to the Bayesian calculations (top panel, solid black circles) consisting of the sum of a simulated fast wave (middle panel, black squares) and slow wave (bottom panel, black circles). The output of the Bayesian calculations corresponding to each portion of the data is shown superimposed in a gray line. The signal-to-noise ratio in the input data is 50:1.

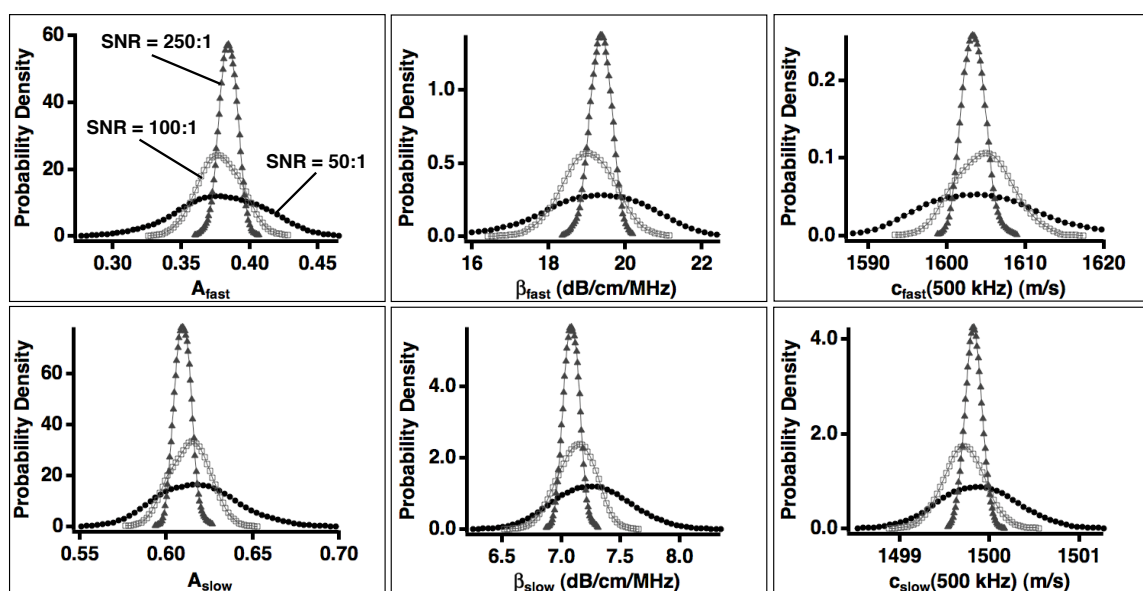


FIGURE 5.3: Marginal posterior probability density functions for the three sets of simulated data at varying signal-to-noise ratio (SNR) levels. All distributions integrate to 1. SNRs of 50:1, 100:1, and 250:1 are shown in circles, squares, and triangles, respectively. As the signal quality improves, the width of the distributions decreases, indicating increased confidence in the parameter value. However, the mean and peak parameter values do not change appreciably.

5.5.2 Phantom data

Ultrasonic data acquired on the Lexan phantom with a step discontinuity are shown in the top panel of Fig. 5.4, with the model constructed from the parameters that maximized the posterior probability shown superimposed on the data. In these calculations, the value of f_0 was set at 5 MHz and the distances of propagation for the fast and slow waves were set to the distances corresponding to the thick and thin portions of the Lexan phantom as measured with calipers. The individual fast and slow waves that comprise the model are shown in the corresponding lower panel. The qualitative agreement between the input data and the model constructed using Bayesian probability theory is excellent despite the large difference in the phases of the fast and slow waves. Moreover, as shown in Fig. 5.5, a conventional analysis of the acquired data in Fig. 5.4 yields large artifacts near 5 MHz in both the attenuation coefficient and phase velocity. In contrast, the attenuation coefficients and phase velocities of the fast and slow waves obtained with Bayesian probability theory do not exhibit such anomalous behavior, and are consistent with the expected values for Lexan. A summary of the parameter estimates (the means and standard deviations of the Monte Carlo samples), is given in Table 5.3. The properties of the fast and slow waves are similar because the medium under investigation in each case is Lexan. Similar results for the bonded Lexan and Plexiglas phantom are shown in Fig. 5.6. For these calculations, f_0 was set at 500 kHz and the propagation distance for each wave was set at 1.1 cm, the thickness of the phantom as measured with

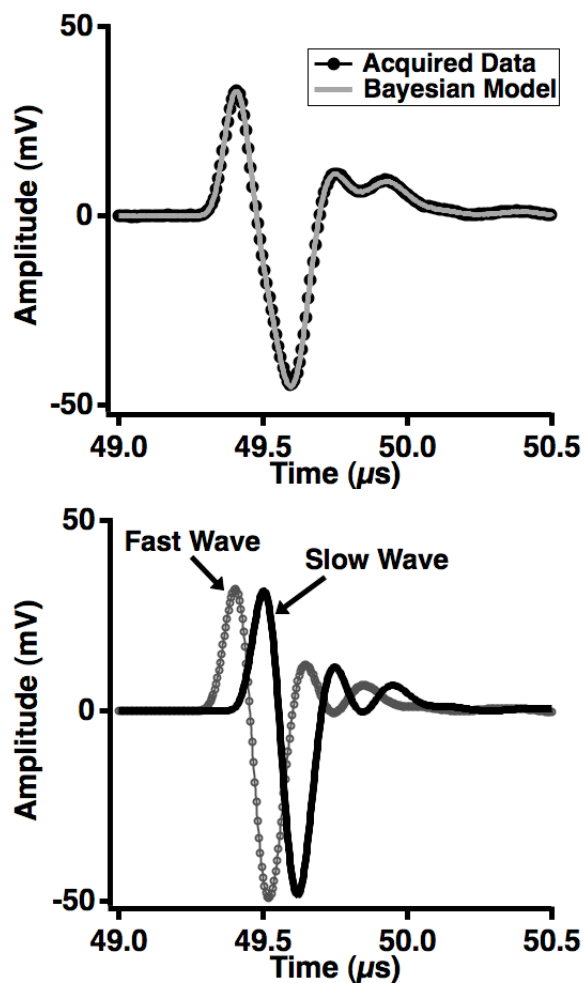


FIGURE 5.4: Data acquired at 5 MHz on a Lexan phantom with a step discontinuity (top panel, dark circles) with the model constructed from the parameters that maximized the joint posterior probability superimposed (top panel, gray line). The fast and slow waves that comprise the model are displayed in the bottom panel.

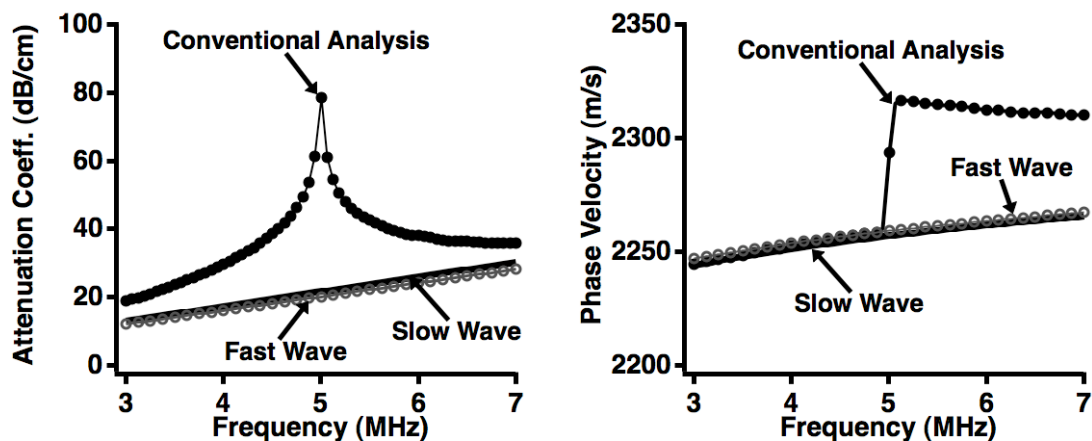


FIGURE 5.5: Conventional analysis of the data from a Lexan phantom with a step discontinuity yields significant artifacts in the attenuation coefficient and phase velocity near band center. In contrast, the curves for the fast and slow waves obtained using Bayesian probability theory are smoothly varying and consistent with a flat and parallel block of Lexan.

calipers. Each of these plastics has relatively low internal losses at frequencies in the 300-700 kHz bandwidth compared to those in the 3-7 MHz bandwidth. This effect is especially notable for Plexiglas, which has a relatively low nBUA even over megahertz bandwidths (on the order of 0.7 dB/cm/MHz from 3-7 MHz). Consequently, the frequency-dependent attenuation coefficient is more difficult to estimate in the hundreds of kilohertz frequency range, because energy loss is dominated by (approximately frequency-independent) reflection losses at the interfaces between the plastics and water. Nevertheless, the qualitative agreement between the model and the data remains quite good, and the ability of the Bayesian approach to estimate the fast and slow wave phase velocities is preserved despite the difficulties in estimating nBUA for the fast and slow waves. These additional complexities are not likely to persist in

TABLE 5.3: The expected values of the model parameters are taken from ultrasonic measurements performed on a flat and parallel block of Lexan. These expected values are compared to the means and standard deviations of the Monte Carlo samples computed using Bayesian probability theory for the data acquired on a block of Lexan with a step discontinuity.

	Parameter					
	A_{fast}	A_{slow}	β_{fast}^{dB} (dB/cm/MHz)	β_{slow}^{dB} (dB/cm/MHz)	$c_{fast}(f_0)$ (m/s)	$c_{slow}(f_0)$ (m/s)
Expected	–	–	4.2	4.2	2250	2250
Bayesian estimate	0.43 ± 0.01	0.44 ± 0.01	4.0 ± 0.1	4.3 ± 0.1	2259 ± 1	2257 ± 1

data acquired on cancellous bone because the attenuation coefficients are much larger than those in plastics (see Discussion section).

A summary of the parameter estimates for the velocity parameters in this data set is given in Table 5.4, with comparisons to approximate expected phase velocities at band center for individual Lexan and Plexiglas samples. Here, Plexiglas corresponds to the fast wave and Lexan corresponds to the slow wave.

5.5.3 Cancellous bone data

Acquired ultrasonic data and the corresponding Bayesian model for a single site on a human femur condyle are shown in Fig. 5.7, with the fast and slow waves generated using the parameters that had maximum posterior probability displayed in the lower panel. The calculations were performed with f_0 set to 500 kHz and the propagation distance set to 1.68 cm, the thickness of the bone sample. The complex

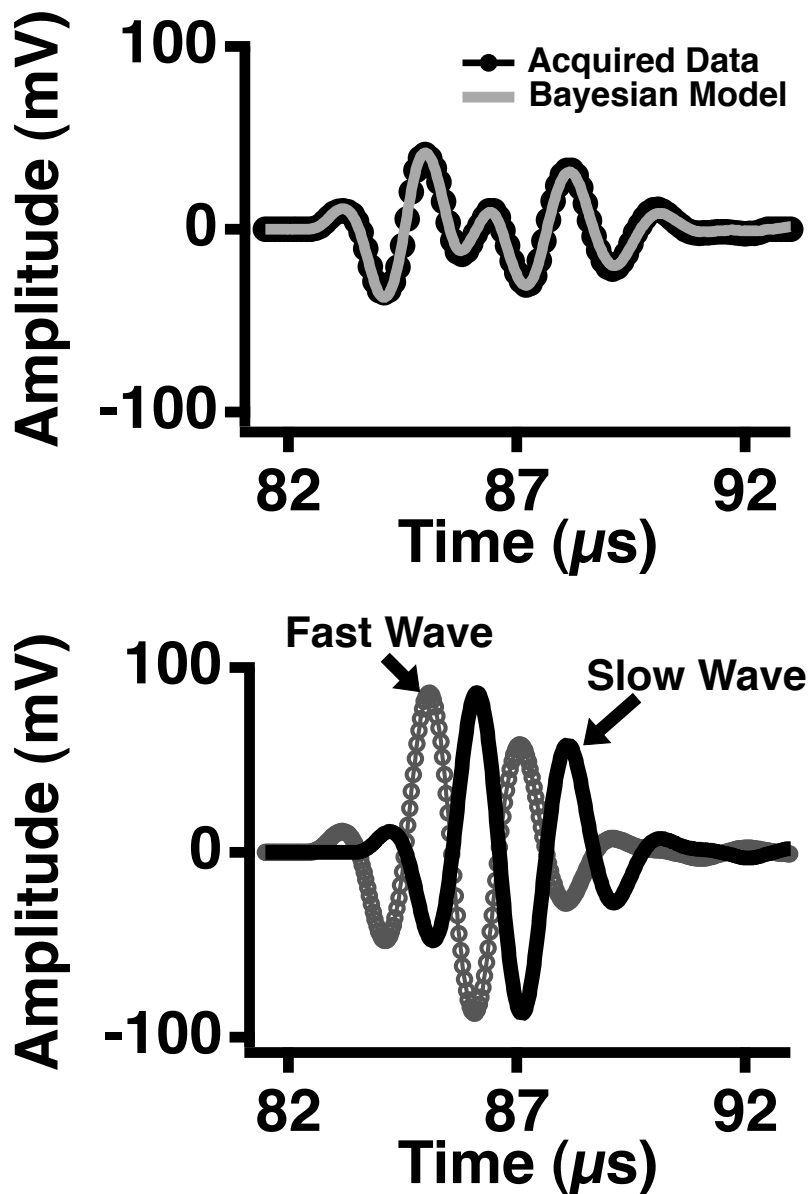


FIGURE 5.6: Data acquired at 500 kHz on a phantom constructed from bonded blocks of Lexan and Plexiglas (top panel, dark circles) with the model constructed from the parameters that maximized the joint posterior probability superimposed (top panel, gray line). The fast and slow waves that comprise the model are displayed in the bottom panel.

TABLE 5.4: The expected values of the model velocity parameters are taken from separate ultrasonic measurements performed on flat and parallel blocks of Lexan and Plexiglas. These expected values are compared to the means and standard deviations of the Monte Carlo samples computed using Bayesian probability theory for the data acquired on a phantom constructed by bonding blocks of Lexan and Plexiglas.

	Parameter	
	$c_{fast}(f_0)$	$c_{slow}(f_0)$
	(m/s)	
Expected	2735	2185
Bayesian estimate	2765 ± 1	2192 ± 1

structure of cancellous bone results in data that are less clean than the data acquired on flat and parallel blocks of plastic. In turn, the anticipated agreement between the data and model is lessened because the attenuation coefficients for the fast and slow waves may deviate from strict linearity, and thus the phase velocities become less logarithmic in nature. However, in spite of these anticipated challenges, the data and model for this site are in good agreement. Additionally, as shown in Fig. 5.8, the phase velocities for the fast and slow waves recovered using Bayesian methods are causally consistent. The conventionally measured dispersion for this site is shown in the left panel of Fig. 5.8 (black circles), and a negative dispersion is evident. The frequency dependence of this curve contrasts with that of the dispersion predicted by the Kramers-Kronig relations, given the nBUA at this site. However, the right panel of Fig. 5.8 shows that the dispersions for the fast and slow waves are positive and increasing, as required by the model. A summary of the parameter estimates for

TABLE 5.5: Means and standard deviations of the Monte Carlo samples computed using Bayesian probability theory for the data acquired on a human cancellous bone specimen taken from a femur condyle.

	Parameter					
	A_{fast}	A_{slow}	β_{fast}^{dB} (dB/cm/MHz)	β_{slow}^{dB}	$c_{fast}(f_0)$	$c_{slow}(f_0)$ (m/s)
Bayesian estimate	0.82 ± 0.05	0.23 ± 0.01	42.8 ± 1.2	5.2 ± 0.3	2036 ± 5	1511 ± 1

these data is given in Table 5.5.

The analysis was performed at nine different sites on the same femur condyle to verify that it could be applied to a variety of data acquired on cancellous bone. The peak values of β_{fast}^{dB} , β_{slow}^{dB} , $c_{fast}(500 \text{ kHz})$, and $c_{slow}(500 \text{ kHz})$ were recorded at each location and averaged to obtain mean values for each parameter across the nine spatial sites. The results are displayed in Fig. 5.9, with the error bars representing the standard deviation in the most probable values for the parameter estimates across all of the nine spatial locations. There is relatively little variance in $c_{fast}(500 \text{ kHz})$ and $c_{slow}(500 \text{ kHz})$ over the spatial sites, but there is considerably more variation in β_{fast}^{dB} and β_{slow}^{dB} over the same locations.

5.6 Discussion

Analysis of ultrasonic data acquired on cancellous bone is often performed by using time-of-flight or phase spectroscopy methods to determine speeds of sound, and applying log spectral subtraction methods to obtain values for BUA or nBUA. Some

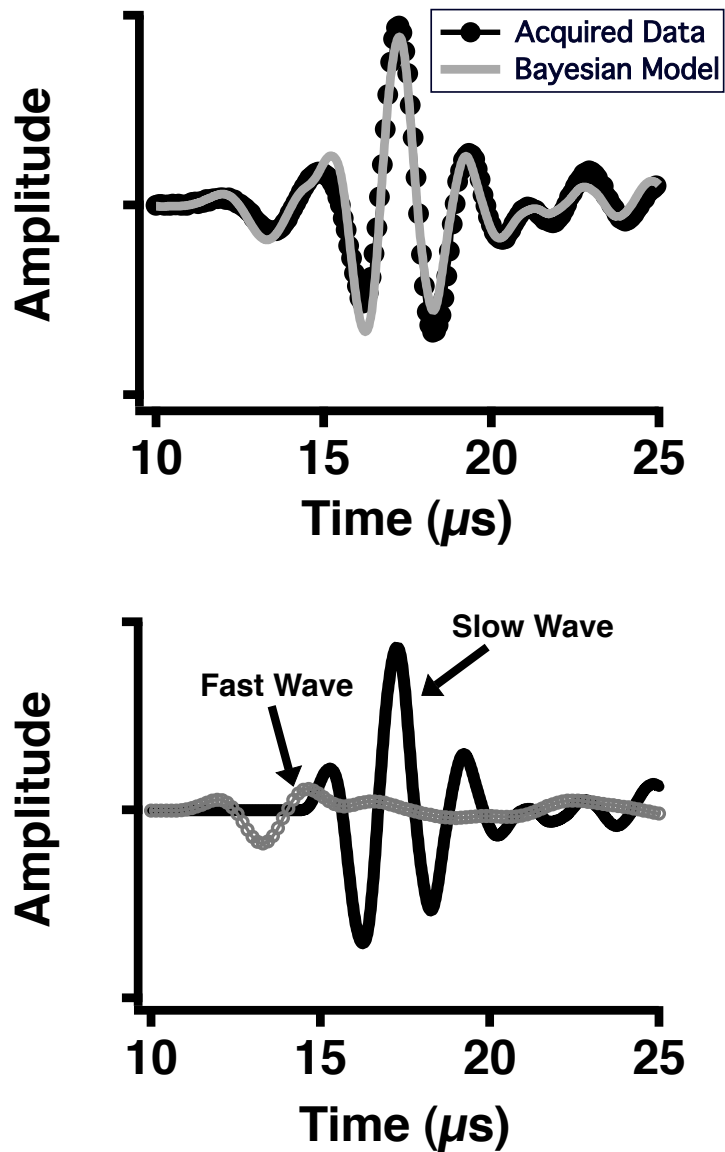


FIGURE 5.7: Data acquired at 500 kHz at one site on a human femur condyle specimen (top panel, dark circles) with the model constructed from the parameters that maximized the joint posterior probability superimposed (top panel, gray line). The fast and slow waves that comprise the model are displayed in the bottom panel.

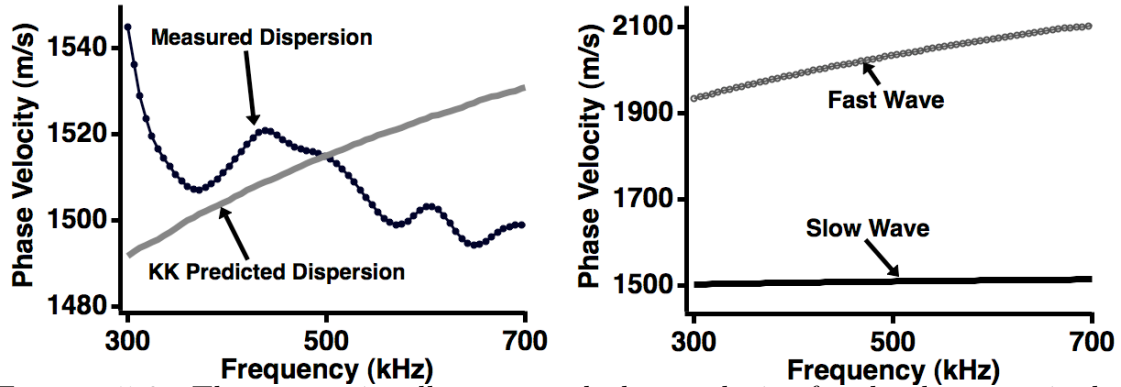


FIGURE 5.8: The conventionally measured phase velocity for the data acquired on a human femur condyle (left panel, dark circles) exhibits an anomalous negative dispersion, in contrast with the dispersion predicted by the Kramers-Kronig relations (left panel, gray curve). The fast and slow wave dispersions obtained using Bayesian probability theory (right panel) do not exhibit anomalous behavior.

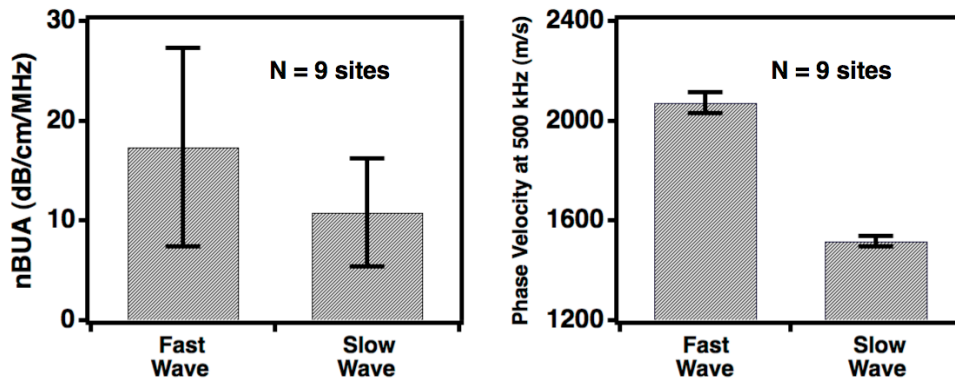


FIGURE 5.9: Values for nBUA and phase velocity at band center inferred by Bayesian probability theory for nine spatial locations within the same human femur condyle specimen. The phase velocities do not vary substantially over the nine sites, but there is considerable variation in nBUA.

assumptions underlying these approaches—namely, that the signal loss and attenuation coefficient of cancellous bone can be approximated by a linear relationship with frequency—have been explicitly incorporated into the model for ultrasonic wave propagation in bone used in the current study. Because the attenuation coefficient rises linearly with frequency, this model employs a dispersion that rises logarithmically with frequency as determined by the Kramers-Kronig relations. The heterogeneity and general complexity of cancellous bone structure appears to result in some deviation from these strict frequency dependences. Indeed, results presented above suggest that as analysis is performed on data obtained from specimens ranging from computer simulation, to homogeneous plastics, and to cancellous bone, these approximations become less satisfying. In spite of this trend, the fast and slow wave estimated parameters appear to be plausible and might in future studies be shown to be of diagnostic value. Furthermore, somewhat more sophisticated models for ultrasonic wave propagation can easily be incorporated into the Bayesian analysis introduced here if appropriate.

Other potential complicating experimental factors not directly accounted for in the model described here are the effects of diffraction and phase cancellation at the face of a piezoelectric receiver (Bauer *et al.*, 2008a, 2009). Because the model does not currently include a mechanism for these effects, systematic errors are introduced that could influence the parameter estimates, especially those that govern signal loss (A_{fast} , A_{slow} , β_{fast} , β_{slow}). It is challenging to determine how much, or in what capacity, these parameter estimates are affected. Interpretation of the estimated values

of A_{fast} and A_{slow} is particularly difficult, since these parameters presumably include contributions from insertion losses, diffraction, phase cancellation, and the distribution of energy among the fast and slow wave modes. These complicating factors are one of the reasons why, in Tables 3-5, no expected value for A_{fast} or A_{slow} is given. The nBUA parameters β_{fast} and β_{slow} can also suffer from a similar ambiguity in their interpretation in some circumstances. However, if the internal losses in the sample under investigation are large, nBUA parameters are dominated by the contributions of the attenuation coefficient; hence, the other complicating experimental factors can sometimes be ignored. This reasoning provides an explanation for the fact that the use of this model resulted in an accurate determination of nBUA for plastic phantoms over an experimental bandwidth of 3-7 MHz, where attenuation coefficients are relatively large, but failed to do so over an experimental bandwidth of 300-700 kHz, where attenuation coefficients are relatively small.

The results presented show that Bayesian probability theory can be used to determine the individual properties of overlapping and interfering fast and slow waves that are not obtained with more conventional analysis techniques. Direct computation of posterior probability density functions for each parameter, as approximated by Markov chain Monte Carlo simulations, provide an easily interpreted representation of all information about a given parameter. Traditionally, Bayesian analysis has been limited by the large computational resources needed to solve complicated problems. However, advances in computing technology have resulted in the ability to apply Bayesian probability theory to problems with high dimensionality and complexity

with reasonably short calculation times and at relatively low cost.

5.7 Conclusion

Bayesian probability theory has been applied to simulated ultrasonic data, to data acquired on two different plastic bone-mimicking phantoms, and to data from a human femur condyle specimen. Agreement between the models and data ranges from good to excellent. Marginal posterior probability densities for the model parameters accurately reflect true input values in simulated data and provide good estimates for the ultrasonic characteristics of the plastic bone-mimicking phantoms, although the analysis performs less well when the medium under study exhibits a small attenuation coefficient. Artifacts present in conventionally obtained phase velocities and attenuation coefficients are replaced by smoothly varying curves determined by probability theory.

Acknowledgment

This study was supported by NIH Grant R01-AR057433.

Bibliography

- Anderson, C. C., Marutyan, K. R., Holland, M. R., Wear, K. A., and Miller, J. G. (2008). “Interference between wave modes may contribute to the apparent negative dispersion observed in cancellous bone”, *J Acoust Soc Am* **124**, 1781–9.
- Anderson, C. C., Marutyan, K. R., Wear, K. A., Holland, M. R., Miller, J. G., and Bretthorst, G. L. (2007). “Model selection in ultrasonic measurements on trabecular bone”, *AIP Conference Proceedings* **954**, 337–345.
- Anderson, C. C., Pakula, M., Holland, M. R., Laugier, P., Bretthorst, G. L., and Miller, J. G. (2009). “Decomposition of interfering ultrasonic waves in bone and bone-mimicking materials”, *AIP Conference Proceedings* **1193**, 321–328.
- Barkmann, R., Laugier, P., Moser, U., Dencks, S., Klausner, M., Padilla, F., Haiat, G., Heller, M., and Glüer, C.-C. (2008). “In vivo measurements of ultrasound transmission through the human proximal femur”, *Ultrasound Med Biol* **34**, 1186–90.
- Bauer, A., Anderson, C., Holland, M., and Miller, J. (2008a). “Measurement artifacts in sonometry of cancellous bone: The relative impact of phase cancellation and interference on measurements of phase-distorting phantoms”, *2008 IEEE International Ultrasonics Symposium Proceedings* 137 – 141.
- Bauer, A., Marutyan, K., Holland, M., and Miller, J. (2007). “Is the kramers-kronig relationship between ultrasonic attenuation and dispersion maintained in the presence of apparent losses due to phase cancellation?”, *J Acoust Soc Am* **122**, 222–228.
- Bauer, A. Q., Anderson, C. C., Holland, M. R., and Miller, J. G. (2009). “Bone sonometry: reducing phase aberration to improve estimates of broadband ultrasonic attenuation”, *J Acoust Soc Am* **125**, 522–9.
- Bauer, A. Q., Marutyan, K. R., Holland, M. R., and Miller, J. G. (2008b). “Negative dispersion in bone: the role of interference in measurements of the apparent phase velocity of two temporally overlapping signals”, *J Acoust Soc Am* **123**, 2407–14.
- Bretthorst, G. L., Hutton, W. C., Garbow, J. R., and Ackerman, J. J. (2005a). “Exponential model selection (in nmr) using Bayesian probability theory”, *Concepts Magn Reson* **27A**, 64–72.
- Bretthorst, G. L., Hutton, W. C., Garbow, J. R., and Ackerman, J. J. (2005b). “Exponential parameter estimation (in nmr) using Bayesian probability theory”, *Concepts Magn Reson* **27A**, 55–63.
- Droin, P., Berger, G., and Laugier, P. (1998). “Velocity dispersion of acoustic waves in cancellous bone”, *IEEE Trans Ultrason Ferroelectr Freq Control* **45**, 581–92.

- Fellah, Z., Sebaa, N., Fellah, M., Mitri, F., Ogam, E., Lauriks, W., and Depollier, C. (2008). “Application of the Biot model to ultrasound in bone: direct problem”, *IEEE Trans Ultrason Ferroelectr Freq Control* **55**, 1508 – 1515.
- Haïat, G., Padilla, F., Cleveland, R. O., and Laugier, P. (2006). “Effects of frequency-dependent attenuation and velocity dispersion on in vitro ultrasound velocity measurements in intact human femur specimens”, *IEEE Trans Ultrason Ferroelectr Freq Control* **53**, 39–51.
- Haïat, G., Padilla, F., Peyrin, F., and Laugier, P. (2008). “Fast wave ultrasonic propagation in trabecular bone: numerical study of the influence of porosity and structural anisotropy”, *J Acoust Soc Am* **123**, 1694–705.
- Hastings, W. (1970). “Monte carlo sampling methods using markov chains and their applications”, *Biometrika* 97–109.
- Hosokawa (2010). “Effect of porosity distribution in the propagation direction on ultrasound waves through cancellous bone”, *Ultrasonics, Ferroelectrics and Frequency Control, IEEE Transactions on* **57**, 1320 – 1328.
- Hosokawa, A. and Otani, T. (1997). “Ultrasonic wave propagation in bovine cancellous bone”, *J Acoust Soc Am* **101**, 558–62.
- Hosokawa, A. and Otani, T. (1998). “Acoustic anisotropy in bovine cancellous bone”, *J Acoust Soc Am* **103**, 2718–22.
- Jeffreys, H. (1961). *Theory of Probability* (Oxford Univ Press).
- Langton, C. M. and Langton, D. K. (2000). “Comparison of bone mineral density and quantitative ultrasound of the calcaneus: site-matched correlation and discrimination of axial BMD status.”, *Br J Radiol* **73**, 31–35.
- Lee, K. I., Hughes, E. R., Humphrey, V. F., Leighton, T. G., and Choi, M. J. (2007). “Empirical angle-dependent Biot and MBA models for acoustic anisotropy in cancellous bone.”, *Phys Med Biol* **52**, 59–73.
- Marutyan, K. R., Anderson, C. C., Wear, K. A., Holland, M. R., Miller, J. G., and Bretthorst, G. L. (2007a). “Parameter estimation in ultrasonic measurements on trabecular bone”, *AIP Conference Proceedings* **954**, 329–336.
- Marutyan, K. R., Bretthorst, G. L., and Miller, J. G. (2007b). “Bayesian estimation of the underlying bone properties from mixed fast and slow mode ultrasonic signals”, *J Acoust Soc Am* **121**, EL8–15.
- Marutyan, K. R., Holland, M. R., and Miller, J. G. (2006). “Anomalous negative dispersion in bone can result from the interference of fast and slow waves”, *J Acoust Soc Am* **120**, EL55–61.

- Metropolis, N., Rosenbluth, A., Rosenbluth, M., Teller, A., and Teller, E. (1953). "Equation of state calculations by fast computing machines", *The Journal of Chemical Physics* .
- Mizuno, K., Matsukawa, M., Otani, T., Laugier, P., and Padilla, F. (2009). "Propagation of two longitudinal waves in human cancellous bone: an in vitro study", *J Acoust Soc Am* **125**, 3460–6.
- Neal, R. (1993). "Probabilistic inference using markov chain monte carlo methods", Citeseer .
- Nicholson, P. H., Lowet, G., Langton, C. M., Dequeker, J., and der Perre, G. V. (1996). "A comparison of time-domain and frequency-domain approaches to ultrasonic velocity measurement in trabecular bone", *Physics in medicine and biology* **41**, 2421–35.
- NIH (2001). "Osteoporosis prevention, diagnosis, and therapy", *JAMA* **285**, 785–95.
- Njeh, C. F., Kuo, C. W., Langton, C. M., Atrah, H. I., and Boivin, C. M. (1997). "Prediction of human femoral bone strength using ultrasound velocity and BMD: an in vitro study", *Osteoporos Int* **7**, 471–7.
- O'Donnell, M., Jaynes, E., and Miller, J. (1978). "General relationships between ultrasonic attenuation and dispersion", *J Acoust Soc Am* **63**, 1935–1937.
- O'Donnell, M., Jaynes, E. T., and Miller, J. G. (1981). "Kramers-kronig relationship between ultrasonic attenuation and phase velocity", *J Acoust Soc Am* **69**, 696–701.
- Padilla, F. and Laugier, P. (2000). "Phase and group velocities of fast and slow compressional waves in trabecular bone", *J Acoust Soc Am* **108**, 1949–52.
- Pakula, M., Padilla, F., and Laugier, P. (2009). "Influence of the filling fluid on frequency-dependent velocity and attenuation in cancellous bones between 0.35 and 2.5 mhz", *J Acoust Soc Am* **126**, 3301–3310.
- Petley, G. W., Robins, P. A., and Aindow, J. D. (1995). "Broadband ultrasonic attenuation: are current measurement techniques inherently inaccurate?", *Br J Radiol* **68**, 1212–4.
- Sebaa, N., Fellah, Z., Fellah, M., Ogam, E., Mitri, F., Depollier, C., and Lauriks, W. (2008). "Application of the Biot model to ultrasound in bone: inverse problem", *IEEE Trans Ultrason Ferroelectr Freq Control* **55**, 1516 – 1523.
- Sivia, D. S. and Skilling, J. (2006). *Data analysis: a Bayesian tutorial* (Oxford Univ Press).
- Strelitzki, R. and Evans, J. (1996). "On the measurement of the velocity of ultrasound in the os calcis using short pulses", *Eur J Ultrasound* **4**, 205–213.

- Toll, J. S. (1956). “Causality and the dispersion relation: Logical foundations”, *Phys Rev* **104**, 1760–1770.
- Waters, K., Hughes, M., Brandenburger, G., and Miller, J. (2000a). “On a time-domain representation of the kramers-kronig dispersion relations”, *J Acoust Soc Am* **108**, 2114–9.
- Waters, K., Hughes, M., Mobley, J., and Miller, J. (2003). “Differential forms of the kramers-kronig dispersion relations”, *IEEE Trans Ultrason Ferroelectr Freq Control* **50**, 68 – 76.
- Waters, K., Mobley, J., and Miller, J. (2005). “Causality-imposed (kramers-kronig) relationships between attenuation and dispersion”, *IEEE Trans Ultrason Ferroelectr Freq Control* **52**, 822 – 823.
- Waters, K. R. and Hoffmeister, B. K. (2005). “Kramers-kronig analysis of attenuation and dispersion in trabecular bone”, *J Acoust Soc Am* **118**, 3912–20.
- Waters, K. R., Hughes, M. S., Mobley, J., Brandenburger, G. H., and Miller, J. G. (2000b). “On the applicability of kramers–kronig relations for ultrasonic attenuation obeying a frequency power law”, *J Acoust Soc Am* **108**, 556–563.
- Wear, K. (2010). “Decomposition of two-component ultrasound pulses in cancellous bone using modified least squares prony method-phantom experiment and simulation”, *Ultrasound Med Biol* **36**, 276–287.
- Wear, K. A. (2000). “Measurements of phase velocity and group velocity in human calcaneus”, *Ultrasound Med Biol* **26**, 641–6.
- Wear, K. A. (2007a). “The effect of phase cancellation on estimates of calcaneal broadband ultrasound attenuation in vivo”, *IEEE Trans Ultrason Ferroelectr Freq Control* **54**, 1352–9.
- Wear, K. A. (2007b). “Group velocity, phase velocity, and dispersion in human calcaneus in vivo”, *J Acoust Soc Am* **121**, 2431–7.
- Wear, K. A. (2008). “The effect of phase cancellation on estimates of broadband ultrasound attenuation and backscatter coefficient in human calcaneus in vitro”, *IEEE Trans Ultrason Ferroelectr Freq Control* **55**, 384–90.
- Wear, K. A. (2009). “Frequency dependence of average phase shift from human calcaneus in vitro”, *J Acoust Soc Am* **126**, 3291–3300.
- Wear, K. A., Stuber, A. P., and Reynolds, J. C. (2000). “Relationships of ultrasonic backscatter with ultrasonic attenuation, sound speed and bone mineral density in human calcaneus”, *Ultrasound Med Biol* **26**, 1311–6.

Williams, J. L. (1992). “Ultrasonic wave propagation in cancellous and cortical bone: prediction of some experimental results by Biot’s theory”, *J Acoust Soc Am* **91**, 1106–12.

CHAPTER 6

ANISOTROPY OF ULTRASONIC PROPERTIES IN CANCELLOUS BONE

6.1 Preface

The material presented in this Chapter is the result of a collaborative effort with Professor Mami Matsukawa and her co-investigators at Doshisha University in Kyoto, Japan, who prepared bone specimens and acquired the data used in this investigation. The author is grateful for their assistance.

6.2 Introduction

Bone growth and remodeling is sensitive to mechanical stimulation (Njeh *et al.*, 1999). In cancellous bone, this manner of growth causes the trabeculae to tend to be aligned along the major stress axes. During standing or walking, the long bones of the leg experience stresses that tend to be oriented along the major axis of the bone. Thus, the trabecular structure in these bones usually has a preferred orientation parallel to the long axis, and is anisotropic. It should be noted, however, that although the trabeculae have a preferred orientation, the natural complexity of cancellous bone and the many interconnected trabeculae practically guarantee that no single direction can rigorously be defined as “parallel to the aligned trabeculae”. Because the mechanical properties of an anisotropic material are directionally dependent, it naturally follows that the ultrasonic properties are also dependent on the angle of insonation relative to the predominant orientation of the trabeculae.

In clinical bone sonometry of the heel, the ultrasonic waves usually propagate in the medial-lateral direction across the heel bone. In this geometry, the signals travel in a direction perpendicular to the predominant trabecular orientation. The potential for future devices to test bone quality along multiple axes provides motivation for a deeper understanding of the anisotropy of the measured ultrasonic parameters in bone. *In vitro* studies have examined the anisotropy of velocity in cancellous bone specimens (Mizuno *et al.*, 2009, 2008; Haiat *et al.*, 2008; Hosokawa and Otani, 1998).

As discussed in Chapters 3 and 5, the propagation of fast and slow waves in

cancellous bone can complicate measurements of velocity and attenuation properties. The same effects can complicate investigations of anisotropy in bone. Hosokawa and Otani (1998) were unable to measure distinct fast and slow wave velocities when the insonation angle was larger than approximately 40 degrees because the fast and slow waves became strongly overlapped as the insonation angle increased. Thus, methods for separating fast and slow waves from data in which they strongly overlap would benefit studies of anisotropy in cancellous bone. The method described in Chapter 5 is suitable for addressing this task.

6.3 Methods

6.3.1 Data acquisition

At Doshisha University in Kyoto, Japan, a spherical specimen approximately 12 mm in diameter was drawn from the distal epiphysis of a bovine femur. The specimen was defatted and mounted in a water tank. In the same water tank, a transmitting transducer with a focal length of 40 mm and a planar receiving transducer were arranged on either side of the specimen in a through-transmission arrangement. The initial direction of propagation through the sample was the superior-inferior direction, along the predominant trabecular orientation. The transmitter was excited by one cycle of a 1 MHz sinusoidal pulse. The signal was received after passing through the sample, digitized on an oscilloscope, and stored for off-line analysis. This process was repeated as the specimen was rotated in 10 degree increments between 0

and 180 degrees, allowing the data to be analyzed as a function of insonation angle relative to the predominant trabecular alignment.

6.3.2 Analysis

Data analysis was carried out in the Laboratory for Ultrasonics at Washington University in St. Louis. Bayesian probability theory as described in Chapter 5 was performed on data acquired at each insonation angle. The model used for fast and slow ultrasonic wave propagation in bone is the same one described in Section 5.4.2, in which the parameters to be estimated are $\{A_{fast}, \beta_{fast}, c_{fast}(f_0), A_{slow}, \beta_{slow}, c_{slow}(f_0)\}$. In this application, f_0 was set to 1 MHz, the center frequency of the transmitted signal.

6.4 Results

A representative portion of the experimental data and the models constructed using the most probable parameter values are shown in Fig. 6.1. In Fig. 6.1, the black lines are the acquired data and the gray curves are the models for the data. Results shown are when the angle of insonation θ was 0° (parallel), 30° , 60° , and 90° (perpendicular) to the predominant trabecular alignment. Anisotropy is evident in that fast and slow waves are easily identified in the acquired data at parallel insonation, but they become more and more overlapped as θ increases. At perpendicular insonation, discernment of individual fast and slow waves is problematic. In general, the models

are in good agreement with the data despite the difficult experimental factors noted in Section 5.6

The most probable parameter values for each insonation angle were stored. In Fig. 6.2, the parameters A_{fast} and A_{slow} are plotted at each angle. A_{fast} is at a maximum when insonation is parallel to the trabeculae and at a minimum when insonation is approximately perpendicular to the trabeculae. The opposite relationship exists for A_{slow} , which has a minimum at parallel insonation and a maximum near perpendicular insonation.

Anisotropy is also apparent in normalized Broadband Ultrasound Attenuation (nBUA) for the fast and slow waves, equivalent to the parameters β_{fast} and β_{slow} . As shown in Fig. 6.3, The fast wave exhibits more smoothly varying anisotropy for this sample compared to that of the slow wave, which does not have a pronounced maximum near 90 degrees. It is interesting to note that unlike A_{slow} , the parameter β_{slow} appears to have a maximum at approximately perpendicular insonation and a minimum at parallel insonation.

Signal loss is a measure that incorporates all factors contributing to A_{fast} and β_{fast} , and correspondingly A_{slow} and β_{slow} . The signal losses for the spherical bovine bone sample are displayed in Fig. 6.4 as a function of insonation angle. Like nBUA, signal loss for both waves achieves a maximum near 90 degrees and a minimum near 0 and 180 degrees.

Velocity should be expected to exhibit significant anisotropy based on qualitative observations of the data in Fig. 6.1, which indicate that the degree to which the fast

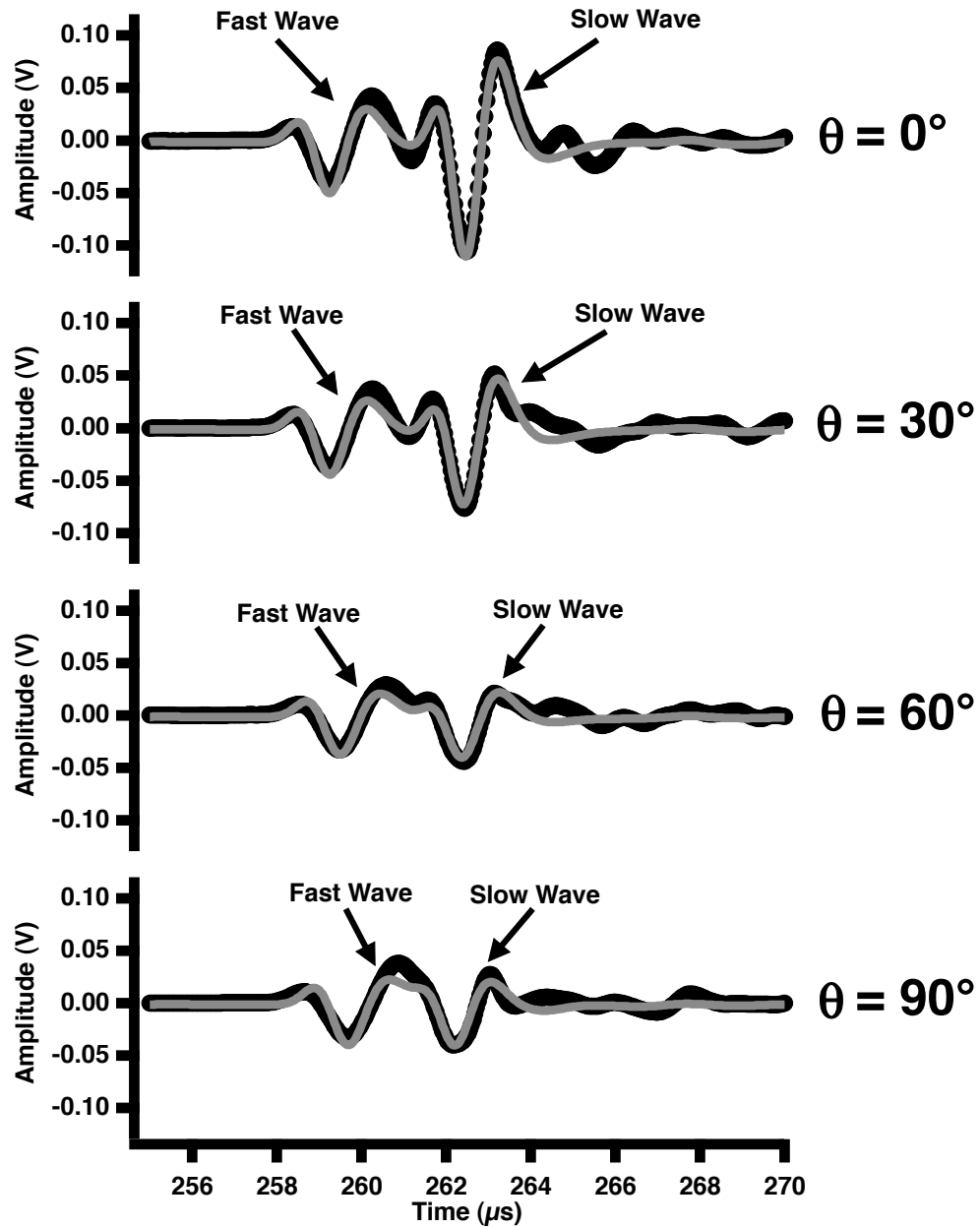


FIGURE 6.1: Acquired experimental data (black curves) and models constructed using Bayesian probability theory (gray curves) for a cancellous bone sample. The angles θ are insonation angles relative to the predominant trabecular alignment. As θ increases from parallel to perpendicular insonation, the fast and slow waves become more overlapped.

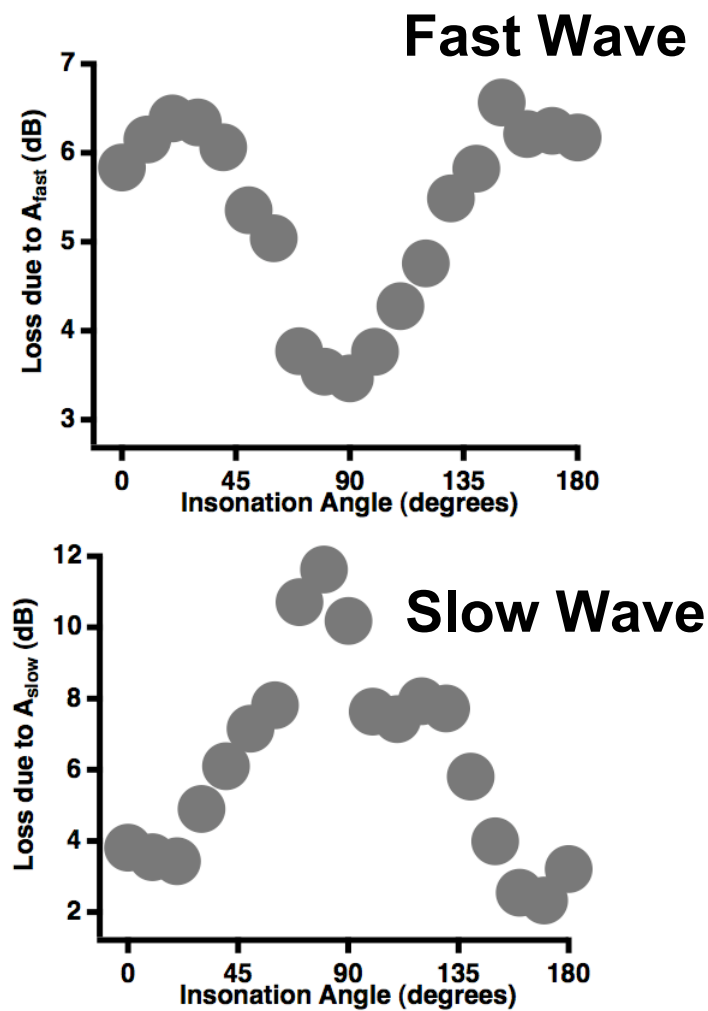


FIGURE 6.2: The most probable values for the parameters A_{fast} (top) and A_{slow} (bottom) as a function of insonation angle for a bovine cancellous bone specimen.

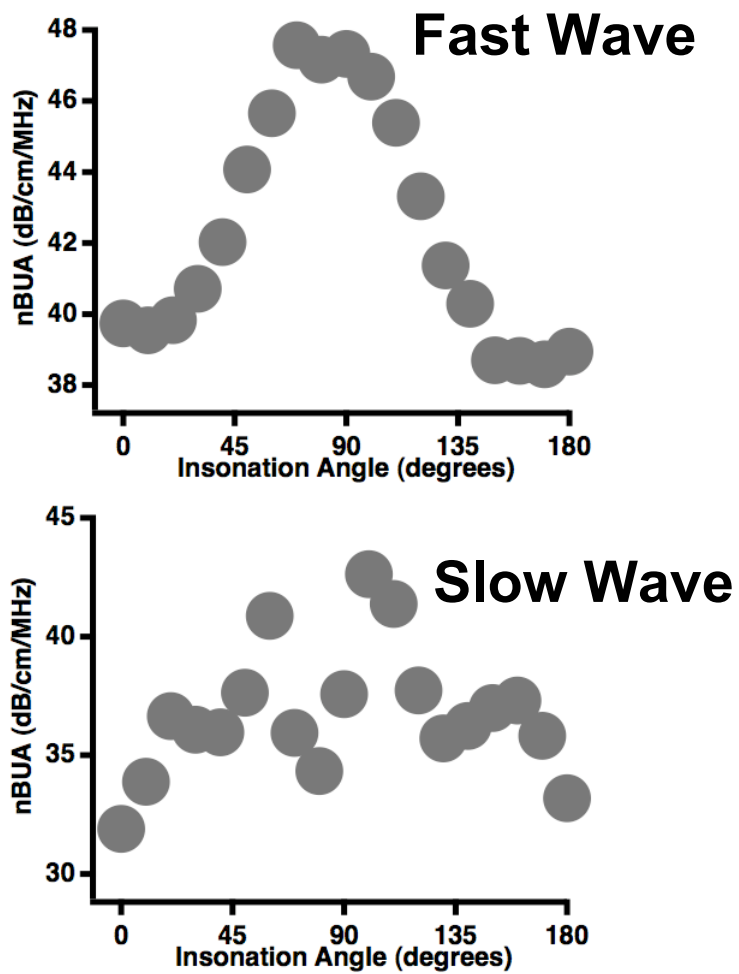


FIGURE 6.3: The most probable values for the parameters β_{fast} (top) and β_{slow} (bottom) as a function of insonation angle for a bovine cancellous bone specimen.

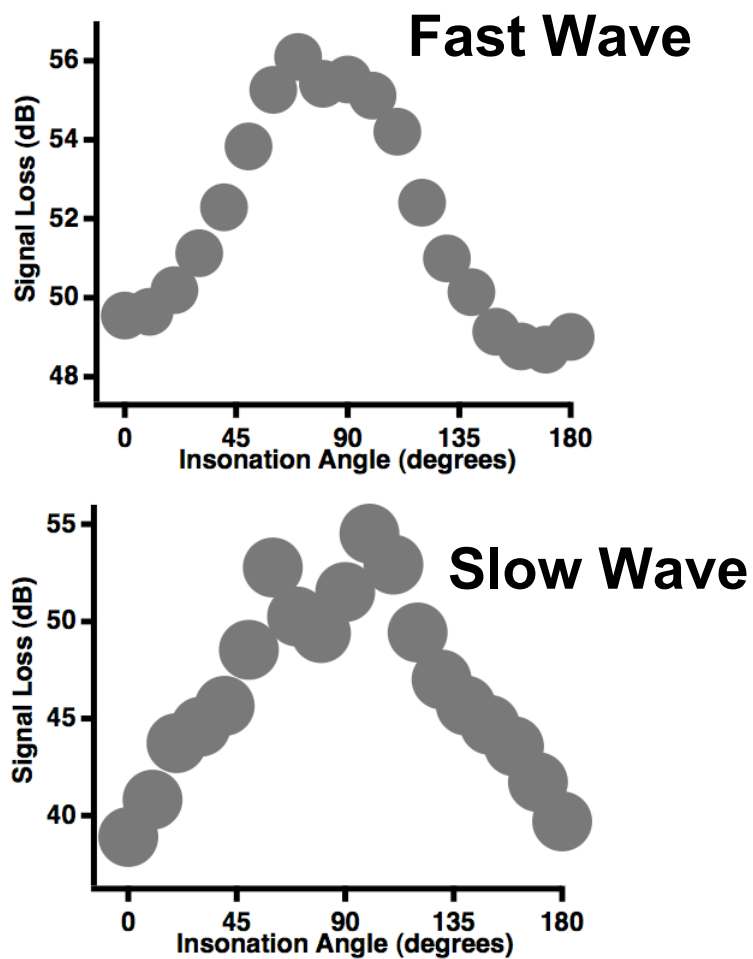


FIGURE 6.4: The signal loss at band center (1 MHz) as a function of insonation angle for a bovine cancellous bone specimen.

and slow waves overlap changes with insonation angle. The phase velocity at 1 MHz is displayed as a function of angle of insonation in Fig. 6.5. At parallel insonation, the fast wave has a maximum in velocity and the slow wave has a minimum. At perpendicular insonation, the situation is reversed; the fast wave velocity is at its minimum, and the slow wave velocity is at its maximum. Therefore, the difference in the velocities is maximized at parallel insonation, and the two waves should be expected to be more distinct in the acquired data. At perpendicular insonation, v_{fast} and v_{slow} are more similar, and more overlap should be anticipated.

An additional parameter of interest is the relative amplitude of the fast and slow waves. The wave amplitudes are determined by finding the maximum of the signal envelope. In Fig. 6.6, the ratio of the maximum amplitude of the fast wave and the maximum amplitude of the slow wave is plotted against insonation angle. A value of 1 indicates that the fast and slow waves have approximately equal amplitude. Again, the anisotropy is evident. The fast wave has approximately 40 percent of the amplitude of the slow wave at parallel insonation, but at perpendicular insonation the fast wave amplitude is higher than the slow wave amplitude.

6.5 Discussion

Using conventional analysis techniques, it can be difficult to fully determine the anisotropy of ultrasonic parameters in cancellous bone because of the strong overlap of fast and slow waves. For the data presented in the current study, accurate

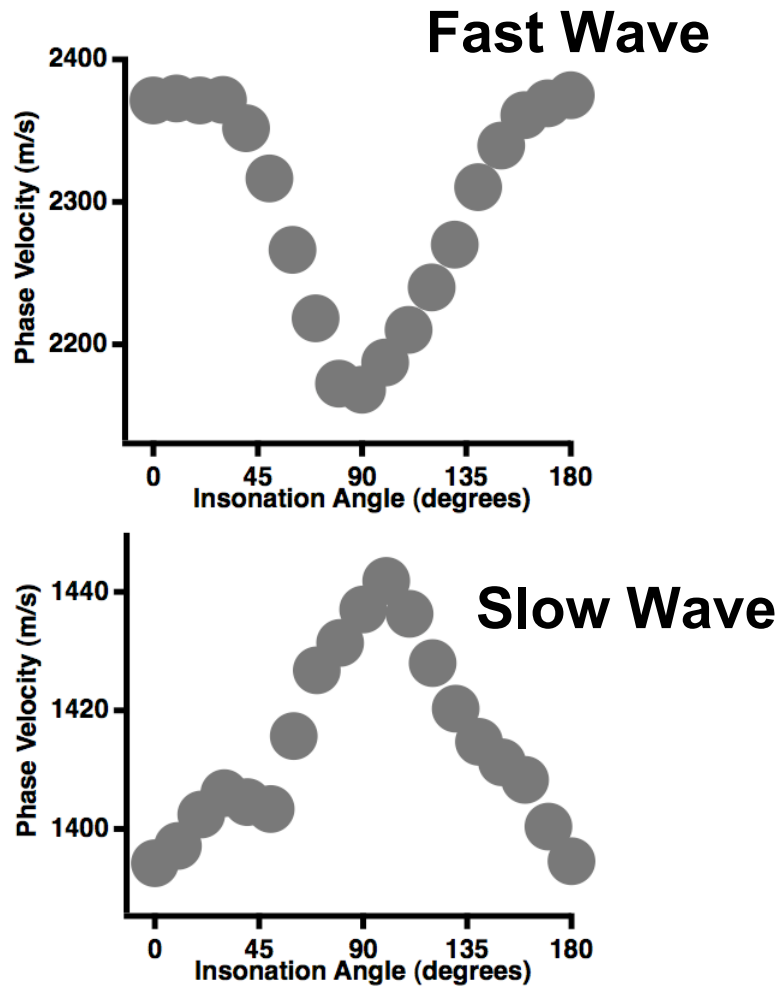


FIGURE 6.5: The most probable values for the parameters v_{fast} (top) and v_{slow} (bottom) as a function of insonation angle for a bovine cancellous bone specimen.

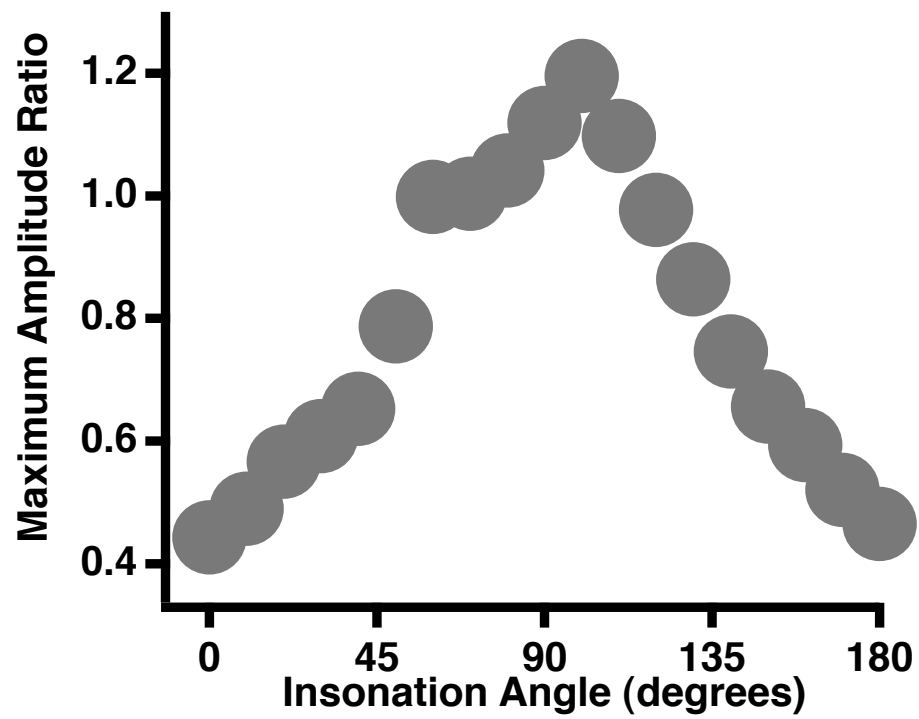


FIGURE 6.6: The ratio of maximum fast wave amplitude to maximum slow wave amplitude as a function of insonation angle for a bovine cancellous bone specimen.

determination of these parameters would be problematic as the angle of insonation approached 90 degrees. Fortunately, Bayesian probability theory is a method for estimating these elusive ultrasonic properties even when the waves are strongly overlapped. The results presented suggest significant anisotropy in phase velocity, nBUA, frequency independent loss (A_{fast} and A_{slow}), signal loss, and fast wave-to-slow wave amplitude ratio.

Bibliography

- Haïat, G., Padilla, F., Peyrin, F., and Laugier, P. (2008). “Fast wave ultrasonic propagation in trabecular bone: numerical study of the influence of porosity and structural anisotropy”, *J Acoust Soc Am* **123**, 1694–705.
- Hosokawa, A. and Otani, T. (1998). “Acoustic anisotropy in bovine cancellous bone”, *J Acoust Soc Am* **103**, 2718–22.
- Mizuno, K., Matsukawa, M., Otani, T., Laugier, P., and Padilla, F. (2009). “Propagation of two longitudinal waves in human cancellous bone: an in vitro study”, *J Acoust Soc Am* **125**, 3460–3466.
- Mizuno, K., Matsukawa, M., Otani, T., Takada, M., Mano, I., and Tsujimoto, T. (2008). “Effects of structural anisotropy of cancellous bone on speed of ultrasonic fast waves in the bovine femur”, *IEEE Trans Ultrason Ferroelectr Freq Control* **55**, 1480–7.
- Njeh, C. F., Hans, D., Fuerst, T., Glüer, C.-C., and Genant, H. K. (1999). *Quantitative Ultrasound: Assessment of Osteoporosis and Bone Status* (Martin Dunitz Ltd).

CHAPTER 7

BAYESIAN ANALYSIS OF CYCLIC VARIATION OF MYOCARDIAL BACKSCATTER

7.1 Preface

This Chapter is based on the manuscript “Bayesian parameter estimation for characterizing the cyclic variation of echocardiographic backscatter to assess the hearts of asymptomatic type 2 diabetes mellitus subjects” written by Christian C. Anderson, Allyson A. Gibson, Jean E. Schaffer, Linda R. Peterson, Mark R. Holland, and James G Miller. It is currently under review for publication in a peer-reviewed journal.

7.2 Abstract

Previous studies have shown that effective quantification of the cyclic variation of myocardial ultrasonic backscatter over the heart cycle might provide a non-invasive technique for identifying the early onset of cardiac abnormalities. These studies have demonstrated the potential for measurements of the magnitude and time delay of cyclic variation for identifying early onset of disease. The goal of this study was to extend this approach by extracting additional parameters characterizing the cyclic variation in an effort to better assess subtle changes in myocardial properties in asymptomatic subjects with type 2 diabetes. Echocardiographic images were obtained on a total of 43 age-matched normal control subjects and 100 type 2 diabetics. Cyclic variation data were generated by measuring the average level of ultrasonic backscatter over the heart cycle within a region of interest placed in the posterior wall of the left ventricle. Cyclic variation waveforms were modeled as piecewise linear functions, and quantified using a novel Bayesian parameter estimation method. Magnitude, rise time and slew rate parameters were extracted from models of the data. The ability of each of these parameters to distinguish between normal and type 2 diabetic subjects, and between subjects grouped by glycated hemoglobin (HbA1c) was compared. Results suggest a significant improvement in using measurements of the rise time and slew rate parameters of cyclic variation to differentiate ($p < 0.001$) the hearts of patients segregated based on widely employed indices of diabetic control compared to differentiation based on the magnitude of cyclic variation.

7.3 Introduction

Type 2 diabetes mellitus is a known risk factor for coronary artery disease and subsequent heart failure. In addition, an increasing body of evidence indicates that diabetes can lead to heart disease independent of atherosclerosis, a condition known as "diabetic cardiomyopathy" (Fang *et al.*, 2004; Hamby *et al.*, 1974; Kannel *et al.*, 1974; Witteles and Fowler, 2008; Rijzewijk *et al.*, 2008). The mechanisms underlying the development of diabetic cardiomyopathy are not fully understood, but several studies suggest that lipid metabolic abnormalities may play a role in lipid accumulation in non-adipose tissue, including myocardium, and that the accumulation of lipids in myocardium contributes to cell dysfunction, cell death, and subsequently cardiomyopathy (Kusminski *et al.*, 2009; Augustus *et al.*, 2003; Carley and Severson, 2005; Peterson *et al.*, 2004; Stremmel, 1988; Borradaile and Schaffer, 2005; Chiu *et al.*, 2001; Finck *et al.*, 2003; Nielsen *et al.*, 2002; Rijzewijk *et al.*, 2008; Zhou *et al.*, 2000).

Ultrasonic backscatter from myocardium has long been known to vary systematically over the cardiac cycle (Mottley *et al.*, 1984; Barzilai *et al.*, 1984; Wickline *et al.*, 1985; Mobley *et al.*, 1995; Naito *et al.*, 1996; DiBello *et al.*, 1998; Hu *et al.*, 2003; Holland *et al.*, 2004, 2007, 2009; Gibson *et al.*, 2009). Quantification of this cyclic variation of myocardial backscatter has provided a tool for non-invasive ultrasonic tissue characterization in a range of pathologies, including diabetes (Gibson *et al.*, 2009; Holland *et al.*, 2007; Wagner *et al.*, 1995; DiBello *et al.*, 1995; Pérez *et al.*, 1992). Traditionally, cyclic variation has been quantified by using the magnitude and time

delay (phase) of the systematic variation of backscatter over the heart cycle. Both of these parameters have been shown to be useful for characterizing myocardium (Holland *et al.*, 2007; Gibson *et al.*, 2009; Wagner *et al.*, 1995; DiBello *et al.*, 1995; Hu *et al.*, 2003; Finch-Johnston *et al.*, 2000). However, other features of the cyclic variation waveform may be more sensitive to the early onset of diabetic cardiomyopathy. Because diabetic cardiomyopathies may first manifest themselves in the form of diastolic dysfunction, methods for characterizing cyclic variation that measure diastolic function could be useful for distinguishing between healthy hearts and those at risk for disease. The current study introduces a novel method for modeling the cyclic variation of myocardial backscatter as a pulse waveform in order to extract parameters with the potential for identifying diastolic dysfunction. This model is then applied to a population of subjects that includes normal controls and asymptomatic type 2 diabetes patients to determine the ability of the model to discriminate between patient groups. Improved non-invasive methods for assessing the potential development of cardiomyopathies associated with type 2 diabetes could permit earlier and more effective intervention.

7.4 Methods

7.4.1 Subjects

Normal control subjects (with a fasting glucose < 100 mg/dL) and subjects with a history of type 2 diabetes mellitus between the ages of 30 and 55 years were recruited

for the study over a three-year span. All subjects underwent a screening medical history and physical exam and phlebotomy for routine laboratories. Participants were excluded from the study if they exhibited greater than Stage 1 hypertension as defined by the seventh report of the Joint National Committee (The Joint National Committee on the Prevention, Detection, Evaluation, and Treatment of High Blood Pressure, 2003); other systemic diseases (e.g. lupus); valvular disease; greater than trace or mild valvular regurgitation; an ejection fraction $< 55\%$; ischemic heart disease as assessed by a screening stress echocardiography exam; or symptoms of heart failure. Study participants were also excluded if they were current smokers, postmenopausal, pregnant, or lactating. A total of 143 subjects were retained in the study, which included 43 normal controls and 100 type 2 diabetics. The average age of the subjects was 43 ± 7 years, and included 57 males and 86 females. Signed informed consent for participation was obtained from each of the subjects under a human studies protocol approved by the Washington University Human Research Protection Office (HRPO).

7.4.2 Laboratory tests

Subjects underwent fasting glucose, glycated hemoglobin, and lipid and protein level tests after an overnight fast. A standard echocardiographic exam was performed to assess cardiac function in addition to the echocardiographic images acquired for ultrasonic tissue characterization.

7.4.3 Data acquisition

A General Electric Vivid 7 clinical imaging system (General Electric Medical Systems, Waukesha, WI, USA) was used to collect echocardiographic cineloops over approximately five heart cycles for each subject. The data were acquired from the parasternal long-axis view in harmonic imaging mode; the transmit frequency was 1.7 MHz, and the receive frequency was 3.4 MHz. The imaging system was configured such that there was a linear relationship between the displayed image grayscale value and changes in the level of ultrasonic backscatter expressed in decibels (dB). To verify this relationship, a series of measurements were performed on a tissue-mimicking phantom in which the imaging system gain was varied systematically in known dB steps. The average grayscale level was determined from within a region of interest placed on each phantom image at each gain setting to establish a conversion factor from image grayscale level to dB and to determine where the relationship was linear. The images were analyzed using NIH ImageJ software (National Institutes of Health, Bethesda, MD, USA).

Subject images were acquired with the system gain set at a level that optimized the dynamic range of the backscattered signals from the myocardium. The acquired data were analyzed offline by using NIH ImageJ to draw a region of interest within the left ventricular free wall and manually tracking it over the several heart cycles in the cineloops. The average grayscale levels within the region of interest for each image frame was recorded and converted to decibels to obtain a measurement of

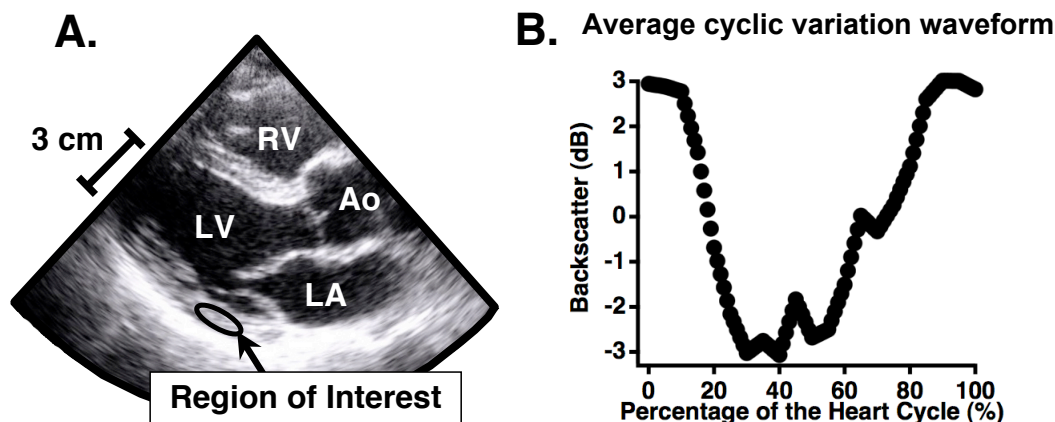


FIGURE 7.1: Regions of interest were placed within the posterior left ventricular wall on each image frame (shown in Panel A) and tracked throughout the heart cycle. The average level of backscatter was determined for each frame and averaged across five heart cycles to obtain an average cyclic variation waveform, such as the one depicted in Panel B.

backscattered energy. The backscattered energy in dB was plotted against time to obtain the systematic variation of ultrasonic backscatter from myocardium. This data was then averaged over the separate heart cycles and redimensioned so that it could be plotted as a percentage of the heart cycle, independent of heart rate. This processing results in average cyclic variation waveforms in which end-diastole is defined as the start (0%) and end (100%) of the heart cycle. A schematic of a region of interest within the posterior wall and the resulting average cyclic variation waveform is depicted in Fig. 7.1.

More details of cyclic variation data acquisition and analysis are outlined by Gibson *et al.* (2009).

7.4.4 Model of cyclic variation data

A piecewise linear model of cyclic variation was defined using six parameters to characterize a given cyclic variation waveform. Two parameters define the high and low levels for the waveform, and four parameters determine the placement (in time or percentage of the heart cycle) of the transition points between the line segments that comprise the model. The line segments are connected to form a continuous model waveform in the manner depicted in Panel A of Fig. 7.2. Mathematically, the model can be expressed as

$$M(x) = \begin{cases} H, & x \leq x_1 \\ m_a x + b_a, & x_1 < x \leq x_2 \\ L, & x_2 < x \leq x_3 \\ m_b x + b_b, & x_3 < x \leq x_4 \\ H, & x_4 < x \end{cases}, \quad (7.1)$$

where $M(x)$ is the amplitude of the model waveform at a percentage of the heart cycle x , H is the high amplitude level for the waveform, L is the low amplitude level for the waveform, and the x_i are the transition point parameters. The slopes of the line segments representing the transitions between the high and low levels, m_a and m_b , are given by

$$m_a = \frac{L - H}{x_2 - x_1} \quad (7.2a)$$

$$m_b = \frac{H - L}{x_4 - x_3} \quad (7.2b)$$

and the intercepts, b_a and b_b , are given by

$$b_a = H - m_a x_1 \quad (7.3a)$$

$$b_b = L - m_b x_3. \quad (7.3b)$$

This model can be used to characterize a generic positive-going or negative-going pulse with a variety of qualitatively different shapes, making it suitable for use on cyclic variation waveforms. Once a model for a specific waveform has been constructed, additional derived quantities can be extracted, such as the magnitude, rise time, fall time, slew rate, duration, and more.

7.4.5 Parameter estimation

Bayesian probability theory was used to estimate the six parameters $\{H, L, x_1, x_2, x_3, x_4\}$ in the model of cyclic variation for each subject. In Bayesian probability theory, all of the information about a given parameter is represented by a probability density function. As an example, the probability for the parameter L is expressed as $P(L|DI)$, where this notation is understood to denote the probability for L given the data D and available background information I . The posterior probability density functions for individual parameters can be computed from the joint posterior probability for all model parameters by marginalization, a process in which the joint posterior probability is integrated over all parameters except the one of interest. For instance, if all parameters are represented by $\Theta = \{H, L, x_1, x_2, x_3, x_4\}$, then the marginal posterior probability for L is calculated by

$$P(L|DI) = \iiint \iiint P(\Theta|DI) dH dx_1 dx_2 dx_3 dx_4, \quad (7.4)$$

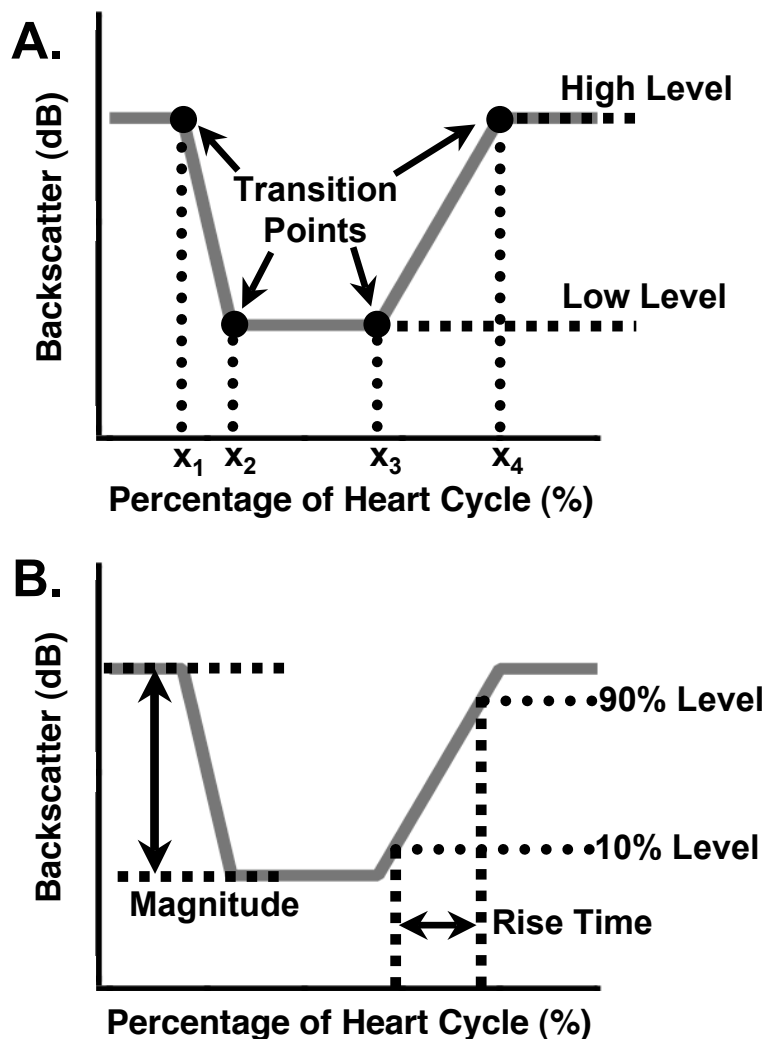


FIGURE 7.2: Panel A (top): Schematic of a model cyclic variation waveform and the parameters used to characterize it. The high and low amplitude levels determine the magnitude, and the four transition time parameters (x_1, x_2, x_3, x_4) mark the locations where the line segments join. Given a set of values for these six parameters, the model waveform (shown in gray) can be constructed. Panel B (bottom): Illustration of the pulse parameters derived from a model cyclic variation waveform. The magnitude is the difference between the high and low levels, and the rise time is the time taken to go from 10% of the magnitude to 90% of the magnitude on the rising edge. The slew rate is the difference between the 90% level and the 10% level, divided by the rise time.

where $P(\Theta|DI)$ is the joint posterior probability for all model parameters. Marginal posterior probabilities for the other parameters can be computed by using the same procedure, but integrating over the appropriate (different) sets of parameters. Thus, for the six-parameter model described in Eq. (7.1), a total of six integrals similar to Eq. (7.4) must be computed.

The joint posterior probability is obtained using Bayes' theorem,

$$P(\Theta|DI) = \frac{P(\Theta|I) P(D|\Theta I)}{P(D|I)}, \quad (7.5)$$

where $P(\Theta|I)$ is the prior probability for the parameters given only the background information I (i.e. before any data is analyzed), $P(D|\Theta I)$ is the likelihood, or direct probability for the data given the parameters and prior information, and $P(D|I)$ is the evidence.

The calculation is performed under the assumption that the model parameters are logically independent; that is, each prior probability depends only on the parameter in question and not on any others. For example, knowledge of L has no bearing on the knowledge of H , x_1 , or any other parameter. Under this assumption, the prior probability for the parameters can be factored using the product rule of probability theory, yielding

$$P(\Theta|I) = P(H|I) P(L|I) P(x_1|I) P(x_2|I) P(x_3|I) P(x_4|I) \quad (7.6)$$

The terms on the right-hand side of Eq. (7.6) are prior probabilities for the individual parameters. These prior probabilities are assigned as bounded Gaussian functions defined by a low, high, mean, and standard deviation for each parameter. The prior

TABLE 7.1: Summary of prior probability density functions used for each parameter in the Bayesian calculations. The means and standard deviations define Gaussian probability densities bounded by the low and the high values.

	Parameter					
	H (dB)	L (dB)	x_1	x_2	x_3	x_4
Low	-10	-10	0	0	0	0
Mean	0	0	50	50	50	50
High	10	10	100	100	100	100
Standard Deviation	10	10	50	50	50	50

information about the parameters is assumed to be vague, and hence the purpose of the prior probabilities are to provide order-of-magnitude estimates for the parameter values. The exact functional form of these prior probabilities has little effect on the final parameter estimates. Summaries of the Gaussian prior probability density functions are given in Table 7.1.

The likelihood, $P(D|\Theta I)$, was assigned using a Gaussian prior probability to represent what was known about the noise. The standard deviation of this Gaussian was removed via marginalization using a Jeffreys prior (Jeffreys, 1961).

Evaluation of complicated multi-dimensional integrals such as those in Eq. (7.4) is difficult or impossible to achieve analytically. As such, the integrals were approximated using a Markov chain Monte Carlo simulation. The nested sampling algorithm was used to carry out the Markov chain Monte Carlo calculations and to draw samples from the joint posterior probability (Skilling, 2006). The nested sampling calculations used 25 live points and 1000 iterations, which provided a satisfactory sampling of the

joint posterior probability. A detailed description of the nested sampling approach is given by Sivia (Sivia and Skilling, 2006) and Skilling (Skilling, 2006), and further details on Bayesian probability theory are given by Sivia and Skilling (Sivia and Skilling, 2006), Jaynes (Jaynes and Bretthorst, 2003), and Bretthorst (Bretthorst *et al.*, 2005).

7.4.6 Data analysis

At the completion of the Markov chain Monte Carlo simulation for a given set of input data, the Monte Carlo samples of the joint posterior probability were used to extract means and standard deviations for each parameter. A model waveform for the input data was constructed using the most probable values for each parameter. Because the model waveform for each data set can be described as a negative-going pulse, additional parameters characteristic of pulsed waveforms can be derived. The parameters extracted from the model waveforms in this study used in this study are illustrated in Panel B of Fig. 2. Each model waveform was analyzed to obtain magnitudes, rise times, and slew rates for each patient. The magnitude is defined as the difference between the high and low levels of the model waveform. The rise time is the time interval between the amplitudes representing 10% and 90% of the magnitude on the rising edge of the pulse. The slew rate is defined as the difference between 90% and 10% magnitude, divided by the rise time. The rising edge of the model waveform was chosen for this analysis because it corresponds to physiology that occurs during early diastolic relaxation, and therefore could serve as an indicator of diastolic dysfunction.

TABLE 7.2: Study group characteristics for the control and diabetic populations.

	Controls	Diabetics
Gender	M = 15 F = 28	M = 45 F = 55
Age (y)	41 ± 6	44 ± 7
	$p = \text{n.s.}$	
Body Mass Index (kg/m ³)	28 ± 6	34 ± 7
	$p < 0.001$	
HbA1c (%)	5.6 ± 0.4	7.6 ± 1.6
	$p < 0.001$	

Values are expressed as means ± standard deviations. n.s. = not significant.

The subjects were separated into diabetic (n = 100) and normal control (n = 43) groups, and the magnitudes, rise times, and slew rates for each group were compared. Statistical significance was determined by a two-tailed, unpaired Student's *t*-test. In addition, to examine further the impact glycemic control may have on the observed cyclic variation of backscatter, the subjects were divided into quartiles by glycated hemoglobin (HbA1c). Thus, although all subjects enrolled in this study had normal systolic function at rest and no evidence of significant obstructive coronary disease during stress echocardiography, the highest quartile of HbA1c (n = 35) can in principle be considered the most “diseased” and the lowest quartile (n = 35) could be considered the most “healthy” for the purposes of this study. Cyclic variation parameters for the highest and lowest quartiles were also compared using a two-tailed, unpaired Student's *t*-test. A summary of the subject group characteristics is given in Tables 7.2 and 7.3.

TABLE 7.3: Study group characteristics for the glycated hemoglobin (HbA1c) highest and lowest quartiles.

	Lowest Quartile	Highest Quartile
Gender	M = 13 F = 22	M = 16 F = 19
Age (y)	40 ± 6	42 ± 7
		$p = \text{n.s.}$
Body Mass Index (kg/m ³)	27 ± 6	36 ± 6
		$p < 0.001$
HbA1c (%)	5.4 ± 0.2	9.5 ± 1.2
		$p < 0.001$

Values are expressed as means ± standard deviations. n.s. = not significant.

7.5 Results

Representative data, along with corresponding model waveforms, are shown in Panels A and B of Fig. 7.3. The versatility of the piecewise linear model allows accurate representation of narrow cyclic variation waveforms that rise quickly back to baseline (Fig. 7.3, Panel A) as well as wider waveforms that take longer to return to baseline (Fig. 7.3, Panel B). Means and standard errors for the magnitude, rise time, and slew rate parameters for the different subject groups are shown in Fig. 7.4, with comparisons between the diabetic and control groups shown in the left-hand panels and those between the highest and lowest quartiles of HbA1c displayed in the right panels. As a group, the normal control subjects had shorter rise times and higher slew rates than their diabetic counterparts, indicating that on average, the cyclic variation of backscatter in the healthier subject population returned to baseline more rapidly

during diastole than in the diseased population. Similar characteristics are evident between the highest and lowest HbA1c quartile groups. The rise time and slew rate parameters showed highly significant differences between the control and diabetic populations as well as the high and low HbA1c quartiles (p ranged between 0.003 and less than 0.0001). The differences in the magnitude of cyclic variation between the respective groups was either not significant ($p = 0.06$) or weakly significant ($p < 0.05$).

7.6 Discussion

Constructing models of cyclic variation data might provide further non-invasive tools for quantification of cardiac function that extend beyond the information obtained using conventional analysis of cyclic variation. Specifically, the shape of the waveform itself may provide indications of dysfunction that are independent or only weakly dependent on the traditionally reported magnitude of cyclic variation. The piecewise linear model examined in this study permits a relatively simple means of modeling such data, and the pulse parameters derived from it (rise time and slew rate) allow basic quantification of waveform characteristics that could have relevance to diastolic function. Although all subjects in the study exhibited clinically normal cardiac function, measurements of these novel cyclic variation parameters demonstrated highly significant differences between normal controls and individuals with type 2 diabetes, as well as between individuals with high and low HbA1c. Results for

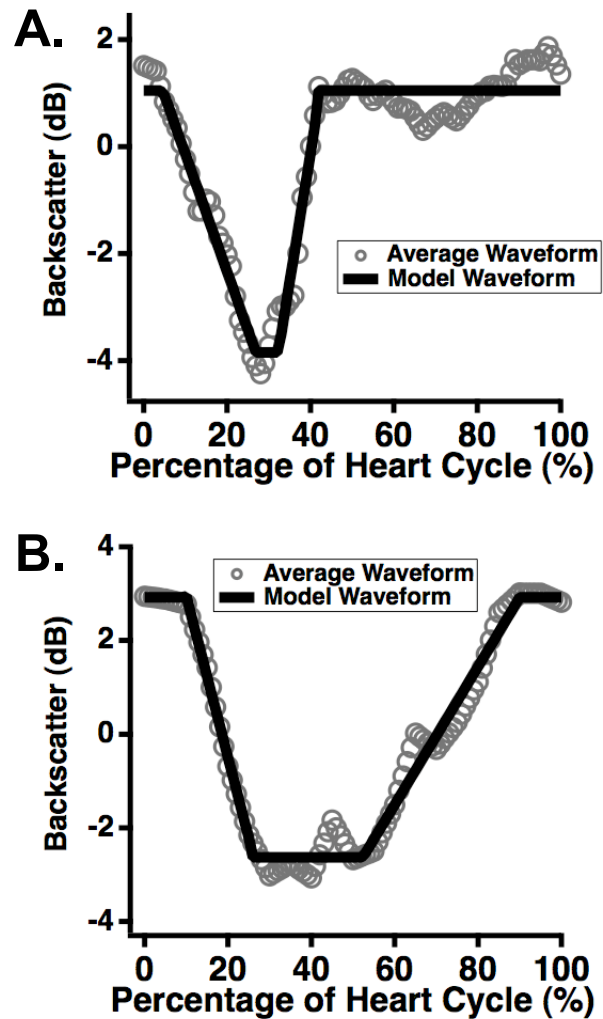


FIGURE 7.3: Representative results for models of acquired cyclic variation data. The data, consisting of backscatter averaged over five heart cycles, are shown in gray circles; the models are shown in solid black lines. The flexible nature of the model allows good representation of both narrow (Panel A) and wide (Panel B) waveform data.

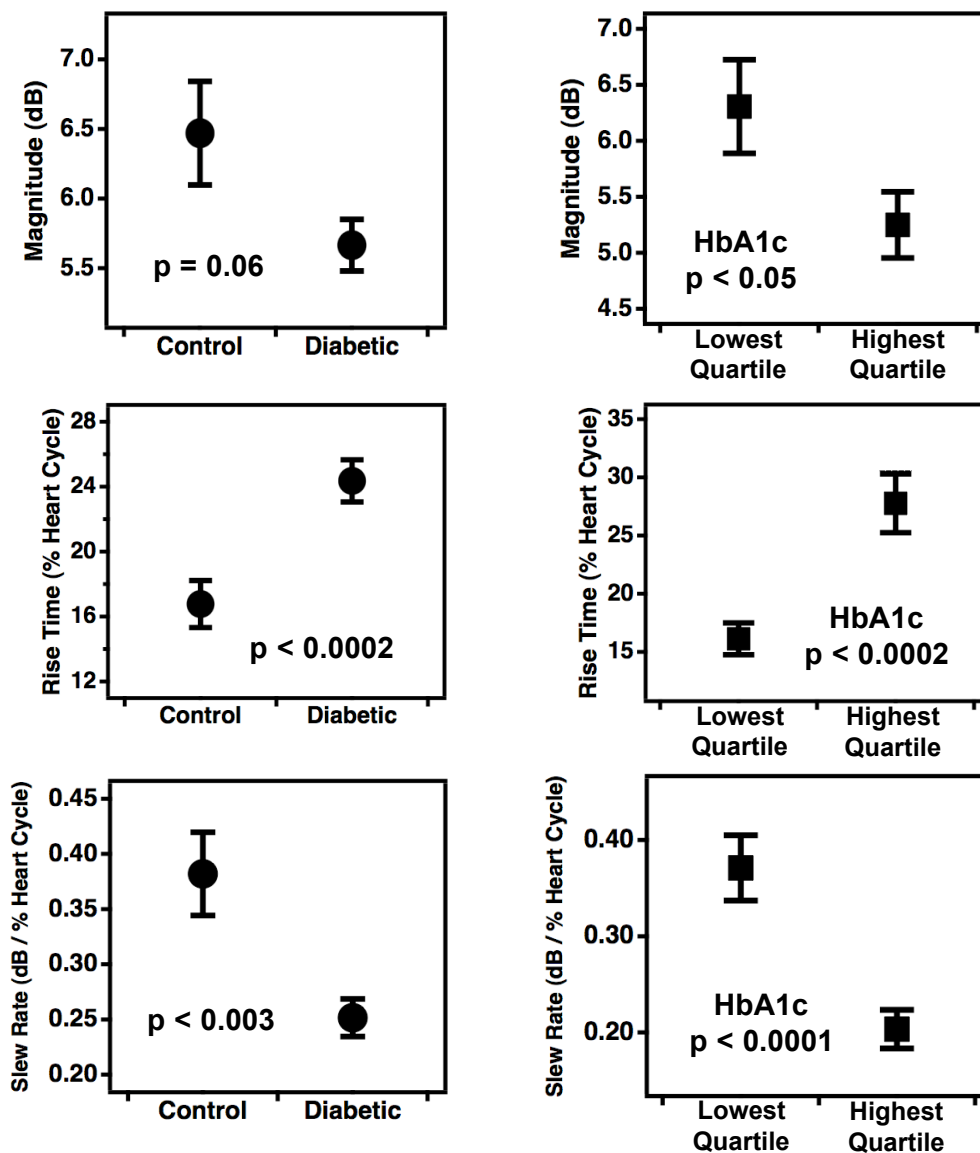


FIGURE 7.4: Differences in the magnitude, rise time, and slew rate of the cyclic variation of backscatter from myocardium among the two subject groupings. Differences between normal control and type 2 diabetic subjects are shown in the left panels, and those between the highest and lowest quartiles of subjects grouped by glycated hemoglobin (HbA1c) are shown in the right panels. Data are presented as means \pm standard errors. Corresponding p -values determined by two-tailed t -tests are included in each panel.

the magnitude parameter are consistent with previous studies involving type 1 and type 2 diabetics (Wagner *et al.*, 1995; Gibson *et al.*, 2009) in that higher magnitudes were observed in healthy individuals than in diabetics. However, the differences in rise time and slew rate between these two populations are stronger than the differences in the magnitude. Subjects without diabetes and subjects with low HbA1c tended to have lower rise times and higher slew rates than their counterparts. If these parameters do indeed have a close correspondence with diastolic performance, this finding is consistent with the expectation that individuals subject to early onset of cardiomyopathies will first present with diastolic dysfunction.

The present study is limited by the absence of concrete evidence of cardiac metabolic or structural abnormalities. Indeed, it is impossible under the current study conditions to determine which, if any, subjects will develop a diabetic cardiomyopathy. A careful longitudinal study over many years could perhaps determine definitively whether differences in the parameters examined here are truly indicative of a high risk for cardiac dysfunction, but such an investigation is beyond the scope of the current study.

In summary, analyses of model-derived parameters for cyclic variation data, especially rise time and slew rate, suggest that using a model-based approach could lead to enhancement or improvement in patient classification. Using these parameters in tandem with magnitude or time delay analyses could eventually lead to effective non-invasive monitoring of patients at higher risk for type 2 diabetic cardiomyopathy.

Funding sources

This research was supported in part by NIH R01 HL40302, NIH R01 AR57433, National Science Foundation 57238 (FDA Scholar in Residence), NIH P20 RR020643, Burroughs Wellcome Fund (1005935), and a grant from the Barnes Jewish Hospital Foundation.

Bibliography

- Augustus, A. S., Kako, Y., Yagyu, H., and Goldberg, I. J. (2003). “Routes of FA delivery to cardiac muscle: modulation of lipoprotein lipolysis alters uptake of TG-derived FA”, *Am J Physiol Endocrinol Metab* **284**, E331–9.
- Barzilai, B., Madaras, E. I., Sobel, B. E., Miller, J. G., and Pérez, J. E. (1984). “Effects of myocardial contraction on ultrasonic backscatter before and after ischemia”, *Am J Physiol* **247**, H478–83.
- Borradaile, N. M. and Schaffer, J. E. (2005). “Lipotoxicity in the heart”, *Curr Hypertens Rep* **7**, 412–7.
- Bretthorst, G. L., Hutton, W. C., Garbow, J. R., and Ackerman, J. J. (2005). “Exponential parameter estimation (in NMR) using Bayesian probability theory”, *Concepts Magn Reson* **27A**, 55–63.
- Carley, A. N. and Severson, D. L. (2005). “Fatty acid metabolism is enhanced in type 2 diabetic hearts”, *Biochim Biophys Acta* **1734**, 112–26.
- Chiu, H. C., Kovacs, A., Ford, D. A., Hsu, F. F., Garcia, R., Herrero, P., Saffitz, J. E., and Schaffer, J. E. (2001). “A novel mouse model of lipotoxic cardiomyopathy”, *J Clin Invest* **107**, 813–22.
- DiBello, V., Giampietro, O., Matteucci, E., Giorgi, D., Bertini, A., Piazza, F., Talini, E., Paterni, M., and Giusti, C. (1998). “Ultrasonic tissue characterization analysis in type 1 diabetes: a very early index of diabetic cardiomyopathy?”, *G Ital Cardiol* **28**, 1128–37.
- DiBello, V., Talarico, L., Picano, E., Muro, C. D., Landini, L., Paterni, M., Matteucci, E., Giusti, C., and Giampietro, O. (1995). “Increased echodensity of myocardial wall in the diabetic heart: an ultrasound tissue characterization study”, *J Am Coll Cardiol* **25**, 1408–15.
- Fang, Z. Y., Prins, J. B., and Marwick, T. H. (2004). “Diabetic cardiomyopathy: evidence, mechanisms, and therapeutic implications”, *Endocr Rev* **25**, 543–67.
- Finch-Johnston, A. E., Gussak, H. M., Mobley, J., Holland, M. R., Petrovic, O., Pérez, J. E., and Miller, J. G. (2000). “Cyclic variation of integrated backscatter: dependence of time delay on the echocardiographic view used and the myocardial segment analyzed”, *J Am Soc Echocardiogr* **13**, 9–17.
- Finck, B. N., Han, X., Courtois, M., Aimond, F., Nerbonne, J. M., Kovacs, A., Gross, R. W., and Kelly, D. P. (2003). “A critical role for pparalpha-mediated lipotoxicity in the pathogenesis of diabetic cardiomyopathy: modulation by dietary fat content”, *Proc Natl Acad Sci U S A* **100**, 1226–31.

- Gibson, A. A., Schaffer, J. E., Peterson, L. R., Bilhorn, K. R., Robert, K. M., Haider, T. A., Farmer, M. S., Holland, M. R., and Miller, J. G. (2009). “Quantitative analysis of the magnitude and time delay of cyclic variation of myocardial backscatter from asymptomatic type 2 diabetes mellitus subjects”, *Ultrasound Med Biol* **35**, 1458–1467.
- Hamby, R. I., Zoneraich, S., and Sherman, L. (1974). “Diabetic cardiomyopathy”, *JAMA* **229**, 1749–54.
- Holland, M. R., Gibson, A., Kirschner, C., Hicks, D., Ludomirsky, A., and Singh, G. (2009). “Intrinsic myoarchitectural differences between the left and right ventricles of fetal human hearts: An ultrasonic backscatter feasibility study”, *J Am Soc Echocardiogr* **22**, 170–176.
- Holland, M. R., Gibson, A. A., Peterson, L. R., Areces, M., Schaffer, J. E., Perez, J. E., and Miller, J. G. (2007). “Measurements of the cyclic variation of myocardial backscatter from two-dimensional echocardiographic images as an approach for characterizing diabetic cardiomyopathy”, *J Cardiometab Syndr* **1**, 149–52.
- Holland, M. R., Wallace, K. D., and Miller, J. G. (2004). “Potential relationships among myocardial stiffness, the measured level of myocardial backscatter (“image brightness”), and the magnitude of the systematic variation of backscatter (cyclic variation) over the heart cycle”, *J Am Soc Echocardiogr* **17**, 1131–7.
- Hu, X., Wang, J., Sun, Y., Jiang, X., Sun, B., Fu, H., and Guo, R. (2003). “Relation of ultrasonic tissue characterization with integrated backscatter to contractile reserve in patients with chronic coronary artery disease”, *Clin Cardiol* **26**, 485–8.
- Jaynes, E. T. and Bretthorst, G. L. (2003). *Probability theory: the logic of science* (Cambridge Univ Press).
- Jeffreys, H. (1961). *Theory of probability* (Oxford Univ Press).
- Kannel, W. B., Hjortland, M., and Castelli, W. P. (1974). “Role of diabetes in congestive heart failure: the framingham study”, *Am J Cardiol* **34**, 29–34.
- Kusminski, C., Shetty, S., Orci, L., Unger, R., and Scherer, P. (2009). “Diabetes and apoptosis: lipotoxicity”, *Apoptosis* **14**, 1484–1495.
- Mobley, J., Banta, C., Gussak, H., Perez, J. E., and Miller, J. G. (1995). “Clinical tissue characterization: Online determination of magnitude and time delay of myocardial backscatter”, *Video Journal of Echocardiography* **5**, 40–48.
- Mottley, J. G., Glueck, R. M., Perez, J. E., Sobel, B. E., and Miller, J. G. (1984). “Regional differences in the cyclic variation of myocardial backscatter that parallel regional differences in contractile performance”, *J Acoust Soc Am* **76**, 1617–23.

- Naito, J., Masuyama, T., Mano, T., Yamamoto, K., Doi, Y., Kondo, H., Nagano, R., Inoue, M., and Hori, M. (1996). "Influence of preload, afterload, and contractility on myocardial ultrasonic tissue characterization with integrated backscatter", *Ultrasound Med Biol* **22**, 305–12.
- Nielsen, L. B., Bartels, E. D., and Bollano, E. (2002). "Overexpression of apolipoprotein b in the heart impedes cardiac triglyceride accumulation and development of cardiac dysfunction in diabetic mice", *J Biol Chem* **277**, 27014–20.
- Pérez, J. E., McGill, J. B., Santiago, J. V., Schechtman, K. B., Waggoner, A. D., Miller, J. G., and Sobel, B. E. (1992). "Abnormal myocardial acoustic properties in diabetic patients and their correlation with the severity of disease", *J Am Coll Cardiol* **19**, 1154–62.
- Peterson, L. R., Herrero, P., Schechtman, K. B., Racette, S. B., Waggoner, A. D., Kisrieva-Ware, Z., Dence, C., Klein, S., Marsala, J., Meyer, T., and Gropler, R. J. (2004). "Effect of obesity and insulin resistance on myocardial substrate metabolism and efficiency in young women", *Circulation* **109**, 2191–6.
- Rijzewijk, L. J., van der Meer, R. W., Smit, J. W., Diamant, M., Bax, J. J., Hammer, S., Romijn, J. A., de Roos, A., and Lamb, H. J. (2008). "Myocardial steatosis is an independent predictor of diastolic dysfunction in type 2 diabetes mellitus", *J Am Coll Cardiol* **52**, 1793–9.
- Sivia, D. S. and Skilling, J. (2006). *Data analysis: a Bayesian tutorial* (Oxford Univ Press).
- Skilling, J. (2006). "Nested sampling for general Bayesian computation", *Bayesian Analysis* **1**, 833–860.
- Stremmel, W. (1988). "Fatty acid uptake by isolated rat heart myocytes represents a carrier-mediated transport process", *J Clin Invest* **81**, 844–52.
- Wagner, R. F., Wear, K. A., Perez, J. E., McGill, J. B., Schechtman, K. B., and Miller, J. G. (1995). "Quantitative assessment of myocardial ultrasound tissue characterization through receiver operating characteristic analysis of Bayesian classifiers", *J Am Coll Cardiol* **25**, 1706–11.
- Wickline, S. A., Thomas, L. J., Miller, J. G., Sobel, B. E., and Pérez, J. E. (1985). "The dependence of myocardial ultrasonic integrated backscatter on contractile performance", *Circulation* **72**, 183–92.
- Witteles, R. M. and Fowler, M. B. (2008). "Insulin-resistant cardiomyopathy clinical evidence, mechanisms, and treatment options", *J Am Coll Cardiol* **51**, 93–102.
- Zhou, Y. T., Grayburn, P., Karim, A., Shimabukuro, M., Higa, M., Baetens, D., Orzi, L., and Unger, R. H. (2000). "Lipotoxic heart disease in obese rats: implications for human obesity", *Proc Natl Acad Sci U S A* **97**, 1784–9.

CHAPTER 8

SUMMARY AND CONCLUDING REMARKS

This scope of this Dissertation encompassed simulated and experimental studies of the physics underlying the interaction of ultrasound with cancellous bone and myocardium. A central theme was the use of Bayesian probability theory in data analysis. Bayesian parameter estimation was used in a model for ultrasonic wave propagation in bone, and in a model to characterize ultrasonic backscatter from myocardium.

Chapter 2 provided context for later Chapters related to bone sonometry. Background on the use of ultrasound for diagnosis and monitoring of osteoporosis was given, followed by information on dispersion in cancellous bone. The apparent disagreement between the Kramers-Kronig relations and experimental measurements of phase velocity was presented, along with proposed explanations.

Chapter 3 was a study investigating whether, and to what extent, fast and slow

waves present in ultrasonic signals transmitted through bone affect measurements of phase velocity. The results of simulated data suggested that when two waves are present in the acquired signal, negative dispersion can be measured if the signal is assumed to be composed of only one wave. Anomalous dispersion was exhibited even when the amplitude of the second wave is small compared to the dominant mode. Furthermore, in some cases in which the dispersion of the mixed mode waveform is negative, the attenuation coefficient retained an approximately linear relationship with frequency.

Chapter 4 introduced Bayesian probability theory and Markov chain Monte Carlo methods for evaluating marginal posterior probabilities. Details were given for calculations used in later Chapters in parameter estimation, including simulated annealing (Chapter 5) and nested sampling (Chapter 7).

The study reported in Chapter 5 used Bayesian parameter estimation to estimate the ultrasonic properties of overlapping fast and slow waves in simulated data and in experimental data acquired on bone-mimicking phantoms and human cancellous bone. The parameter estimates for the simulations were in excellent agreement with the input data. In the studies on bone-mimicking phantoms, Bayesian analysis was also successful in estimating parameters for the fast and slow waves that were in agreement with the known ultrasonic properties of the plastics used to construct the phantoms. For data acquired on bone, the models constructed with highly probable parameter estimates were also in good agreement with the acquired data. However, experimental factors such as insertion losses, phase cancellation, and uncertainty in

the way energy is distributed among the fast and slow waves make interpretation of the results more complicated.

Chapter 6 reported the results of Bayesian parameter estimation applied to ultrasonic data acquired on a spherical cancellous bone sample extracted from a bovine femur. Measurements were taken in 10 degree steps between insonation angles of 0 degrees and 180 degrees relative to the predominant direction of the trabeculae. Conventional analysis techniques were difficult to apply to the full data set because the fast and slow waves strongly overlapped when the insonation angle approaches 90 degrees. However, the fast and slow waves were able to be reconstructed using Bayesian methods, allowing full characterization of the anisotropy. Anisotropies were found in velocity, attenuation, and relative amplitude parameters even when the fast and slow waves were strongly overlapped.

In Chapter 7, Bayesian methods were used to estimate parameters in a piecewise linear model of the cyclic variation of backscatter from myocardium in 43 normal control subjects and 100 subjects with type 2 diabetes mellitus. The subjects were also grouped into quartiles by glycated hemoglobin (HbA1c). Subjects with diabetes or high HbA1c were found, on average, to have longer rise times and lower slew rates than the normal controls or subjects with low HbA1c. Greater statistical significances were found in the differences between the subject groups for the rise time and slew rate parameters derived from the model than for the magnitude of cyclic variation alone.